
MASS-DEPENDENT TITANIUM ISOTOPE VARIATIONS IN TERRESTRIAL
AND EXTRA-TERRESTRIAL BASALTS

Inaugural-Dissertation

zur

Erlangung des Doktorgrades
der Mathematisch-Naturwissenschaftlichen Fakultät
der Universität zu Köln

vorgelegt von

Sebastian Kommescher

aus Le Chesnay (Frankreich)

Köln, 2020

Berichterstatter (Gutachter):

Prof. Dr. Carsten Munker

Prof. Raúl Fonseca (PhD)

Tag der mündlichen Prüfung:

20.3.2020

In the beginning the Universe was created. This has made a lot of people very angry and been widely regarded as a bad move.

- Douglas Adams

ABSTRACT

Titanium is a fairly abundant minor element and while some silicates can contain relatively large amounts of Ti (titanite, Ca-rich amphiboles), the most common Ti bearing phases are Ti oxides, such as ilmenite and rutile. Titanium is incompatible in most silicate minerals and is enriched in the melt during fractional crystallisation of a magma. The increasing Ti content in the melts eventually leads to fractional crystallisation of Ti-oxides. The lower spatial coordination of Ti in a melt relative to a higher spatial coordination of Ti in crystallising Ti oxides, leads to preferential partitioning of lighter Ti isotopes into the Ti-bearing oxides. Consequently, the Ti isotope composition of the residual melt gets increasingly heavier during fractional crystallisation of Ti oxides and Ti isotopes can trace the evolution of a magmatic system. High-precision analysis of Ti isotopes are performed with the so-called double spike technique. The double spike is a synthetic solution in which the abundances of two isotopes are synthetically enriched. Once the isotope composition of the double spike is very well-known, it is added to a sample and after chemical separation and mass spectrometric analysis, iterative calculations constrain the deviation of the Ti isotope composition of the analysed sample from a given reference material.

This monograph reports the process of implementation the Ti double spike isotope dilution technique at the University of Cologne's Geo- and Cosmochemistry group is (CHAPTER 2). The double spike tracer solution and an additional synthetic reference material similar to the established Origins Lab Ti reference material are calibrated. Furthermore, chemical and mass spectrometric protocols are developed and refined to ensure best possible chemical separation of Ti from other elements as well as high precision and accuracy of Ti isotope measurements on a Neptune Plus Multi-Collector Inductively Coupled Plasma Mass Spectrometer.. After the successful implementation of this technique, Ti isotope compositions of lunar and terrestrial samples are determined.

The results from CHAPTER 3 expand available Ti isotope data for lunar samples and help to further constrain the Ti isotope composition of the urKREEP component (the residual liquid, enriched in incompatible elements like K, Rare Earth Elements and P in the final stage of Lunar Magma Ocean solidification). In addition to the analysed samples, modelling aims to constrain the exact Ti isotope composition of the urKREEP component. Modelling results are in good agreement with both analysed samples and reported literature data. Titanium isotope compositions of low- and high-Ti mare basalts reveal resolvable variations, most likely due to petrogenetic processes. The assumed low-Ti mare basalt source region is the ambient mafic cumulate mantle, whereas high-Ti mare basalts require the presence of a Ti-rich phase, most likely a mixture of mafic cumulates and the late stage ilmenite-bearing cumulates (latest stages of Lunar Magma Ocean solidification). Results show significant Ti isotope variations in high-Ti mare basalts which are, coupled with high precision High Field Strength Elements data, best explained by the partial melting of an ilmenite bearing cumulate. Observed intragroup Ti isotope variations in low-Ti mare basalts are most likely due to fractional crystallisation of ilmenite prior to eruption or the absence of a Ti-rich phase during petrogenesis. Using partitioning data and potential source compositions based on Lunar Magma Ocean solidification models, fractional crystallisation of ilmenite and partial melting in the presence or absence of ilmenite are modelled. The modelled trends further demonstrate that observed Ti isotope variations in high-Ti and low-Ti mare basalts are due to partial melting of an ilmenite bearing cumulate and fractional crystallisation of ilmenite, respectively. Furthermore, data and modelling tentatively exclude high-Ti mare basalt petrogenesis through assimilation of an ilmenite-bearing cumulate component into a low-Ti magma.

The Ti isotope composition of subduction zone derived rocks are the focus of CHAPTER 4 of this monograph. Representative sets from various subduction zones are chosen. In addition to tholeiitic samples from two localities, samples from the more depleted mantle wedge (boninites) and sediment drill cores from two localities were analysed. Coupled with an extensive isotope, trace element and High Field Strength Elements data set, Ti isotope data reveal no Ti isotope fractionation through hydrous sediment melts. These data rather suggest that partial melting in the presence of Ti-oxides (or lack thereof) is the key factor driving Ti isotope fractionation in subduction zone related rocks. Similarly, the systematically heavier Ti isotope composition of boninitic samples compared to related tholeiitic samples are consistent with boninite petrogenesis through partial melting of a more depleted mantle source in the

presence of Cr-spinel. In contrast to previous studies however, samples from one locality suggest that amphibole, a silicate mineral, is leading to Ti isotope fractionation.

This monograph demonstrates that coupled Ti isotope and High Field Strength Element variations allow the precise differentiation of the petrogenetic processes on Earth and Moon and demonstrate the great potential of coupled Ti isotope-High Field Strength Element studies. Additionally, results in this monograph suggest that petrogenetic involvement of amphibole may have fractionated Ti isotopes in one sample location. This stresses the need for future experimental studies as well as mineral separate studies in order to better constrain Ti isotope fractionation behaviour.

ZUSAMMENFASSUNG

Titan ist ein relativ häufiges Nebenelement. Während einige Silikate größere Mengen an Titan enthalten können (Titanit, Ca-reiche Amphibole), so sind die häufigsten Ti-reichen Phasen die Ti-Oxide, wie Ilmenit und Rutil. Als in den meisten Silikatmineralen inkompatibles Element wird Ti während der fraktionierten Kristallisation eines Magmas in der Schmelze angereichert. Der stetig steigende Titangehalt in der Schmelze führt dazu, dass ab einem gewissen Ti-Gehalt Titanoxide aus der Schmelze auskristallisieren. Die niedrigere räumliche Koordination von Ti relativ zur höheren Koordination im Kristallgitter der Oxide führt zu einem bevorzugten Einbau der leichten Ti-Isotope in das Kristallgitter der Oxide. Folglich wird während der Kristallisation die zurückbleibende Schmelze stetig an schwereren Ti-Isotopen angereicht, wodurch es möglich wird, anhand von Ti-Isotopen die Entwicklung eines magmatischen Systems nachzuvollziehen.

Hochpräzise Messungen von Ti-Isotopenzusammensetzungen werden mit der sogenannten Doppelspike-Methode durchgeführt. Ein Doppelspike ist eine künstlich hergestellte Lösung, in der die Häufigkeiten zweier Ti-Isotope stark erhöht sind, wohingegen die Häufigkeiten der übrigen Ti-Isotope stark verarmt sind. Sobald diese Isotopenverhältnisse in der Lösung sehr genau bekannt ist, wird sie zu einer unbekannt Probe hinzugegeben und nach chemischer Abtrennung störender Elemente und massenspektrometrischer Bestimmung der Mischung, kann daraus durch iterative Berechnungen die Ti-Isotopenzusammensetzung der unbekannt Probe relativ zu einem Referenzmaterial sehr genau und präzise bestimmt werden.

Diese Monographie beschreibt die Implementierung der Ti-Doppelspike-Isotopenverdünnungsmethode in der Arbeitsgruppe Geo- und Kosmochemie der Universität zu Köln (KAPITEL 2). Neben dem Doppelspike wird zusätzlich ein weiteres Referenzmaterial, welches dem etablierten „Origins Lab“-Ti-Standard ähnelt, kalibriert. Weiterhin werden die chemischen Trennverfahren und massenspektrometrischen Protokolle entwickelt und angepasst, um die höchstmögliche Präzision der Methode an dem Neptune Plus Multi-

Kollektor-Plasmaquellen-Massenspektrometer sicherzustellen. Nach der erfolgreichen Kalibrierung der Chemikalien und der Messprotokolle werden diese angewendet, um die Ti-Isotopenzusammensetzung von Mondgesteinen sowie terrestrischen Gesteinen zu bestimmen.

Die in KAPITEL 3 vorgestellten Ergebnisse erweitern die vorhandenen Ti-Isotopendaten für Mondgesteine und erlauben das genauere Bestimmen der Ti-Isotopenzusammensetzung der postulierten urKREEP-Komponente, der letzten Flüssigphase vor Erstarren des lunaren Magmaozeans (angereichert an inkompatiblen Elementen wie K, den Seltenen Erden, sowie P). Zusätzlich zu den Analysen wird die Ti-Isotopenzusammensetzung der urKREEP-Komponente durch Modellrechnungen bestimmt. Diese sind im Rahmen der Unsicherheiten identisch mit den hier gemessenen Daten und vorangegangenen Arbeiten. Titan-Isotopenzusammensetzungen der „low-Ti“ und „high-Ti“ Mare Basalte zeigen deutliche Variationen, welche wahrscheinlich durch den petrogenetischen Entstehungsprozess der Gesteine entstanden sind. Während die vermutete „low-Ti“ Mare-Basalt-Magmenquelle der mafische Mantel des Mondes ist, benötigen die „high-Ti“ Mare-Basalte für ihre Entstehung die Gegenwart einer Ti-reichen Phase in der Magmenquelle, wie Ilmenit. Damit ist die Quellregion höchstwahrscheinlich eine Mischung aus dem mafischen Mantel und den Ilmenit-reichen Kumulaten. Die beobachteten Variationen in Ti-Isotopenzusammensetzungen in „high-Ti“ Mare-Basalten sind, gekoppelt mit „High Field Strength Element (Elemente mit hoher Valenz und kleinem Ionenradius)“ Daten, auf das partielle Schmelzen eines Ilmenit-reichen Kumulats zurückzuführen. Die Ti-Isotopenvariationen innerhalb der „low-Ti“ Mare-Basalt Gruppen sind auf fraktionierte Kristallisation von Ilmenit vor der Eruption des Magmas oder das Ausbleiben dieses Prozesses zurückzuführen. Mittels Verteilungskoeffizienten sowie möglichen Zusammensetzungen der „high-Ti“ Quellregionen, welche wiederum auf verschiedenen Magmaocean-Kristallisationsmodellen basieren, wird das partielle Schmelzen des mafischen Mantels (ohne Ilmenit) oder der Ilmenit-reichen Kumulate modelliert. Die berechneten Trends stimmen mit den hier gemachten Beobachtungen überein und unterstreichen, dass die Variationen in „high-Ti“ und „low-Ti“ Mare-Basalten auf das partielle Schmelzen eines Ilmenit-reichen Kumulats und fraktionierte Kristallisation von Ilmenit zurückzuführen sind. Weiterhin kann, basierend auf den Ergebnissen dieser Studie, eine Petrogenese der „high-Ti“ Mare-Basalte durch Assimilation einer Ilmenit-reichen Komponente in ein „low-Ti“ Magma ausgeschlossen werden.

In Kapitel 4 wurden Proben verschiedener Subduktionszonen, sowie dazugehörige Boninite und Sedimentproben gemessen. Titan-Isotopenzusammensetzungen mit zusätzlichen

Spurenelement- und High Field Strength Element-Daten zeigen, dass wasserreiche Schmelzen des subduzierten Sediments keinen Einfluss auf die Ti-Isotopenzusammensetzung haben. Vielmehr liegt der Grund für die beobachteten Variationen wahrscheinlich in der An beziehungsweise Abwesenheit von Ti-reichen Oxiden während des partiellen Schmelzens des subduzierten Materials. Weiterhin zeigen die systematisch schwereren Ti-Isotopenzusammensetzungen der boninitischen Proben relativ zu den dazugehörigen Tholeiiten, dass das partielle Schmelzen des verarmten Mantelkeils in der Gegenwart von Cr-reichem Spinell zu Ti-Isotopenfraktionierung führt. Anders als frühere Studien deuten die Ergebnisse in dieser Arbeit auch darauf hin, dass Amphibole Ti-Isotope fraktionieren können, was bisher nicht beobachtet wurde.

Diese Monographie stellt heraus, dass die Kombination von High Field Strength Element-Daten mit Ti-Isotopendaten weitreichende Einblicke in die petrogenetischen Prozesse von Mondgesteinen und terrestrischen Gesteinen erlauben. Zusätzlich deuten terrestrische Ti-Isotopenvariationen in einer Lokalität darauf hin, dass neben Ti-reichen Oxiden auch einige silikatische Minerale, genauer Amphibole, Ti-Isotope fraktionieren können. Dies unterstreicht nur noch mehr die Notwendigkeit, Ti-Isotopenfraktionierungsfaktoren für silikatische Minerale zu bestimmen.

PREFACE

This thesis is submitted in partial fulfilment of the requirements for obtaining the doctoral degree in Natural Sciences (Doctor rerum naturalium) at the University of Cologne. The work described herein was conducted at the Geo- and Cosmochemistry Research Group of the Institute for Geology and Mineralogy between January 2016 and January 2020 under the joint supervision of Dr. Peter Sprung (2016 – 2017) Prof. Dr. Carsten Münker (2016 – 2019) with additional supervision by Dr. Raúl Fonseca (2018 – 2019). The position was partially financed through a UoC Advanced Post Doc grant within the Excellence Initiative to Dr. Sprung (2016 – 2018) and the UoC Graduate School of Geosciences fellowship (2019; GSGS-2019X-07). An index of (partially) published portions of this thesis are given at the end of the document.

TABLE OF CONTENT

1	INTRODUCTION	1
1.1	Stable isotope systematics.....	2
1.1.1	Mass Fractionation – First principles	4
1.1.2	Mass-independent isotope effects.....	7
1.1.3	Reference materials in stable isotope geochemistry.....	8
1.2	Titanium elemental and stable isotope systematics	10
1.2.1	Geochemical behaviour of Ti	10
1.2.2	Titanium isotopes as a tracer of magmatic differentiation	11
1.2.3	Extra-terrestrial, mass-dependent isotope systematics	13
1.2.4	Extra-terrestrial Ti isotope systematics and nucleosynthetic heritage.....	14
1.3	Motivation and objectives.....	17
2	METHODS.....	19
2.1	Ion Chromatography / Chemistry	20
2.1.1	Calibration of the separation method.....	20
2.1.2	Final Ti separation scheme	22
2.2	Double Spike Isotope Dilution.....	24
2.2.1	Spike and Reference Material calibration.....	25
2.2.2	Data reduction.....	29
2.3	MC-ICP-MS.....	35
3	UNRAVELLING LUNAR MANTLE PROCESSES THROUGH THE Tl ISOTOPE COMPOSITION OF LUNAR BASALTS.....	39
3.1	Introduction.....	40
3.1.1	Formation of the Moon.....	40
3.2	Titanium isotope systematics of lunar basalts.....	46
3.2.1	Neutron capture effects and potential sampling bias.....	47
3.3	Results.....	49

3.4	Discussion	54
3.4.1	Modelling the Ti isotope composition of urKREEP	54
3.4.2	Modelling the Ti isotope evolution of mare basalts	60
3.4.3	Partial melting of different cumulate compositions.....	63
3.4.4	Assimilation of an IBC component by a low-Ti magma.....	65
3.4.5	Identifying magmatic processes in lunar basalt sources.....	67
3.4.6	Other isotope systems	70
3.5	Conclusion	72
4	TITANIUM ISOTOPE VARIATIONS IN SUBDUCTION ZONE DERIVED ROCKS... 75	
4.1	Introduction.....	76
4.1.1	Convergent plate margins and arc volcanism.....	76
4.1.2	Titanium isotope systematics in subduction zones.....	78
4.1.3	Geological background and sample selection.....	79
4.2	Methods.....	82
4.2.1	Sample digestion and column chemistry	82
4.2.2	MC-ICP-MS measurements	84
4.3	Results.....	84
4.4	Discussion	88
4.4.1	General remarks on coupled $\delta^{49}\text{Ti}$ – (trace) element systematics	89
4.4.2	Can the recycling of subducted sediments affect the Ti isotope composition of arc lithologies? – Cyprus, Solomon Islands	91
4.4.3	Fluids and residual mineral phases – rutile, Sunda arc samples.....	93
4.4.4	Residual phases – amphibole, Papua New Guinea.....	95
4.4.5	Basalts and their boninitic siblings	98
4.5	Conclusions.....	99
5	CONCLUDING REMARKS	101
6	ACKNOWLEDGEMENTS	105
7	REFERENCES	107

INDEX OF FIGURES

Figure 1-1: Neutron capture cross sections for Ti, Sm, Gd and Hf.....	7
Figure 1-2: Correlation of $\delta^{49}\text{Ti}$ and SiO_2 -content.....	12
Figure 1-3: Mass-depended Ti isotope variations in meteorites. Meteorite group of the respective data point is found on the left side of the figure.	13
Figure 1-4: Nucleosynthetic Ti data for various solar system materials.....	15
Figure 1-5 a and b: Mass-independent Ti isotope variations	16
Figure 2-1: Elution curves for Ca, Ti, V, and Cr of the initial chemistry.	21
Figure 2-2: Complete elution curve for chemistry and clean-up.	22
Figure 2-3 a and b: a) Schematic chemical separation and b) yield test results.....	23
Figure 2-4 a and b: $\delta^{49/47}\text{Ti}_{\text{OL-Ti}}$ versus f_{sample}	28
Figure 2-5 a and b: Determined $\delta^{49}\text{Ti}$ Ca-doped $1\mu\text{g/mL}$ Ti Col-Ti solutions	29
Figure 2-6: Comparison between Siebert et al., (2001) and Compston and Oversby (1969)..	34
Figure 2-7: Drift of ^{49}Ti with time when using X-cone (a) and normal cone (b).....	36
Figure 2-8: Cup configuration of IC- and ID set up.....	37
Figure 2-9: Long term precision and accuracy of the Ti method.....	38
Figure 3-1: Departure from the terrestrial fractionation line expressed as $\Delta^{17}\text{O}$	40
Figure 3-2: Multiple impact origin of the Moon.	41
Figure 3-3: Formation model of the lunar crust	42
Figure 3-4: CI-Chondrite normalized REE element distribution of various lunar lithologies.	43
Figure 3-5: Classification of lunar rocks based on TiO_2 vs. $\text{Mg} / (\text{Mg} + \text{Fe})$	44
Figure 3-6 a and b: Sampling bias and neutron capture effects.	48
Figure 3-7: Measured Ti isotope compositions of lunar samples.	52
Figure 3-8: Intermediate precision (long term reproducibility)	53
Figure 3-9 a-c: Estimating the $\delta^{49}\text{Ti}$ of KREEP based on HFSE/element ratios	55
Figure 3-10 a-d: LMO solidification modelling results.	59
Figure 3-11 a and b: Results for partial melting, fractional crystallisation and AFC.	61
Figure 3-12: Modelled Ti isotope composition and Ta/Hf during partial melting.....	64
Figure 3-13 a-c: Plots of a) $\delta^{49}\text{Ti}$ vs. MgO/TiO_2 , b) $\delta^{49}\text{Ti}$ vs. Ta/Hf and c) $\delta^{49}\text{Ti}$ vs. U.....	68
Figure 3-14 a and b: Ti isotope compositions vs. other stable isotope systems.....	72
Figure 4-1: Processes at subduction zones.....	77
Figure 4-2: Intermediate precision of the analysed reference materials.	87
Figure 4-3: Ti isotope composition of analysed samples relative to SiO_2	89
Figure 4-4 a - d: Ti isotope composition vs. trace element ratios.	92

Figure 4-5: PRIMA-normalised trace element pattern for the New Britain sample suite..... 95
Figure 4-6 a and b: Main, trace element and Ti isotope data for New Britain samples..... 97
Figure 4-7 a and b: $\delta^{49}\text{Ti}$ vs. SiO_2 98

INDEX OF TABLES

Table 2-1: Calibration results for Col-Ti and the Cologne Ti double spike.	26
Table 2-2: Results of reference materials with varying sample to spike ratios (given as the fraction of sample in the sample-spike mixture - f_{sample}).	27
Table 2-3 Amount of Ca, $^{44}\text{Ca}/^{47}\text{Ti}$ and resulting $\delta^{49}\text{Ti}$ of Ca-doped Col-Ti solutions.	28
Table 3-1: Summary of reference materials and measured samples.	51
Table 3-2: Relevant mineral assemblages for Trace element and isotope modelling.	56
Table 3-3: Values used in the models.	58
Table 4-1: Ti isotope compositions of subduction zone derived samples.	85
Table 8-1: Appendix, used trace elements (lunar samples).	122
Table 8-2: Appendix, used trace element data in the arc study.	123

CHAPTER 1
INTRODUCTION

1.1 Stable isotope systematics

Isotope analysis relies heavily on the use of mass spectrometers. The precursors of the modern mass spectrometer, the first mass spectrographs were described by Thomson (1914) and Aston (1919), respectively. Constant progress over the next 15 to 20 years led to the development of the double focusing mass spectrometer by Mattauch and Herzog (1934) and Alfred Nier (1940), who refined the construction of mass spectrometers for routine analysis. The next 20 years were marked by discoveries of various variations in isotope compositions of for instance hydrogen and sulphur (see review by Jacob Bigeleisen 1965). The first step towards automation was published by Gerald Wasserburg *et al.*, (1969), who built the first mass spectrometer with digital data registration. Over the coming decades, the use of mass spectrometers allowed for greater insights into terrestrial and extra-terrestrial natural processes through numerous stable and radioactive isotope systems. As an example, three (coupled) stable isotope systems will be briefly introduced and summarised.

Hydrogen and Oxygen – H and O: The two constituents of water, oxygen and hydrogen, show similar depletion in their respective heavy isotopes (^2H , *i.e.*, D and ^{18}O) in freshwater relative to rocks and organic products. Coupled variations in $^{18}\text{O}/^{16}\text{O}$ and the deuterium to hydrogen ratio (D/H), the so called Global Meteoric Water Line (first described by Harmon Craig, 1961) defines a linear array of coupled O and H isotope variations in water. Closed off basins show a clear offset towards heavier O isotope compositions, which is an effect of precipitation (Allègre, 2008 and references therein; Craig, 1961). Deuterium isotope variations in meteoric waters show variations in the hundreds of permil (Hoefs, 2009), with ocean water showing a very narrow range. Coupled variations in O and H can help trace the water cycle and different terrestrial reservoirs (ice, freshwater, rain water), and either coupled or isolated studies of H, D and O can trace *e.g.*, salinity, temperature, humidity (Allègre, 2008 and references therein). Variations in O isotope compositions in igneous rocks can be attributed to contamination with crustal rocks or hydrothermal alteration (Allègre, 2008). More so, the variation of unaltered rocks, basalts or ultrabasic rocks, are not only constant (at around 5.5 ‰) but also analogous to the average value of meteorites (Allègre, 2008 and references therein; Taylor, 1974 and references therein). While the O isotope variations in basalts and seawater show only very little variation (Hoefs, 2009), O isotope variations in water and some geological reservoirs (metamorphic and sedimentary rocks) can be fairly large (10s of permil) (Allègre, 2008 and

references therein; Taylor, 1974). Given the heterogeneity in O isotope compositions in solar system bodies, variations in O isotope composition further showed a genetic relationship between Earth and Moon, as both planetary bodies have an identical oxygen isotope compositions (Herwartz *et al.*, 2014; Wiechert, 2001). Mass-independent effects in meteoritic O and terrestrial ozone were first discovered by Clayton *et al.*, (1973) and Thiemens and Heidenreich (1983) observed in terrestrial ozone. In contrast to these ‘traditional isotope systems’, non-traditional isotope systems in this case relates to the novel character of the methods. The development of these non-traditional isotope systems was previously hindered by technical limitations related to instrumentation. This implies, but is not limited to, insufficient precision and sensitivity of the method and the instruments. Many of these systems came with additional pitfalls in for instance their abundance, redox behaviour or simply in the observable variations. For a detailed review on the evolution of non-traditional isotope analysis techniques in the past two decades, the reader is referred to the relevant literature (Albarède and Beard, 2004; Teng *et al.*, 2017). Here, I will briefly describe the state of the art related to the non-traditional stable isotope systems V and Fe, which like Ti, can be fractionated by similar processes (melting and magmatic differentiation, changes in redox conditions) and mineral phases (oxides) (*e.g.*, Hopkins *et al.*, 2019; Prytulak *et al.*, 2013; Sossi *et al.*, 2016; Weyer *et al.*, 2005).

Vanadium – V: Vanadium is a moderately incompatible and strongly redox dependent transition element (Prytulak *et al.*, 2013). The presence of only two isotopes with a very large difference in their natural abundances makes it challenging to use V isotopes as a tracer (^{50}V with 0.25 % and ^{51}V with 99.75 %– Berglund and Wieser, 2011; Nielsen *et al.*, 2011; Prytulak *et al.*, 2011). This is particularly difficult as regular detectors ideally operate within an abundance ratio below ~ 100 , *i.e.*, the ratio of one isotope to another can be measured with higher precision if the ratio is less than 100. The coupled use of detection methods, ion counter and Faraday cup, limits precision in V stable isotope analysis usually to ± 1 ‰ (Nielsen *et al.*, 2011). Additionally, double spike isotope dilution cannot be used here (V only has two isotopes), which limits the precision of the method even further. Another pitfall due to the low abundance of ^{50}V , are isobaric interferences, *i.e.*, isotopes of another element with the same mass (^{50}Ti and ^{50}Cr on ^{50}V . Nielsen *et al.*, 2011; Prytulak *et al.*, 2011). These interferences cannot be resolved and V isotope analysis consequently requires an highly efficient chemical separation procedure (Nielsen *et al.*, 2011). Prytulak *et al.*, (2011) found that V isotope compositions are very robust against alteration processes, which makes them a viable tracer for ancient mantle and mantle

derived melts. Prytulak *et al.*, (2013) report the V isotope composition of the Allende meteorite, terrestrial basalts and more evolved silicates. While the Allende meteorite is shown to be enriched in the light isotopes compared to terrestrial materials, Earth and Moon have an identical V isotope composition after correction for secondary neutron capture of the latter (Hopkins *et al.*, 2019; Prytulak *et al.*, 2011, 2013).

Iron – Fe: Iron is a fairly abundant, siderophile element with a quite complex chemical behaviour (see Dauphas *et al.*, 2017 for a review and references therein). Its abundance in terrestrial reservoirs varies corresponding to its valence, metallic Fe⁽⁰⁾ is enriched in the core, whereas ferrous (Fe²⁺) and ferric (Fe³⁺) are preferentially enriched in the mantle and the crust, respectively (Dauphas *et al.*, 2017 and references therein). Variations in iron isotope compositions can occur during fractional crystallisation of Fe-bearing minerals and redox cycling of Fe. Further significant Fe isotope variations are also found in some high-temperature samples (Beard and Johnson, 2004 and references therein; Johnson *et al.*, 2004). Variations of Fe isotope compositions in lunar samples suggest fractionation via partial melting, as well as a chemical kinship between the Bulk Silicate Earth and the Moon (Poitrasson *et al.*, 2004, 2019; Sossi *et al.*, 2016; Sossi and Moynier, 2017; Weyer *et al.*, 2005). This homogeneity of Fe isotope compositions may go even further, as Weyer *et al.*, (2005) found that Martian meteorites, eucrites (stony meteorite, origin: Vesta) and pallasites (stony-iron meteorites thought to originate from the core-mantle boundary of differentiated asteroids) have the same Fe isotope composition within uncertainty as Earth’s mantle. This would suggest a very homogenous distribution of Fe isotopes in the solar system.

1.1.1 Mass Fractionation – First principles

Mass fractionation, the physical-chemical process driving variations in stable isotope composition, describes the process of partitioning of isotopes of the same element between two phases with different isotopic ratios. A measure of the magnitude of this partitioning can be expressed as the fractionation factor α_{A-B} :

$$\alpha_{A-B} = \frac{R_{i,j}^A}{R_{i,j}^B} \quad 1-1$$

Where $R_{i,j}$ is the corresponding isotopic ratio of i over j of phase A or B , respectively. In natural systems, fractionation can be produced by a number of processes such as phase equilibrium, unidirectional reactions or radioactive decay and particle irradiation (Dauphas and Schauble, 2016). As such, observations from these natural systems allow a set of qualitative rules:

- Equilibrium fractionation between two phases decreases with increasing temperature (proportional to $1/T^2$),
- the degree of fractionation scales with the relative mass difference. Whereas the mass difference for H and D is roughly 50%, it is less than 5% for ^{47}Ti and ^{49}Ti ,
- in equilibrium, the heavier isotope shows a preference to the site with the stiffest chemical bond, which tends to increase with the oxidation state. Conversely, lighter isotopes favour covalent bonds and higher coordination numbers (Schauble, 2004; Sharp, 2007).

For example, during ilmenite/melt equilibration, ilmenite will incorporate lighter isotopes of Ti in its VI-fold site. The silicate melt will prefer heavier Ti isotopes, as this element is coordinated in IV to V fold in this phase (Alderman *et al.*, 2014; Leitzke *et al.*, 2018; Mysen and Richet, 2019). Assuming a distribution of the isotopes over all possible sites or positions, the equilibrium constant K_{eq} is related to the fractionation factor α – or the degree of fractionation – by the following relationship (Sharp, 2007):

$$\alpha = K_{eq}^{1/n} \tag{1-2}$$

where n is the number of atoms exchanged. As mentioned earlier, n equals unity in most cases so that this expression can be simplified too:

$$K_{eq} = \alpha \tag{1-3}$$

With these first principles, α can be further investigated using statistical mechanics (Schauble, 2004; Sharp, 2007). Considering fractionation to be a reaction at equilibrium, it is possible to calculate the Gibbs free energy and related to K_{eq} through:

$$\Delta G_{Rxn}^0 = -RT \ln(K_{eq}) \quad 1-4$$

$$K_{eq} = e^{\left(\frac{-\Delta G_{Rxn}^0}{RT}\right)} \quad 1-5$$

A molecule consisting of two isotopes of the same mass share a bond best approximated by a spring. The two isotopes vibrate towards and away from each other. The vibrational energy ν of this isotope doublet can be calculated using:

$$\nu = \frac{1}{2\pi} \sqrt{\frac{k_s}{\mu}} = \frac{1}{2\pi} \sqrt{k_s \left(\frac{1}{m_a} + \frac{1}{m_b}\right)} \quad 1-6$$

where k_s is the spring constant, μ the reduced mass of the molecules a and b , and m_a and m_b the masses of each isotope, respectively. Substituting a lighter isotope for a heavier one increases the reduced mass μ while leaving the spring constant unchanged. This leads to a decrease in vibrational energy. It follows that a molecule with two heavy isotopes vibrates slower than a molecule with a heavy and a light isotope, which in turn also vibrates slower than a molecule with two light isotopes. Vibrational energy quanta are by far the dominant factor, even though rotational and translational energy quanta contribute as well to the total energy of a molecule. As the latter two are negligible, calculating equilibrium stable isotope fractionation factors requires only the consideration of the vibrational energy quanta (Schauble, 2004). Given the level of precision, quantum mechanical calculations are not required to predict fractionation behaviour during fractional crystallisation of a melt, but can be approximated and expressed using a Rayleigh distillation model

$$R_{sample}^{i/j} = f R_{sample}^{i/j} \alpha^{-1} \quad 1-7$$

with R being the isotope ratio of i normalised to j of the sample and the reference material, respectively, f the amount of the element remaining in the system and α the fractionation factor.

1.1.2 Mass-independent isotope effects

Whereas mass-dependent isotope fractionation effects in a three isotope system follow linear fractionation trends in direct relation to the difference between the masses of each isotope, mass-independent effects are departures from this trend (Clayton *et al.*, 1973; Thiemens and Heidenreich, 1983). A more in-depth treatment of the mathematical background of mass fractionation can be found in the literature (Dauphas and Schauble, 2016; Schauble, 2004; Sharp, 2007). As the focus of this study are mass-dependent variations of Ti isotopes, only a brief review of a few examples will be given in this monograph.

Thiemens and Heidenreich (1983) observed mass-independent effects in atmospheric ozone, most likely linked to photolytic decomposition and molecular symmetry. An “asymmetric” ozone molecule (such as $^{17}\text{O}^{16}\text{O}^{18}\text{O}$) is much more abundant than a “symmetrical” ozone molecule (for instance $^{16}\text{O}^{16}\text{O}^{16}\text{O}$), leading to a selective fractionation that is independent of mass (*e.g.*, Allègre, 2008; Thiemens, 2006 and references therein). Mass-independent fractionation also occurs through kinetic effects that result from biological processes, as it requires “less energy” to use low mass isotopes in biological processes (like preferential use of ^{12}C over ^{13}C ; Hoefs, 2009). Another major mass-independent fractionation process, especially in cosmochemistry and the analysis of extra-terrestrial samples, is (secondary) neutron capture.

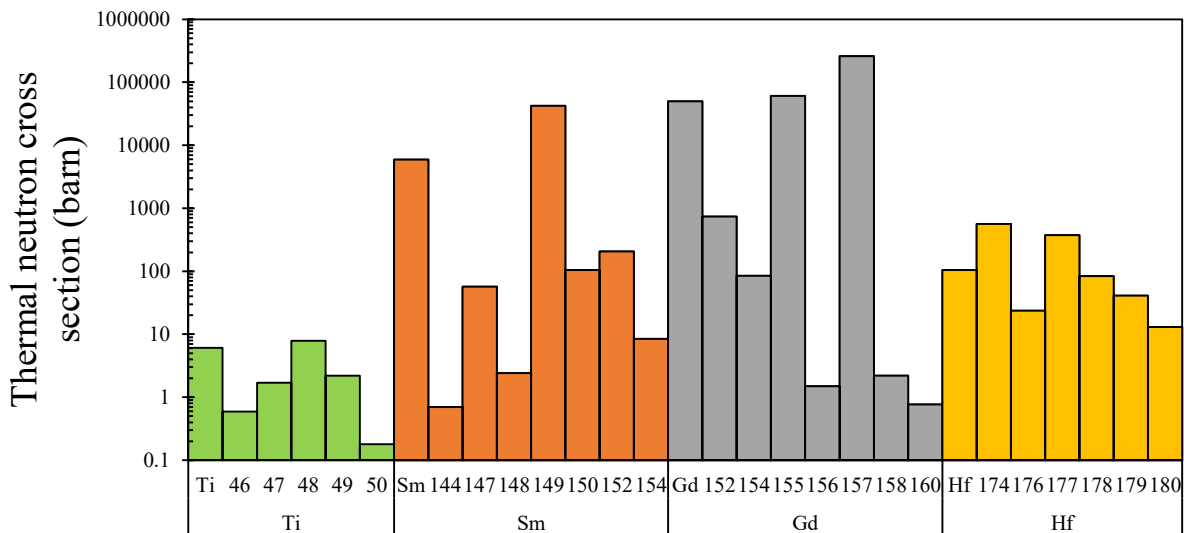


Figure 1-1: Neutron capture cross sections for Ti, Sm, Gd and Hf. Mean cross section for each element is shown as well as data for each isotope. While Gd or Sm are more sensitive towards neutron capture, the abundance of Ti is far higher. Cross section data compiled from the IAEA database (Kopecky *et al.*, 2001)

While silicon burning during nuclear fusion in the interior of stars produces all isotopes up to ^{56}Fe , isotopes heavier than ^{56}Fe require more energy than what is released by their formation (Clayton, 2003). The main nucleosynthetic process for the heavier elements is neutron capture, with the process itself being split into the slow or s-process, and the rapid or r-process (Demtröder, 2010). The tendency of an isotope of a given element to capture neutrons in secondary or tertiary processes is quantified by its neutron capture cross section, given in barn (b) or milli-barn (mb), where 1 barn is an area of space ($1\text{b} = 10^{-28} \text{ m}^2 = 1000 \text{ mb} = 10^{-31} \text{ m}^2$). Generally, the larger this area, the higher is the probability of capturing a neutron of a given velocity, which is given in electron Volt (eV). Sensitive elements for neutron capture in the thermal neutron range of 0.025 eV and 0.2 eV are for instance Sm and Gd (Figure 1-1; Sprung *et al.*, 2010; Zhang *et al.*, 2012). This is most relevant for extra-terrestrial material, as these materials are not shielded from cosmic radiation and neutron bombardment (*e.g.*, Ti, Cr; Trinquier *et al.*, 2009). However, for this study, these effects are negligible (Deng *et al.*, 2018b; Greber *et al.*, 2017b), and the reader is referred to the relevant literature on this topic (Dauphas and Schauble, 2016; Thiemens, 2006; Watkins *et al.*, 2017)

1.1.3 Reference materials in stable isotope geochemistry

In stable isotope geochemistry, data is usually given as an isotopic ratio relative to a reference material. This material can be a well characterised rock standard or an artificial material, for instance a processed piece of high purity metal (Millet and Dauphas, 2014; Teng *et al.*, 2017). In order for a given material to be suitable to be used as reference material or isotopic reference material, it must meet a number of conditions:

- it needs to be assured that the material is isotopically homogenous within current precision and it should remain so as precision improves,
- it should be available for distribution,
- ideally, it consists of a pure chemical compound, being able to either be diluted or dissolved in acids,
- its isotopic composition should lie within natural variability,
- the choice of relative notation should be agreed and followed by the analytical community,

- last but not least, its isotopic composition should be precisely known for all its isotopes to a high degree of precision to prevent anomalies.

A detailed review on terrestrial reference material is given by Jochum and Enzweiler (2014 and references therein), as well as the Committee on Reference Materials of the International Organisation for Standardisation (REMCO / ISO). Most common notation in stable isotope geochemistry is the delta value δ^i :

$$\delta^i(R_{i,j \text{ sample}})(\text{per mil}) = \left(\frac{R_{i,j \text{ sample}}}{R_{i,j \text{ Reference}}} - 1 \right) 10^3 \quad 1-8$$

where $R_{i,j}$ is the isotope ratio being analysed, i is the isotope in numerator and j the one in the denominator. Furthermore, it is normalized to the corresponding isotopic ratio of an IRM. In this monograph the mass-dependent Ti isotope fractionation in natural samples, will be expressed as the deviation of the $^{49}\text{Ti}/^{47}\text{Ti}$ ratio of the sample relative to the Origins Lab Ti reference material (OL-Ti described in Millet and Dauphas, 2014) given in permil (henceforth $\delta^{49}\text{Ti}$):

$$\delta \left(^{49}\text{Ti}/^{47}\text{Ti}_{\text{sample}} \right) (\text{per mil}) = \left(\frac{\left(\frac{^{49}\text{Ti}}{^{47}\text{Ti}} \right)_{\text{sample}}}{\left(\frac{^{49}\text{Ti}}{^{47}\text{Ti}} \right)_{\text{OL-Ti}}} - 1 \right) \times 10^3 \quad 1-9$$

Nucleosynthetic anomalies are expressed as ε or μ values and are calculated in a similar manner. Due to their smaller scale, the deviation is given in parts per ten thousand for ε or parts per million for μ . However, these anomalies only show after correction for instrumental (and natural) mass bias, which is why the ratio used for correction is included in the equation. For Ti, $^{49}\text{Ti}/^{47}\text{Ti}$ is used, as these two isotopes do not have any significant isobaric interferences, unlike ^{46}Ti and ^{48}Ti (^{46}Ca and ^{48}Ca) and ^{50}Ti (^{50}V and ^{50}Cr) and the observed effect is the largest for ^{50}Ti , as such, nucleosynthetic studies focus on this isotope.

$$\varepsilon^{50}\text{Ti}_{\text{sample}} \left(\frac{^{49}\text{Ti}}{^{47}\text{Ti}} \right) (\text{parts per ten thousand}) = \left(\frac{\left(\frac{^{50}\text{Ti}}{^{47}\text{Ti}} \right)_{\text{sample}}}{\left(\frac{^{50}\text{Ti}}{^{47}\text{Ti}} \right)_{\text{OL-T}}} - 1 \right) \times 10^4 \quad 1-10$$

$$\mu^{50\text{Ti}}_{\text{sample}} \left(\frac{^{49}\text{Ti}}{^{47}\text{Ti}} \right) (\text{parts per million}) = \left(\frac{\left(\frac{^{50}\text{Ti}}{^{47}\text{Ti}} \right)_{\text{sample}}}{\left(\frac{^{50}\text{Ti}}{^{47}\text{Ti}} \right)_{\text{OL-}}} - 1 \right) \times 10^6 \quad 1-11$$

An analysed sample with an identical isotopic composition as the reference material would lead to a value of 0, any deviation from this 0 value is a consequence of mass fractionation. Once constrained, the isotope composition of reference materials can be used to gauge the long term accuracy of a method.

1.2 Titanium elemental and stable isotope systematics

1.2.1 Geochemical behaviour of Ti

Titanium is a refractory, lithophile during core-mantle segregation and fluid-immobile element that has five isotopes, all of which are stable. Its electron configuration (Ar (3d²4s²)) locates it in the IVB group of the periodic table, and the other elements in that group, the so-called “titanium metals” group, consist of Hf and Zr. In similar fashion to the (expanded) high field strength element group (HFSE – Nb, Ta, Hf, Zr, Mo and W), Ti typically exhibits a high oxidation state (4+) coupled to a small ionic radius (Clayton, 2003; McDonough *et al.*, 1992; 0.42 to 0.61 Å in four-fold and six-fold coordination, respectively; Mysen and Richet, 2019 and references therein). The average coordination of Ti in silicate melts is V-fold (Alderman *et al.*, 2014; Mysen and Richet, 2019), while Ti is most commonly emplaced in crystalline structures in VI-fold (Ti-bearing oxides, titanite, amphiboles, most silicates, *e.g.*, Leitzke *et al.*, 2018; Mysen and Richet, 2019), and more rarely in IV-fold coordination (pyroxenes; Leitzke *et al.*, 2018; Simon *et al.*, 2014). By far the most common Ti-rich minerals are rutile or ilmenite, which also control the budget of the other high field strength elements (or HFSE, Münker, 2010; Mysen and Richet, 2019). The most prevalent oxidation state of Ti is Ti⁴⁺, *e.g.*, in rutile, ilmenite or ulvospinel. However, under more reducing conditions (*i.e.*, lower oxygen fugacity) the fraction of Ti³⁺ in the bulk Ti budget of a rock or mineral increases (Toplis and Carroll, 1995). This may be possible in reduced planetary bodies like the Moon or in CAI inclusions found in chondrites (Simon *et al.*, 2007), where samples are known to have equilibrated at oxygen

fugacities below the iron-wüstite (Fe-FeO) redox equilibrium (Wadhwa, 2008). Moreover, recent Ti K-edge XANES studies carried out on lunar samples and experimental analogues, revealed that larger amounts of Ti^{3+} (up to 40 %) may be present in rutile, armalcolite and clinopyroxene under lunar redox conditions (Simon and Sutton, 2017, Leitzke *et al.*, 2018). But while modelling predicts values of around 10% Ti^{3+} , direct measurements have shown higher limited amounts of trivalent Ti in lunar samples (up to 30%; Simon *et al.*, 2014; Simon and Sutton, 2017). This would mean that Ti isotopes can be used as a tracer for magmatic processes over a large range of redox-conditions, as tetravalent Ti is the most likely predominant redox species of this element in most geological materials. As such, the mineral-melt isotope fractionation behaviour of Ti is likely representative of the element's behaviour as a whole.

1.2.2 Titanium isotopes as a tracer of magmatic differentiation

Titanium stable isotope systematics have been increasingly used to investigate magmatic processes on Earth and the Moon (Millet *et al.*, 2016; Millet and Dauphas, 2014). Titanium has five stable isotopes, with ^{48}Ti by far the most abundant (Berglund and Wieser, 2011): The two lightest Ti isotopes, ^{46}Ti and ^{47}Ti , are primarily produced during oxygen and silicon burning during stellar nucleosynthesis (mole fraction: 0.0825 and 0.0744, respectively). The isotopes ^{48}Ti and ^{49}Ti (mole fraction: 0.737 and 0.0541), primarily exist as decay products from ^{48}Cr and ^{49}Cr , respectively, which result from stellar explosions. The process for the production of ^{50}Ti takes place in type Ia supernovae (mole fraction: 0.0519; Berglund and Wieser, 2011; Clayton, 2003). According to stable isotope theory, ions that adopt higher spatial coordination in phases form stronger, stiffer bonds and as such, these sites show a preference for lighter isotopes of a given element (Schauble, 2004). As such, because Ti shows higher spatial coordination in most Ti-rich minerals (VI-fold in rutile, ilmenite, etc.) compared to silicate melt, during fractional crystallisation or partial melting, the solid mineral will tend to be enriched in lighter Ti isotopes, whereas the melt becomes gradually enriched in heavier Ti isotopes (Millet *et al.*, 2016). On a first order basis this expectation would imply that a silicate melt should show progressively higher $\delta^{49}Ti$ with increasing SiO_2 content and decreasing MgO content, which appears to be the case (Millet *et al.*, 2016). Moreover, Deng *et al.*, (2019) identified a second trend comprised of plume-derived lavas. This array showed increasingly high $\delta^{49}Ti$ at even lower SiO_2 -content (see Figure 1-2). Deng *et al.*, (2019) argued that the steeper trend shown by Ocean Island Basalt (OIB) samples in $\delta^{49}Ti$ vs. SiO_2 space is due to delayed Fe-Ti oxide saturation due to lower

oxygen fugacities (fO_2) of OIB relative to arc magmas, which together with extensive olivine and plagioclase crystallization leads to OIB becoming enriched in TiO_2 compared to MORB and arc lavas at similar SiO_2 contents. Once the OIB melt becomes Fe-Ti oxide saturated, the magnitude of change in the $\delta^{49}Ti$ of the melt with SiO_2 content is quite high, leading to the steeper slope in $\delta^{49}Ti$ vs. SiO_2 space. Millet *et al.*, (2016) found no significant Ti isotope variations in Island Arc Basalts, MORB and metamorphic rocks over a restricted range of SiO_2 contents (44 to 50 wt.%).

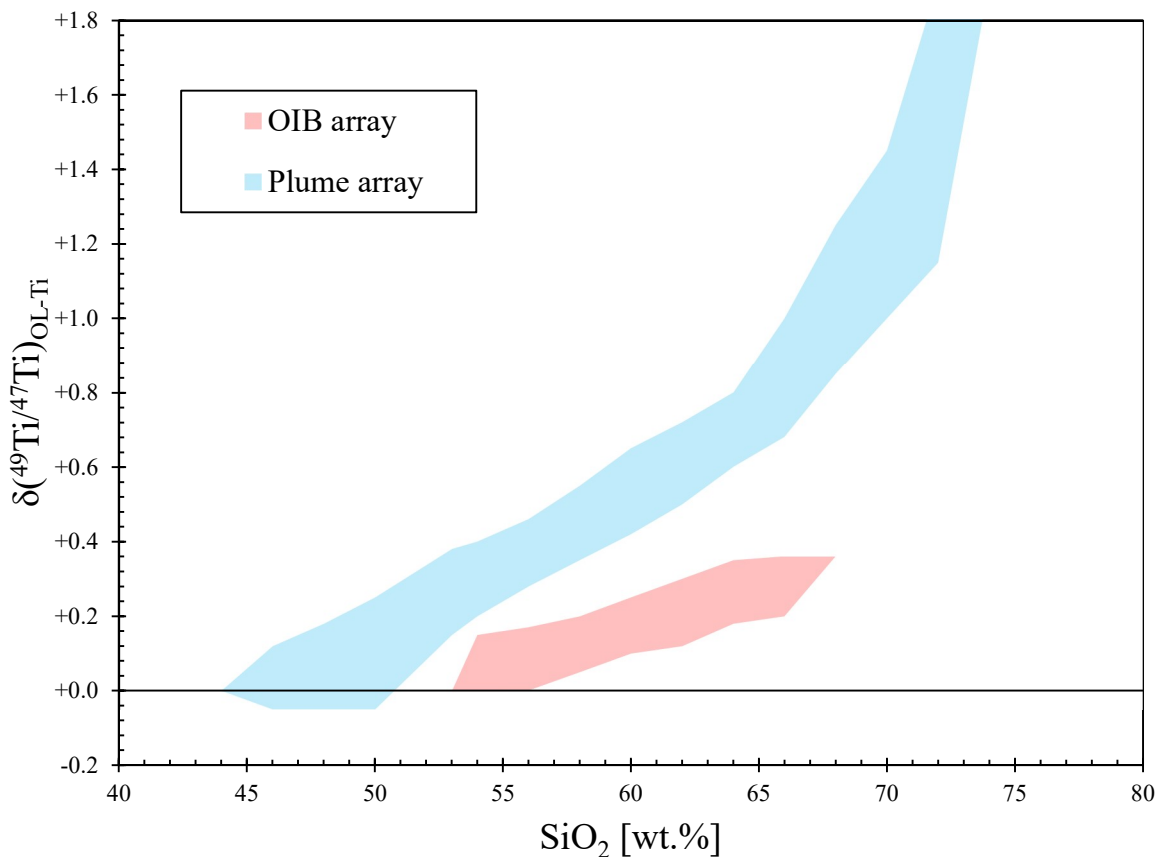


Figure 1-2: Correlation of $\delta^{49}Ti$ and SiO_2 -content. Heavier Ti isotope compositions show correlation with silica content. The red field was first constrained by Millet *et al.*, (2016), expanded and complimented by the “plume” field by Deng *et al.*, (2019)

This suggests that Ti is not mobile in F- or Cl-bearing fluids across the mantle wedge during dehydration of subducted lithosphere. The effect of common silicate minerals (such as olivine, clino- and orthopyroxene) on Ti isotope fractionation behaviour appears to be negligible. Johnson *et al.*, (2019) split fresh lavas of the Kilauea Iki volcano (Hawaii) into a dense oxide portion and a less dense silicate portion using density separation. While the oxide-fraction displays expectedly lower values of $\delta^{49}Ti$, slightly lower than the estimated bulk fractionation

factor by Millet *et al.*, (2016), the silicate portion does not show a resolvable variation in $\delta^{49}\text{Ti}$ relative to the bulk composition of these lavas. The same seems to hold true for mineral separates from lunar samples (Mandl *et al.*, 2018). Furthermore, these results are consistent with ab-initio modelling by Wang *et al.*, (2019), who found no resolvable Ti inter-mineral isotope fractionation between in olivine, orthopyroxene and pyrope garnet relative to their clinopyroxene (used as unfractionated Ti isotope baseline), and negative Ti isotope compositions in their modelled oxide phases.

1.2.3 Extra-terrestrial, mass-dependent isotope systematics

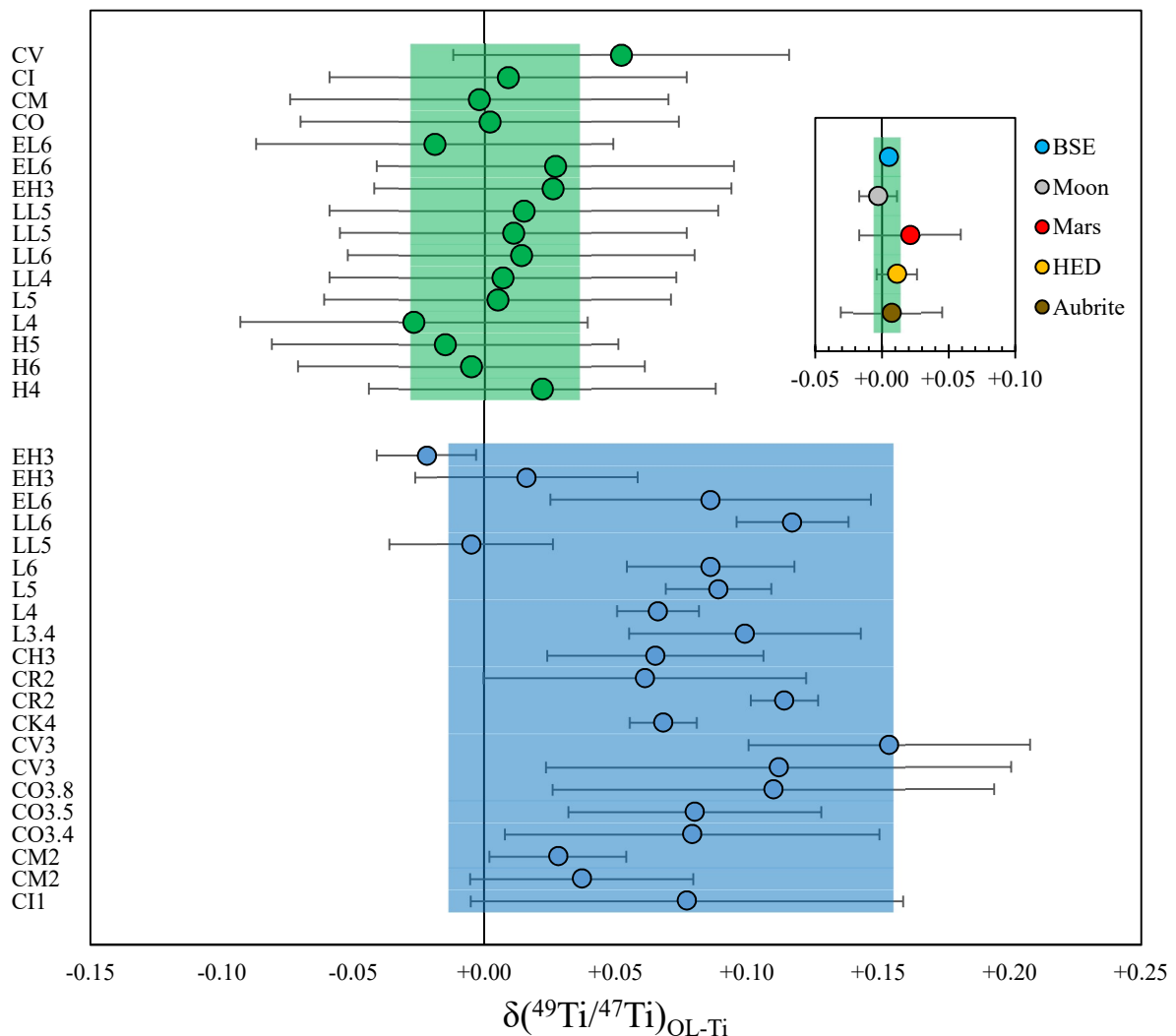


Figure 1-3: Mass-dependent Ti isotope variations in meteorites. Meteorite group of the respective data point is found on the left side of the figure. Blue symbols represent data from Deng *et al.*, (2019) and their chondritic average (blue box), green is data by Greber *et al.*, (2017b) and their chondritic average. Uncertainties recalculated to 2 s. Inset shows bulk $\delta^9\text{Ti}$ of planetary bodies by Greber *et al.*, (2017b). Uncertainty of chondritic value is taken directly from Greber *et al.*, (2017b) and here represent the 95% c.i.

When constraining the $\delta^{49}\text{Ti}$ of meteorite samples and lunar samples, neutron capture correction during the double spike deconvolution is necessary (Greber *et al.*, 2017b), as evidenced by mass-independent effects in irradiated lunar samples (*e.g.*, Zhang *et al.*, 2012). Various groups of chondrites show a homogenous distribution in their Ti isotope composition in the respective study, but resolvable differences when compared to another (Figure 1-3; Deng *et al.*, 2018b; Greber *et al.*, 2017b). The chondritic average in the datasets from Deng *et al.*, (2018b) and Greber *et al.*, (2017b) overlap within two standard deviations, but show resolvable differences in their Ti isotope compositions when their 95 % confidence interval is considered. However, average values of the $\delta^{49}\text{Ti}$ for the Bulk Silicate Earth (BSE, $+0.005 \pm 0.005 \text{ ‰}$), lunar samples ($+0.004 \pm 0.010 \text{ ‰}$), the Howardite-Eucrite-Diogenite parent body (HED, potentially Vesta; $+0.011 \pm 0.021 \text{ ‰}$), Angrites ($+0.007 \pm 0.038 \text{ ‰}$) and Mars ($-0.003 \pm 0.014 \text{ ‰}$) are the same, within uncertainty, to the average chondritic value of Greber *et al.*, ($+0.004 \pm 0.010 \text{ ‰}$; 2017b). This is in contrast to other stable isotope data for refractory lithophile elements like Ca, and is most likely due to the different behaviour of Ti during condensation in the solar nebula (Greber *et al.*, 2017b).

1.2.4 Extra-terrestrial Ti isotope systematics and nucleosynthetic heritage

Mass-independent effects for Ti isotope compositions in inner solar system bodies are related to neutron capture effects and are expressed as $\epsilon^{50}\text{Ti}(^{49}\text{Ti}/^{47}\text{Ti})$, henceforth $\epsilon^{50}\text{Ti}$, (Equation 1-15, Figure 1-4 and 1-5 a and b). Variations in $\epsilon^{50}\text{Ti}$ can be extremely large in very refractory phases such as CAIs and pre-solar grains (Gerber *et al.*, 2017; Render *et al.*, 2019), due to various amounts of the precursor material from the latter mixed into the former. While $\epsilon^{50}\text{Ti}$ variations in various CAI-groups indicate large-scale transport of material in the solar system (Render *et al.*, 2019), the later formed chondrites formed distinct reservoirs that remained isolated from each other (Gerber *et al.*, 2017). Bulk inner solar system bodies also show significant large-scale variations (Leya *et al.*, 2008; Trinquier *et al.*, 2009; Zhang *et al.*, 2012). It is unlikely that this results from heterogeneous distribution of the solar nebula material (Trinquier *et al.*, 2009). The correlation between $\epsilon^{46}\text{Ti}(^{49}\text{Ti}/^{47}\text{Ti})$ and $\epsilon^{50}\text{Ti}(^{49}\text{Ti}/^{47}\text{Ti})$ found by Trinquier *et al.*, (2009) in a range of solar system materials points towards a well-mixed inner solar system (Figure 1-4), as the nucleosynthetic origin for ^{46}Ti and ^{50}Ti is different (oxygen

and silicon burning during stellar nucleosynthesis vs. production in a type Ia supernovae, respectively - cf. Clayton, 2003). However, the variability in the mass-independent Ti isotope composition on a planetary scale requires a process to impart this heterogeneity. Such a process may consist of thermal processing of the molecular cloud material where, for example, thermal event(s) in the early solar system fractionated moderately volatile elements potentially leading to loss of pre-solar silicates containing ^{46}Ti - ^{50}Ti -excesses (Trinquier *et al.*, 2009).

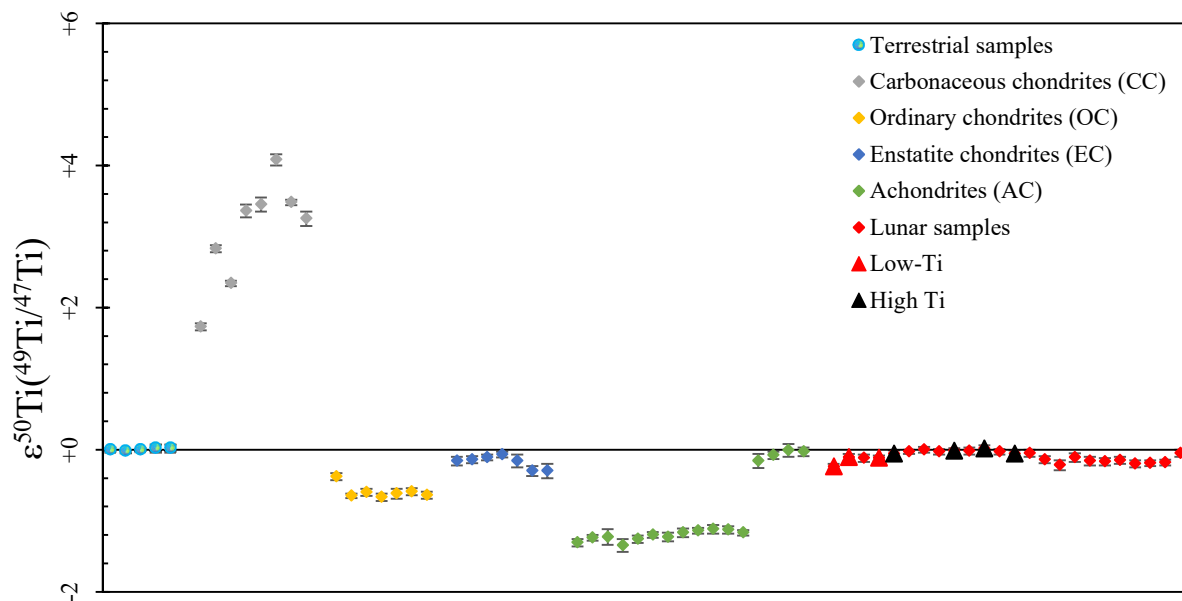


Figure 1-4: Nucleosynthetic Ti data for various solar system materials. Data show significant anomalies in some achondrites, ordinary and enstatite chondrites, data by Zhang *et al.* (2012). Samples from Earth and the Moon are the same within analytical uncertainty. See text for discussion of negative $\epsilon^{50}\text{Ti}$ values for lunar samples.

On a planetary scale, Ti can be used, for example, to constrain the homogeneity of the Earth-Moon System. Earth inherited its Ti isotopic composition from its building blocks. Any departure from the mass-independent fractionation line (Figure 1-5 a) would represent input from another source region. When studying the nucleosynthetic heritage of the Moon, however, secondary neutron capture effects need to be taken into consideration. A useful mean of control are the ratios between the isotopes of samarium or of gadolinium, which both show large neutron capture cross sections in the thermal and epithermal neutron range. Any correlation in an $\epsilon^{50}\text{Ti}(^{49}\text{Ti}/^{47}\text{Ti})$ vs. Sm or Gd isotope plot indicates the capture of secondary neutrons on the lunar surface. After correction for these effects, terrestrial and lunar samples show no resolvable differences in their $\epsilon^{50}\text{Ti}(^{49}\text{Ti}/^{47}\text{Ti})$. This similarity implies that either the Moon-forming impactor(s) had the same $\epsilon^{50}\text{Ti}(^{49}\text{Ti}/^{47}\text{Ti})$ as the proto-Earth (within 0.10 ϵ -units), or that somehow the Moon inherited material primarily from what is now the BSE. The former

hypothesis is unlikely, as during the chaotic period of planetary formation it is hard to envision that two such bodies share the same Ti isotopic composition. The most plausible scenario is a mixing process in the post impact magma disc, which likely homogenized material from the impactor and BSE (Zhang *et al.*, 2012).

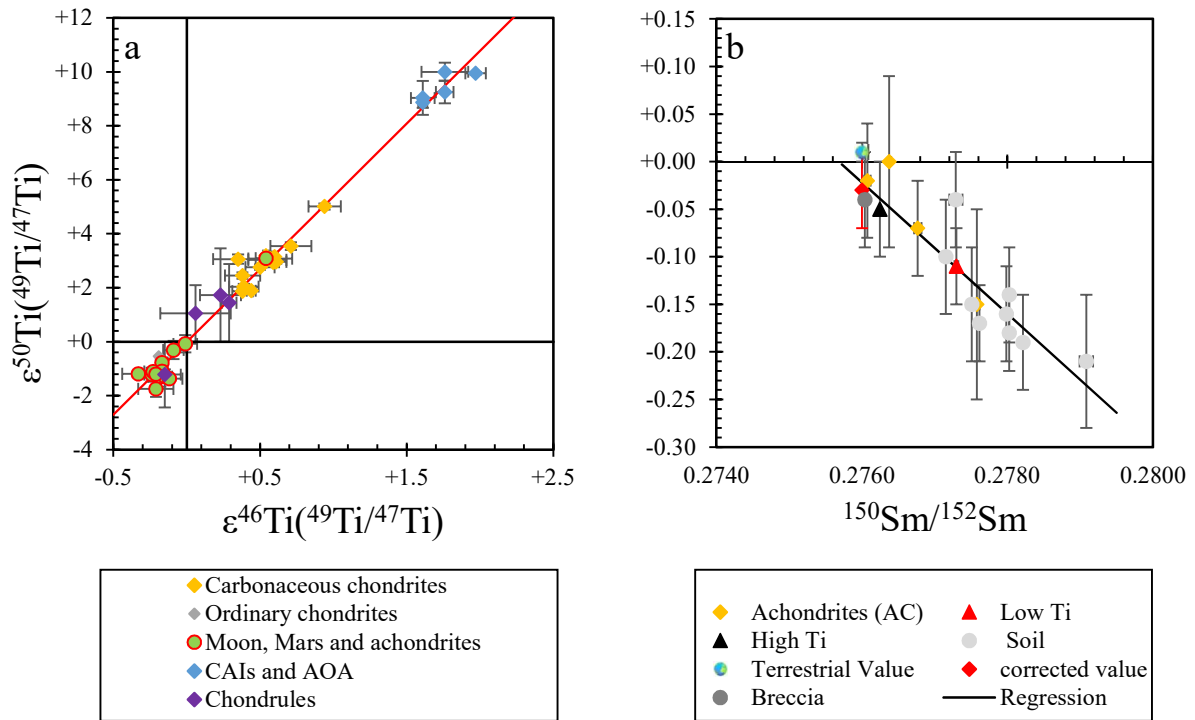


Figure 1-5 a and b: Mass-independent Ti isotope variations by Trinquier *et al.*, (2009) and Zhang *et al.*, (2012). Neutron capture effects in $\epsilon^{46}\text{Ti}$ and $\epsilon^{50}\text{Ti}$ reveal a correlation between the distinct reservoirs (a). Correlation of $\epsilon^{50}\text{Ti}$ with neutron capture monitor ($^{150}\text{Sm}/^{152}\text{Sm}$) reveal secondary neutron capture effects, after correction the value for Earth and Moon is identical within uncertainty.

1.3 Motivation and objectives

As seen in the previous section, Ti isotopes show resolvable variations in natural samples that stem from both mass-dependent and mass-independent processes. This monograph however focuses on mass-dependent Ti isotope variations to trace processes and components involved in the petrogenesis of terrestrial and lunar basaltic samples. Previous studies focussed on coupled Ti isotope - SiO₂ variations in terrestrial and extra-terrestrial samples (Deng *et al.*, 2018b, 2018a, 2019; Greber *et al.*, 2017a, 2017b; Millet *et al.*, 2016). However, the behaviour of the extended high field strength element group (here Th, U, W, Nb, Ta, Hf, Zr, and Lu) is often attributed with Ti-bearing phases such as rutile or ilmenite (Klemme *et al.*, 2005, 2006a). Thus, where there are extensive HFSE datasets available, it may prove more insightful to couple HFSE variations and Ti isotope variations in the same sample sets, rather than just to focus on their Ti isotope composition and silica content. By determining the Ti isotope composition of well characterised samples with available HFSE data, this study aims to provide insights into relevant processes (fractional crystallisation of Ti-bearing phases and partial melting in the presence or absence of these phases) and relevant components (*e.g.*, residual rutile, ilmenite, magnetite or potentially amphiboles, subducted sediment or mantle wedge) that fractionate Ti isotopes. The main objectives of my doctoral research were:

- I. Establish the Ti double spike method at the University of Cologne (Chapter 2).
 - a. Create and calibrate a double spike and an in-house reference material to ensure high precision and accuracy of the analysis of Ti isotope compositions as well as further develop a chemical separation procedure to separate elements of the extended HFSE group and Ti from other elements and from each other using ion chromatography,
 - b. further develop a measurement protocol on the University of Cologne's Neptune Plus MC-ICP-MS, and
 - c. develop the data reduction scheme.

- II. The lunar chapter (Chapter 3) uses the techniques and chemicals developed and calibrated in Chapter 2 to determine the Ti isotope composition of a representative set

of lunar samples. These data are then coupled with published high-precision isotope dilution HFSE data from the same samples to investigate the three primary reservoirs of lunar basalts,

- a. the last remainder of the Lunar Magma Ocean crystallisation (urKREEP),
- b. the ambient mafic lunar mantle and
- c. the ilmenite-bearing cumulates,

which are thought to be the source regions of KREEP-rich samples, low-Ti and high-Ti mare basalts, respectively. This study aims to constrain what process leads to Ti isotope fractionating in lunar samples with a special emphasis on high-Ti mare basalts (deep partial melting of an ilmenite bearing cumulate vs. shallow assimilation)

III. In chapter 4, in the same approach is applied to subduction zone related rocks (basalts, boninites and sediments). The Ti isotope composition of samples from subduction zones can potentially be influenced by:

- a. The nature of the subducted material (oceanic crust and overlying metasediments),
- b. the melting of the overlying (depleted) mantle wedge,
- c. the presence or absence of various residual Ti-bearing phases in the subducted slab and (although unlikely),
- d. fluid alteration

For this, a representative set of well characterised samples from different subduction zone settings was chosen, each of which is to varying degrees influenced by the aforementioned components. This study aims to constrain the influence of these components on coupled variations of Ti isotope composition, HFSE and other process-diagnostic trace element ratios.

CHAPTER 2
METHODS

2.1 Ion Chromatography / Chemistry

All chemicals used consisted of laboratory grade reagents. Residual trace element concentrations, *i.e.*, blank levels of concentrated acids (10 M HCl, 14 M HNO₃, 24 M HF) and other reagents (Merck 30 Vol.-% H₂O₂, Millipore™ MilliQ, henceforth MQ ultrapure water) were constantly monitored by the Cologne Clean Lab facility staff. Average residual Ti concentrations in all used chemicals never exceeded the 1 ng/mL threshold (sub-ng/g range). As such, any contribution to the Ti budget of all concentrated reagents used can be considered negligible given the amount of Ti present in the samples (usually 30 µg, 20 µg for two TiO₂-poor KREEP-rich lunar samples) analysed in these studies.

2.1.1 Calibration of the separation method

The chemistry used in this study is a modified version of the expanded high field strength element group chromatographic separation procedure outlined in studies by Münker (2001), Bast *et al.*, (2015), and most recently by Tusch *et al.*, (2019), who focussed on W. The main goal of the chemistry was to keep Ti in solution for as long as possible and avoid the complete dry down of the Ti aliquot during chemistry, in order to minimise the potential of sample loss or contamination. Initial tests were run on a three-column approach. In an initial step, a reference material, for instance BHVO-2 is digested. Prior to chemistry, a 5% aliquot of the digested solution is taken and doped with In. The sample is then loaded in a 1 M HCl - 2 Vol.-% H₂O₂ mixture onto the column. Matrix elements, as well as other HFSE, are separated as chemistry proceeds (See Figure 2-1). At each elution step of the chemistry, a further 5% aliquot is taken and doped with In. The doped aliquots are then measured on an ICP-MS for their elemental content, and using the results their absolute yield can be calculated. The elution curve shown in Figure 2-1 demonstrates a good separation of Ti from matrix elements especially from Ca, which is a major element, and its ineffective separation from Ti can result in two isobaric interferences on masses of Ti (⁴⁶Ca and ⁴⁸Ca on ⁴⁶Ti and ⁴⁸Ti). Traces of Cr and significant amounts of V are still found in the Ti-cut after the sample matrix is separated. As Cr and V can both result in isobaric interferences on Ti (namely on ⁵⁰Ti), their removal is essential and as

such, a clean-up is required. Double-spike analysis can neglect ^{50}Ti and any interferences on this by ^{50}V and ^{50}Cr , as ^{50}Ti is not part of the double spike deconvolution.

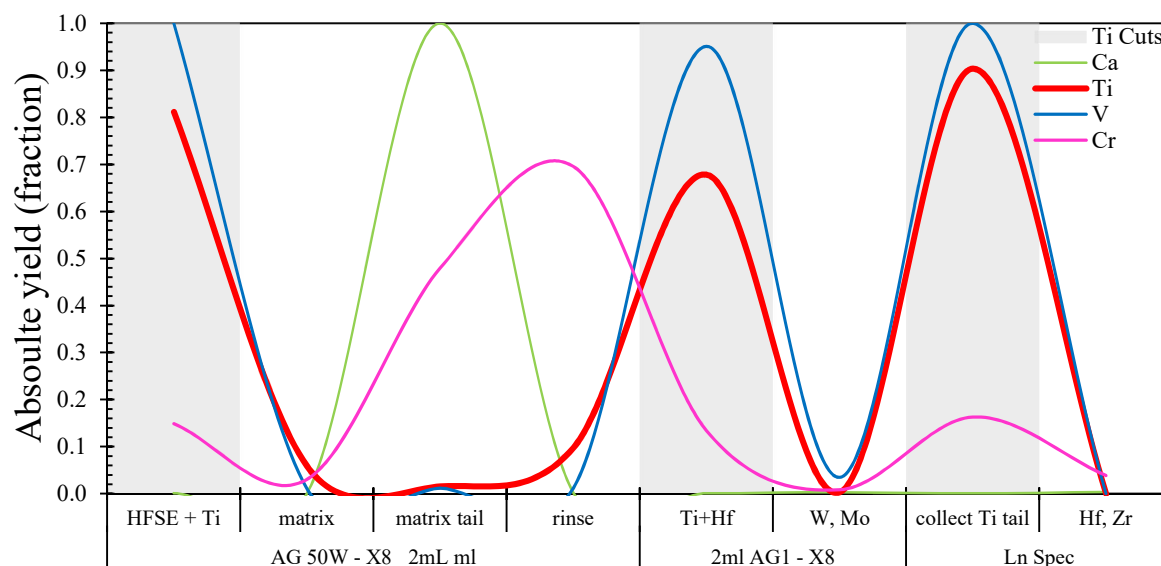


Figure 2-1: Elution curves for Ca, Ti, V, and Cr of the initial chemistry. Traces of Cr and large amounts of V remain in the Ti-cut

Nevertheless, the presence of matrix elements like V and Cr warrants a clean-up as matrix effects and other ionising effects can introduce second order mass bias or reduce sensitivity (Olesik and Jiao, 2017). This clean-up is carried out using AG1-X8 columns in 1 M HF - 0.33 M HCl. For this, the sample solution (1 M HCl - 2 Vol.-% H_2O_2) is converted into 1 M HF - 0.33 M HCl by adding concentrated 24 M HF and MQ water. In this solution, Ti adsorbs to the resin and Cr and V are rinsed off. Titanium is then eluted in 6 M HCl - 0.06 M HF. However, in instances where the Cr and V clean-up is not completely efficient, or simply out of precaution, the sample solution can instead be eluted in 1 M HCl - 2 Vol.-% H_2O_2 . The clean-up is then repeated, by adjusting the eluted sample solution to 1 M HF - 0.33 M HCl, and then loading the sample. After matrix elution, Ti is eluted in 6 M HCl - 0.06 M HF. This procedure ensures that the final Ti cut is free of any residual matrix. It should be noted that matrix-free or -poor samples, such as chemical reference materials (OL-Ti, Col-Ti) or mineral separates, require higher initial acid concentrations, 1.75 M HCl - 2 Vol.-% H_2O_2 instead of 1 M. With little to no matrix elements to adsorb to the resin, Ti is retained longer in the resin (AG50W X8). As such, it is required to either rinse the columns longer (using a larger volume of acid -

> 30 mL) or to increase acid strength of the sample solution. After the first column, the acid remains at 1 M HCl — 2 Vol.-% H₂O₂.

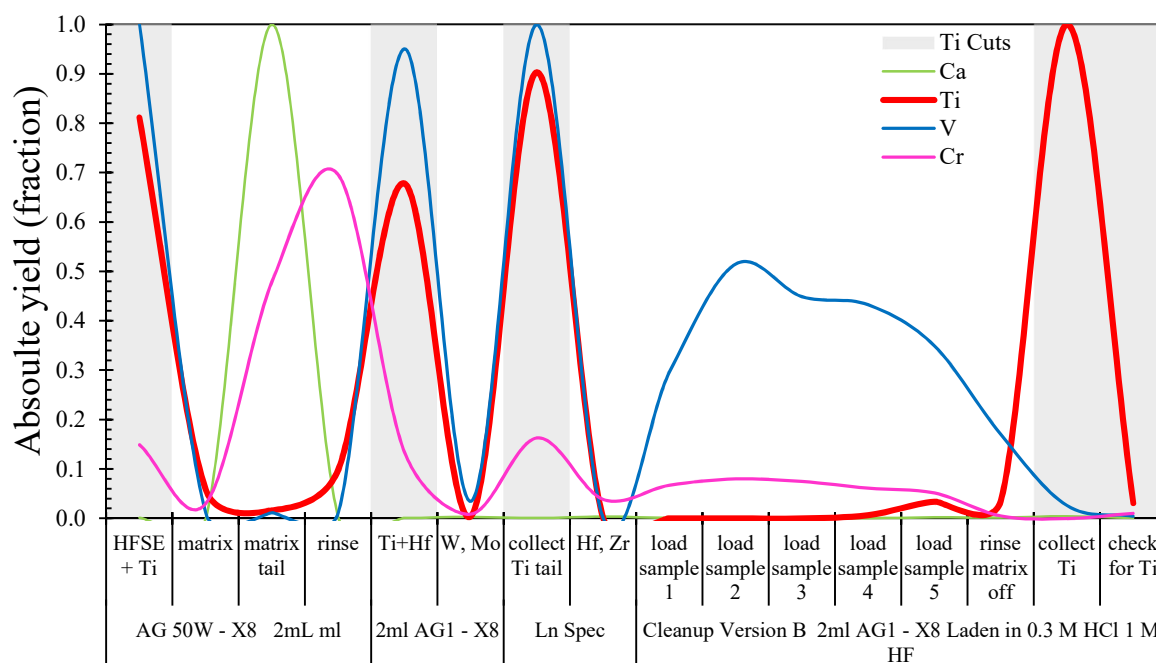


Figure 2-2: Complete elution curve for chemistry and clean-up. Clean-up step can be repeated if necessary.

2.1.2 Final Ti separation scheme

The final recipe and yield test (Figure 2-3 a and b) now technically allows quantitative separation of Ti from the matrix. For this, samples are weighed in such that ideally 30 μg of Ti are present. Sample powders are placed into a Savillex beaker and spiked (see section 2.2.1). The sample is then digested using a 4 mL of concentrated HNO₃ and HF (ratio 3:1). After equilibration in the closed Savillex beaker for 48 hours on a hotplate at 120 °C, the dissolved sample is subsequently dried down and refluxed in 6 M HNO₃ with a trace of 0.5 M HCl – 0.5 HF. This step is carried out to prevent the formation of secondary fluorides and to transfer the sample in chloride form. The sample is refluxed with 6 M HCl – 0.06 M HF and after it is dried, it is taken up in 1 mL of 1 M HCl – 2 Vol.-% H₂O₂. The added hydrogen peroxide complexes with Ti, which gives the (Ti) sample solution a light yellow-orange colour, in addition to the yellow colour from Fe in the matrix and the added HCl. The sample is then loaded onto the column and directly eluted with other HFSE as the matrix is adsorbed onto the AG-50W-X8 cation resin. Matrix elements are then eluted with 10 mL of 6 M HCl. The Ti & HFSE cut is

then loaded onto the next column (AG1 X8 anion resin), and Ti, Zr, Hf are directly eluted whereas W, Mo are subsequently eluted in 10 mL of a 6 M HNO₃ – 0.5 M HF – 2 Vol.-% H₂O₂ mixture.

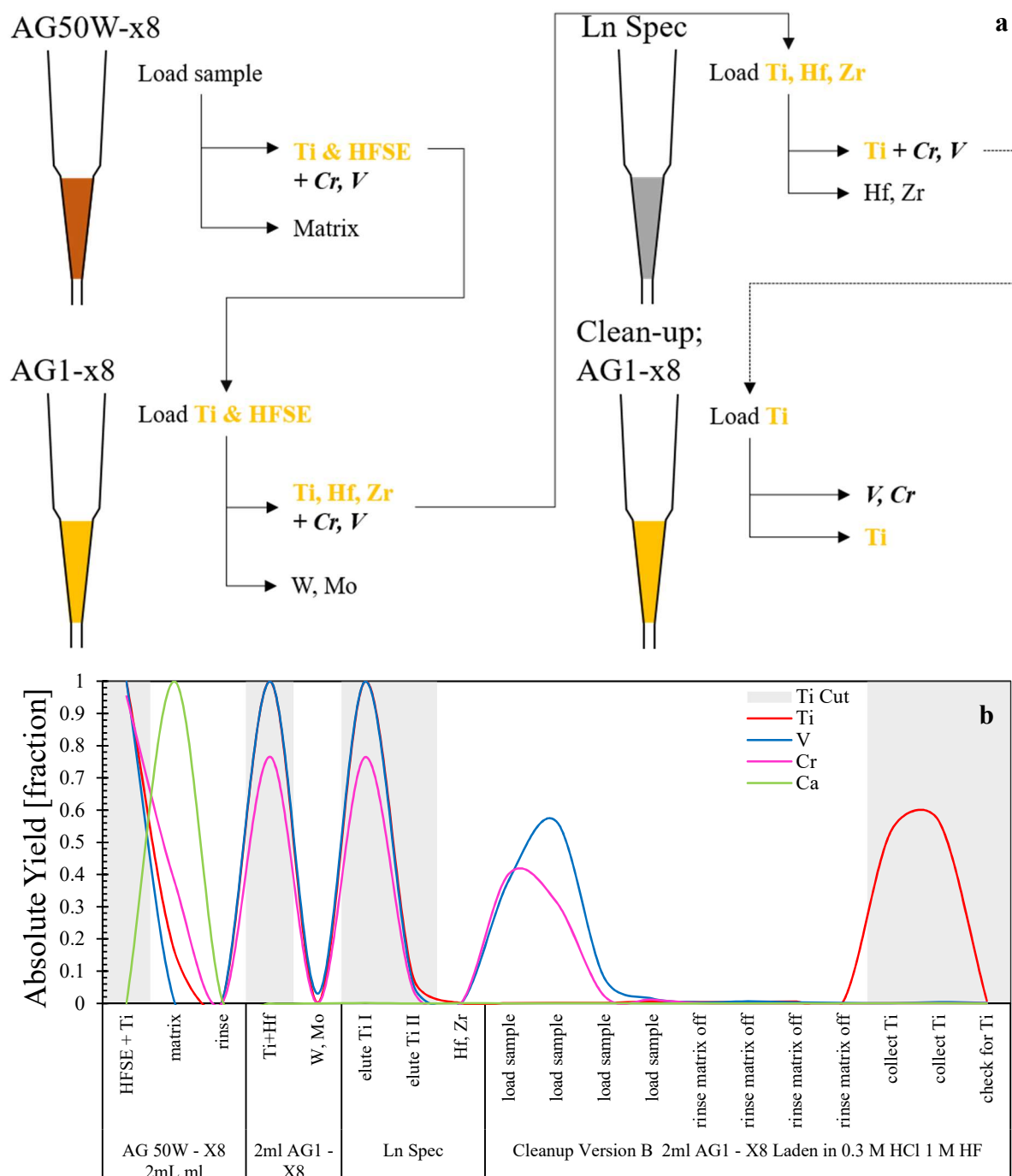


Figure 2-3 a and b: a) Schematic chemical separation and b) yield test results. Each arrow in a) represent a different element cut. Yields were calculated using an Excel macro initially written by Peter Sprung. The clean-up can be repeated if necessary to assure absolute purity

The sample is then loaded into an LN Spec Column filed with 2 mL resin volume. The Ln Spec resin elutes Ti and retains Hf and Zr. At this stage, trace amounts of Ca and significant amounts of Cr and V are still present in the sample solution. For the required clean-up, the sample solution is adjusted from 1 M HCl – 2 Vol.-% H₂O₂ to a 1 M HF – 0.33 M HCl. This increases the sample volume to around 100 mL. Because of the larger sample volume, the AG1-X8 cation columns are pre-cleaned and fitted with 120 mL Biorad funnels, which enables the sample to be loaded in a single step. With 1 M HF – 0.33 M HCl, Ti adsorbs onto the resin, eluting remaining trace amounts of Ca, Cr and V already in the loading step. Separation should be achieved at this stage, however, occasionally trace amounts of Cr and V may still be present in the sample solution, prompting the incorporation of a second clean-up step. In this case, after loading 100 mL of sample, Ti is washed down using 10 mL of 1 M HCl 2 vol.-% H₂O₂ and is again adjusted to 1 M HF – 0.33 M HCl. As such, the clean-up can be repeated one last time and complete Ti purification can be achieved. The samples are then ready to be measured on the multi-collector ICP-MS.

2.2 Double Spike Isotope Dilution

The aim of a double spike is to provide a solution for the following equation:

$$R_{Sample}^{i/j} = \left[p \cdot R_{Spike}^{i/j} + (1 - p)R_{Ref.-Mat}^{i/j} \cdot \left(\frac{m_i}{m_j} \right)^\alpha \cdot \left(1 + \frac{\varepsilon_{Sample}^{i/j}}{10^4} \right) \right] \cdot \left(\frac{m_i}{m_j} \right)^\beta \quad 2-1$$

where R is the ratio of isotopes i and j in the sample, spike and reference material. The amount of spike is given by p , m is the atomic mass of i and j , whereas α and β correspond to the natural and instrumental mass bias factors, respectively. The term included in ε accounts for mass-independent variations, but can be neglected for Ti in terrestrial and lunar samples (Deng *et al.*, 2018b; Greber *et al.*, 2017b). It is evident that with the three unknowns p , α and β , three equations to solve this system are required, thus the need for at least four isotopes, *i.e.*, three isotope ratios for double spike study. It should be pointed out though that in recent studies a

three isotope implementation of a double-spike procedure has been used successfully (Coath *et al.*, 2017; Millet and Dauphas, 2014).

2.2.1 Spike and Reference Material calibration

Nicolas Greber generously provided an aliquot of the Origins Lab Ti reference material, henceforth named OL-Ti. This well-known material was calibrated in a study by Millet & Dauphas (2014) and is now the accepted reference material in mass-dependent and independent Ti isotope studies (Deng *et al.*, 2018a, 2018b, 2019; Gerber *et al.*, 2017; Greber *et al.*, 2017a, 2017b; Millet *et al.*, 2016).

Furthermore, an Alfa Aesar PURATRONIC high-purity Ti rod was procured (99.999%; LOT. Nr M04C023) to calibrate an in-house reference material similar to the Origins Lab Ti reference material (OL-Ti; Millet *et al.*, 2016; Millet and Dauphas, 2014). The rod was sliced using a diamond string saw and four chips were picked for dissolution into individual stock solutions with varying final Ti concentrations (henceforth called “Col-Ti”). Two high purity ^{47}Ti and ^{49}Ti oxide powders were obtained from the Oak Ridge National Laboratory. Single spikes and metal chips were weighed in pre-cleaned 250 mL (spikes) and 500 mL (Col-Ti) perfluoroalkoxy alkane (PFA) bottles and dissolved in a 1:19 mixture of concentrated HF and 3 M HNO_3 . Titanium spikes were mixed in a 500 mL PFA bottle that had been pre-cleaned with diluted acids over multiple days (diluted HCl, HF, HNO_3 and a HNO_3 -HCl mixture) in order to obtain a double spike composition with $^{49}\text{Ti}/^{47}\text{Ti}$ of 1.07207. This optimal value was calculated with the double spike toolbox by Rudge *et al.*, (2009). The double spike has a final Ti concentration of $410.9 \pm 0.3 \mu\text{g/g}$.

Calibration of the double spike was initially performed using an aliquot of OL-Ti, as its isotope composition is well constrained (Millet *et al.*, 2016; Millet and Dauphas, 2014). In order to determine the isotope composition of the double spike, two solutions were prepared: an ideally spiked (sample to spike proportions of 0.51:0.49) aliquot of OL-Ti (1 $\mu\text{g/mL}$ total Ti) and a pure dilution of the double spike (1 $\mu\text{g/mL}$, pure double spike Ti). Subsequent measurements of the diluted, pure double spike yield average, but not mass-bias-corrected, isotope ratios. Nevertheless, these values should fall on a mass-dependent fractionation line with DS-OL-Ti mixture on a three isotope plot. Using the exponential law, the non-mass-bias-corrected double spike ratios of pure double spike measurements (described above) are then artificially (*i.e.*, mathematically) fractionated. The corrected ratios are used in the double spike deconvolution

of the doped OL-Ti aliquots. Since the reference material relative to itself is defined as $\delta(^{49}\text{Ti}/^{47}\text{Ti})_{\text{OL-Ti}} = 0 \text{ ‰}$, the fractionation factor is iteratively adjusted so that the known, average isotope composition of the OL-Ti becomes equal to 0 ‰ (Kurzweil *et al.*, 2018). The isotope compositions of the double spike and-in house reference material correspond to $\delta^{49}\text{Ti}$ of 430 and 0.204 δ -units, respectively. The results are given in Table 2-1.

Table 2-1: Calibration results for Col-Ti and the Cologne Ti double spike. Higher uncertainty for $^{46}\text{Ti}/^{47}\text{Ti}$ and $^{48}\text{Ti}/^{47}\text{Ti}$ stem from the lower abundance of these isotopes in the double spike solution. Atomic masses from (Wang *et al.*, 2017).

	$^{46}\text{Ti}/^{47}\text{Ti}$	$^{48}\text{Ti}/^{47}\text{Ti}$	$^{49}\text{Ti}/^{47}\text{Ti}$
OL-Ti	1.092874	10.070565	0.749766
2se	0.000011	0.000086	-
Millet <i>et al.</i> (2016) - Double spike	0.032663	0.270783	0.945969
2se	0.000001	0.000007	0.000013
Cologne double spike	0.006224	0.07996	1.072000
2se	0.000018	0.00015	0.000065
Cologne ColTi Ref.-mat	1.092759	10.071601	0.749919
2se	0.000002	0.000019	0.000003
[c] DS, Ti_{tot}	410.9 \pm 0.3 $\mu\text{g/g}$		
[c] ^{49}Ti	4.170 \pm 0.003 $\mu\text{mol/g}$		
[c] ^{47}Ti	4.055 \pm 0.003 $\mu\text{mol/g}$		

In order to verify and better constrain the ideal sample/spike proportion that was calculated using the double spike toolbox of Rudge *et al.*, (2009), a set of spiked chemical and terrestrial reference materials were prepared. Aliquots with the equivalent of 30 μg sample Ti of the in-house reference material (36 μL of an 820 $\mu\text{g/mL}$ solution) were prepared and added double spike to achieve sample:spike proportions of 0.9:0.1, 0.8:0.2, 0.7:0.3, 0.6:0.4, 0.55:0.45, 0.51:0.49 (ideal ratio) 0.45:0.55, 0.4:0.6, 0.3:0.7, and 0.2:0.8, respectively (see Table 2-2). Furthermore, eight separate digestions of the reference material BCR-2 (3 mg powder; 30 μg Ti) were spiked in the sample:spike proportions of 0.9:0.1, 0.8:0.2, 0.7:0.2, 0.51:0.49 (ideal ratio), 0.5:0.5, 0.43:0.57, 0.28:0.72, and 0.18:0.82. Lastly, five aliquots of the OL-Ti solution (30 μg Ti), were spiked in the sample:spike proportions of 0.8:0.2, 0.55:0.45, 0.51:0.49 (ideal ratio), 0.45:0.55, and 0.2:0.8. Chemical reference materials were equilibrated in closed vessels over 72 hours and then diluted for measurement on the MC-ICP-MS. In the case of BCR-2, Ti was separated according to the chemical separation procedure described in 2.1.2. The results of the over- and under spiking tests are shown in Figure 2-4 and Table 2-2 and indicate that for sample:spike proportions between 0.36:0.64 and 0.74:0.26 (a $^{48}\text{Ti}/^{47}\text{Ti}_{\text{Mix}}$ between ~ 1 and ~ 3) $\delta^{49}\text{Ti}$ is accurate.

Table 2-2: Results of reference materials with varying sample to spike ratios (given as the fraction of sample in the sample-spike mixture - f_{sample}). Each sample was measured three times and bracketed by ideally spiked Col-Ti and OL-Ti for additional quality control.

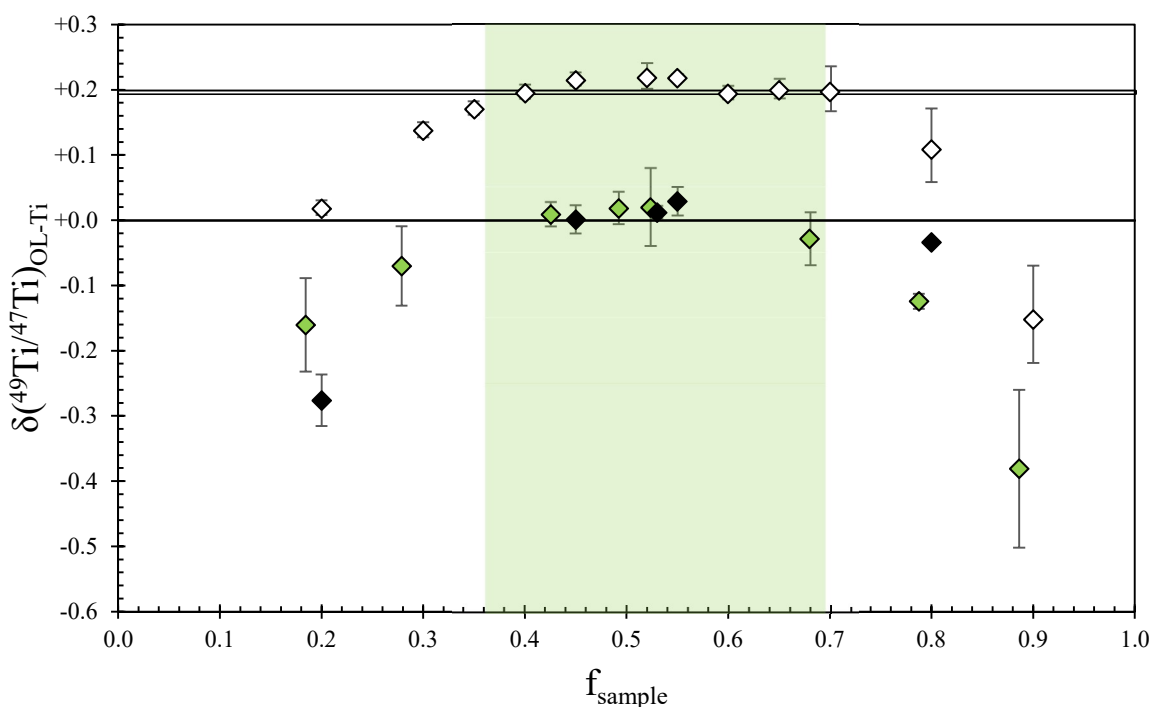
Reference Material	f_{sample}	$^{48}\text{Ti}/^{47}\text{Ti}_{\text{mix,measured}}$	2 s	$\delta(^{49}\text{Ti}/^{47}\text{Ti})_{\text{OL-Ti}}$	2 s	n	95% c.i.
Col-Ti	0.90	6.2661	0.0011	-0.152	0.067	3	0.083
Col-Ti	0.80	4.16766	0.00022	0.109	0.050	3	0.063
Col-Ti	0.70	2.94295	0.00011	0.197	0.031	3	0.038
Col-Ti	0.65	2.52532	0.00021	0.194	0.013	3	0.016
Col-Ti	0.60	2.20163	0.00013	0.194	0.009	3	0.011
Col-Ti	0.55	1.78385	0.00011	0.2182	0.0043	3	0.0053
Col-Ti	0.52	1.6142	0.0078	0.218	0.017	3	0.022
Col-Ti	0.45	1.293016	0.000049	0.215	0.009	3	0.011
Col-Ti	0.40	1.097546	0.000034	0.195	0.010	3	0.012
Col-Ti	0.35	0.881946	0.000011	0.170	0.009	3	0.011
Col-Ti	0.30	0.751503	0.000064	0.138	0.010	3	0.013
Col-Ti	0.20	0.480887	0.000010	0.018	0.010	3	0.012
OL-Ti	0.80	3.57164	0.00039	-0.0339	0.0031	3	0.0038
OL-Ti	0.55	1.483742	0.000094	0.029	0.022	3	0.027
OL-Ti	0.53	1.284446	0.000024	0.012	0.010	3	0.012
OL-Ti	0.45	1.049865	0.000037	0.001	0.022	3	0.027
OL-Ti	0.20	0.397393	0.000027	-0.276	0.039	3	0.049
BCR-2	0.89	5.9691	0.0015	-0.38	0.12	3	0.150
BCR-2	0.79	4.14241	0.00020	-0.124	0.011	3	0.014
BCR-2	0.68	2.87956	0.00019	-0.029	0.041	3	0.050
BCR-2	0.52	1.76271	0.00002	0.020	0.060	3	0.074
BCR-2	0.49	1.53541	0.00005	0.018	0.025	3	0.031
BCR-2	0.43	1.258582	0.000033	0.009	0.019	3	0.023
BCR-2	0.28	0.729415	0.000081	-0.070	0.061	3	0.076
BCR-2	0.18	0.40141	0.00015	-0.160	0.072	3	0.089
Session averages							
Session I							
ColTi				0.199	0.039	28	0.008
OL-Ti				0.000	0.018	8	0.008
Session II							
ColTi				0.193	0.047	26	0.010
OL-Ti				0.000	0.012	8	0.005
BCR-2 ideal range							
				0.005	0.045	4	0.017
Total averages							
Col-Ti				0.196	0.043	54	0.006
OL-Ti				0.000	0.015	16	0.004

Samples with sample:spike proportions outside this range should be excluded, as delta values drift towards lower values.

Table 2-3 Amount of Ca, $^{44}\text{Ca}/^{47}\text{Ti}$ and resulting $\delta^{49}\text{Ti}$ of Ca-doped Col-Ti solutions.

ng/ μL Ca	$^{44}\text{Ca}/^{47}\text{Ti}_{\text{measured}}$	2 s	$\delta^{49}\text{Ti}/^{47}\text{Ti}_{\text{OL-Ti}}$	2 s	n	95% c.i.
1	0.0004325	0.0000047	0.219	0.057	3	0.071
10	0.0011534	0.0000010	0.243	0.038	3	0.047
100	0.010093	0.000025	0.265	0.044	3	0.054
500	0.049157	0.000058	0.437	0.023	3	0.029
1000	0.098285	0.000099	0.616	0.030	3	0.037

The isotopes ^{46}Ca and ^{48}Ca interfere with ^{46}Ti and ^{48}Ti , both of which are part of the double spike deconvolution. Accordingly, it is important that the analyte solution is Ca-free, which is usually achieved using the chemical separation procedure described in section 2.1. Nevertheless, the effect of Ca contamination in the final measurement solution was tested by doping five aliquots (1 $\mu\text{g}/\text{mL}$ Ti) of the spiked Col-Ti solution with an Alfa Aesar Ca plasma standard, resulting in concentrations of 1, 10, 100, 500 and 1000 ng/mL Ca.



The green field represents the range in which spiked samples reproduce the published values. BCR-2 range average is $\delta^{49}\text{Ti}/^{47}\text{Ti}_{\text{OL-Ti}} = +0.005 \pm 0.017\text{‰}$ ($n = 12$ values of four samples with three measurements each).

- \diamond ColTi
- \blacklozenge BCR-2
- \blacklozenge OITi
- ColTi average
- OL-Ti average

Figure 2-4 a and b: $\delta^{49/47}\text{Ti}_{\text{OL-Ti}}$ versus f_{sample} i.e. the fraction of the sample in the sample - spike mixture. The diagram illustrates the range in which the sample/spike ratio reproduces published values. The threshold for precise and accurate results is approximately between approximately 0.36 and 0.7 (f_{sample}). Millet et al., (2016) give their BCR-2 at $\delta^{49}\text{Ti}/^{47}\text{Ti}_{\text{OL-Ti}} = -0.015 \pm 0.005\text{‰}$ 95% c.i. which overlaps generously with the results from this study.

Interferences of Ca isotopes can be accurately corrected up to Ca concentrations of 100 ng/ μ L or a $^{44}\text{Ca}/^{47}\text{Ti}$ of 0.01 (Figure 2-4 a, b) without a significant decrease in the measurement precision of Ti isotope ratios. Larger abundancies of Ca cause erroneous, positive $\delta^{49}\text{Ti}$ values.

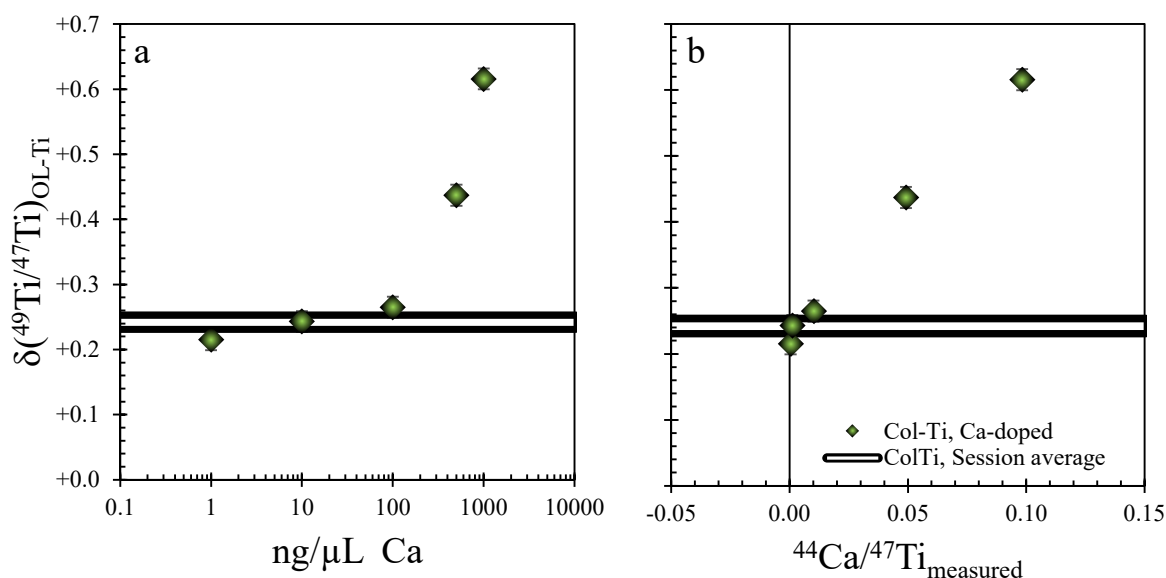


Figure 2-5 a and b: Determined $\delta^{49}\text{Ti}$ Ca-doped 1 $\mu\text{g}/\text{mL}$ Ti Col-Ti solutions versus a) Ca concentration and b) $^{44}\text{Ca}/^{47}\text{Ti}$ ratio. Samples reproduce accurately up until Ca concentrations of 100 ng/ μ L or 100 ppb Ca. See also Table 2-3

2.2.2 Data reduction

Rudge *et al.*, (2009) published with their “double spike toolbox” a reliable and adaptable data reduction template for double spike studies. However, this script requires *MatLab* or similar programs. Creech and Paul (2015) made the code for their *IsoSpike* software available, however, this code is an add-on for the (now commercial) *iolite* data-processing software. Siebert *et al.*, (2001) and Compston and Oversby (1969) have published an offline applet that can be incorporated into Excel. As data reduction can be done iteratively, statistical evaluation is iterative as well (Heuser *et al.*, 2002; Schoenberg *et al.*, 2008). An alternate approach, which is to perform Monte Carlo simulations for uncertainty estimates is available but was not used in this study.

2.2.2.1 The Siebert *et al.*, (2001) method

The double-spike deconvolution method used in this study relies on a vector-based approach to iteratively approach the unknowns of the double spike equation. First, the natural and instrumental fractionation factors are determined by

$$R_{measured} = R_{true} \left(\frac{m_i}{m_j} \right)^{F_{inst}} \quad \text{and} \quad R_{measured} = R_{true} \left(\frac{m_i}{m_j} \right)^{F_{nat}} \quad 2-2$$

These first values for F_{inst} and F_{nat} are chosen, arbitrarily, from experience. The ratio used for correction ($^{49}\text{Ti}/^{47}\text{Ti}$) is denoted as x , whereas $^{48}\text{Ti}/^{47}\text{Ti}$ and $^{46}\text{Ti}/^{47}\text{Ti}$ be y and z . With these three ratios, one can define the coordinates for $R_{x,y,zSA}$ and $R_{x,y,zST}$

$$R_{x,y,zSA} = R_{x,y,zST} \cdot \left(\frac{m^{49,48,46}\text{Ti}}{m^{47}\text{Ti}} \right)^{F_{nat,ass}} \quad 2-3$$

Step 1

The points ST , SA and SP create a plane, SA is initially an artificially fractionated sample that is used as a starting point (assume a value for $F_{nat,ass}$ at first and fractionate ST). Based on the equations for a plane $z = ax + by + c$ the parameters a, b and c are written as:

$$\begin{aligned} a &= \frac{R_y ST (R_z SA - R_z SP) + R_y SA (R_z SP - R_z ST) + R_y SP (R_z ST - R_z SA)}{R_y ST (R_x SA - R_x SP) + R_y SA (R_x SP - R_x ST) + R_y SP (R_x ST - R_x SA)} \\ b &= \frac{R_x ST (R_z SA - R_z SP) + R_x SA (R_z SP - R_z ST) + R_x SP (R_z ST - R_z SA)}{R_x ST (R_y SA - R_y SP) + R_x SA (R_y SP - R_y ST) + R_x SP (R_y ST - R_y SA)} \\ c &= R_z ST - a \cdot R_x ST - b \cdot R_y ST \end{aligned} \quad 2-4$$

Step 2

Assuming a value for $F_{inst,ass}$, the true mixed ratios are calculated by

$$\frac{R_{x,y,zMS}}{\left(\frac{M^{46,48,49}\text{Ti}}{M^{47}\text{Ti}} \right)^{F_{inst,ass}}} = R_{x,y,zMT} \quad 2-5$$

These true values form a mass-dependent fractionation line. If the values for both F_{inst} and F_{nat} are true, the line $MS-MT$ pierces the plane from Step 1 on the same point as the exponential fractionation curve. As such, two equations describe these lines with $z = dx + e$ and $z = fy + g$ and the parameters d , e , f , and g are given by

$$d = \frac{R_z MS - R_z MT}{R_x MS - R_x MT} ; e = R_z MS - d \cdot R_x MS$$

$$f = \frac{R_z MS - R_z MT}{R_y MS - R_y MT} ; g = R_z MS - f \cdot R_y MS \quad 2-6$$

Using these, it is possible to calculate the intersect of the lines with the planes $ST-SA-SP$ with

$$x_{int} = \frac{b \cdot g - b \cdot e + e \cdot f - c \cdot f}{a \cdot f + b \cdot d - d \cdot f}$$

$$y_{int} = \frac{a \cdot e - a \cdot g + d \cdot g - c \cdot d}{a \cdot f + b \cdot d - d \cdot f}$$

$$z_{int} = a \cdot x_{int} + b \cdot y_{int} + c \quad 2-7$$

These intersect values are the new values for $R_{x,y,z}MT$ and are used to calculate an instrumental mass bias factor with

$$F_{inst,calc} = \frac{\ln(R_x MS/R_x MT)}{\ln(M_{49}/M_{47})} \quad 2-8$$

With this new value, the process goes back to equation 2-4 to recalculate $R_{x,y,z}MT$, ending in a recalculated $F_{inst,calc}$, and is repeated once more (*i.e.*, two iterations).

Step 3

If correct, the point defined by $R_{x,y,z}MT$ lies on a mixing line between the sample SA and the spike SP . This can however only be true if the assumed value for $F_{nat,ass}$ is correct. Similar to the calculations in step 1 (using ST , SA and SP), the points MS , MT and SP form a plane. As such, one calculates the parameters a , b and c using:

$$a = \frac{R_y MS(R_z MT - R_z SP) + R_y MT(R_z SP - R_z MS) + R_y SP(R_z MS - R_z MT)}{R_y MS(R_x SAMTR_x SP) + R_y MT(R_x SP - R_x MS) + R_y SP(R_x MS - R_x MT)}$$

$$b = \frac{R_x MS(R_z MT - R_z SP) + R_x MT(R_z SP - R_z MS) + R_x SP(R_z MS - R_z MT)}{R_x MS(R_y MT - R_y SP) + R_x MT(R_y SP - R_y MS) + R_x SP(R_y MS - R_y MT)}$$

$$c = R_z MS - a \cdot R_x MS - b \cdot R_y MS \quad 2-9$$

Once again, the two lines are defined by

$$d = \frac{R_z SA - R_z ST}{R_x SA - R_x ST} ; e = R_z SA - d \cdot R_x SA$$

$$f = \frac{R_z SA - R_z ST}{R_y SA - R_y ST} ; g = R_z SA - f \cdot R_y SA \quad 2-10$$

and their intersect with the plane $MS-MT-SP$ is given by the following expressions:

$$x_{int} = \frac{b \cdot g - b \cdot e + e \cdot f - c \cdot f}{a \cdot f + b \cdot d - d \cdot f}$$

$$y_{int} = \frac{a \cdot e - a \cdot g + d \cdot g - c \cdot d}{a \cdot f + b \cdot d - d \cdot f}$$

$$z_{int} = a \cdot x_{int} + b \cdot y_{int} + c \quad 2-11$$

Using the $R_{x,y,z}SA_{new}$, $F_{nat,new}$ is calculated and the process is repeated from *Step 1* onwards. These iterations are then repeated at least three times until the deviation of the new value from the previous one is deemed acceptable. The values usually converge after two to three iterations.

2.2.2.2 The Compston and Oversby (1969) method

The original study by Compston and Oversby (1969) described an iterative approach using equations previously published for Sr isotope studies. Their approach uses different ratios than the usually used ${}^i\text{Ti}/{}^{47}\text{Ti}$ in order to de-magnify the uncertainties. For Ti and using their definition:

$$R_{mix}^{i/^{49}\text{Ti}} = (Z_{sample}^i + Z_{spike}^i) / (Z_{sample}^{^{49}\text{Ti}} + Z_{spike}^{^{49}\text{Ti}}) \quad 2-12$$

With $Z_{sample,spike}^i$ as the abundance of a given Ti isotope ⁱ. Equation 2-12 can be re-arranged to

$$Q_{^{49}\text{Ti}} = Z_{sample}^{^{49}\text{Ti}} / Z_{spike}^{^{49}\text{Ti}} = (R_{mix}^i - R_{spike}^i) / (R_{sample}^i - R_{mix}^i) \quad 2-13$$

and

$$R_{mix}^{^{48}\text{Ti}/^{49}\text{Ti}} = (R_{spike}^{^{48}\text{Ti}/^{49}\text{Ti}} + Q_{^{46}\text{Ti}/^{49}\text{Ti}} R_{sample}^{^{48}\text{Ti}/^{49}\text{Ti}}) / (1 + Q_{^{46}\text{Ti}/^{49}\text{Ti}}) \quad 2-14$$

This calculated mixed ratio is then used to constrain a first instrumental mass bias using the exponential law. This mass bias factor is used to calculate both $^{46}\text{Ti}/^{49}\text{Ti}$ and $^{48}\text{Ti}/^{49}\text{Ti}$ which are then used to calculate the $^{48}\text{Ti}/^{46}\text{Ti}$:

$$R_{calc,mix}^{^{48}\text{Ti}/^{46}\text{Ti}} = \left[R_{mix}^{^{48}\text{Ti}/^{49}\text{Ti}} \cdot \left(\frac{m_{^{48}\text{Ti}}}{m_{^{49}\text{Ti}}} \right)^\beta \right] \cdot \left[R_{mix}^{^{46}\text{Ti}/^{49}\text{Ti}} \cdot \left(\frac{m_{^{46}\text{Ti}}}{m_{^{49}\text{Ti}}} \right)^\beta \right] \quad 2-15$$

In similar fashion to the two previous equations, 2-13 can be transformed to

$$Q_{^{46}\text{Ti}} = Z_{sample}^{^{46}\text{Ti}} / Z_{spike}^{^{46}\text{Ti}} = Q_{^{49}\text{Ti}} R_{sample}^{^{46}\text{Ti}/^{49}\text{Ti}} / R_{spike}^{^{46}\text{Ti}/^{49}\text{Ti}} \quad 2-16$$

which can be used to calculate the $^{48}\text{Ti}/^{46}\text{Ti}$ of the sample with

$$R_{sample}^{^{48}\text{Ti}/^{46}\text{Ti}} = \left(1 + \frac{1}{Q_{^{46}\text{Ti}}} \right) \cdot R_{mix}^{^{48}\text{Ti}/^{46}\text{Ti}} - \frac{1}{Q_{^{46}\text{Ti}}} \cdot R_{spike}^{^{48}\text{Ti}/^{46}\text{Ti}} \quad 2-17$$

Equation 2-5 can be calculated using the corrected $R_{calc,mix}^{^{48}\text{Ti}/^{46}\text{Ti}}$ and the constant $R_{spike}^{^{48}\text{Ti}/^{46}\text{Ti}}$. The “true” isotope ratios are initially used to calculate the natural fractionation factor α , which in turn are used again to calculate the Q -proxy (using the now corrected $^{46}\text{Ti}/^{49}\text{Ti}$ and $^{48}\text{T}/^{49}\text{Ti}$).

The average Q_{49Ti} is used to calculate the $R_{mix}^{48Ti/49Ti}$ in 2-12, the circular references in the spreadsheet iteratively converge towards the true values of the isotopic ratios (Q -proxy in 2-12 and α , respectively).

2.2.2.3 Choice of data reduction scheme

Both data reduction schemes were tested using a set of chemical and terrestrial standards as well as processed lunar samples. After evaluating both methods, the data reduction scheme by Schoenberg *et al.*, (2008) based on Compston and Oversby (1969; henceforth Compston-scheme) is chosen. Both data sheets yield identical results for reference materials. However, due to higher precision after six measurements for spiked lunar samples in the Compston-scheme, results can be significantly different (Figure 2-6).

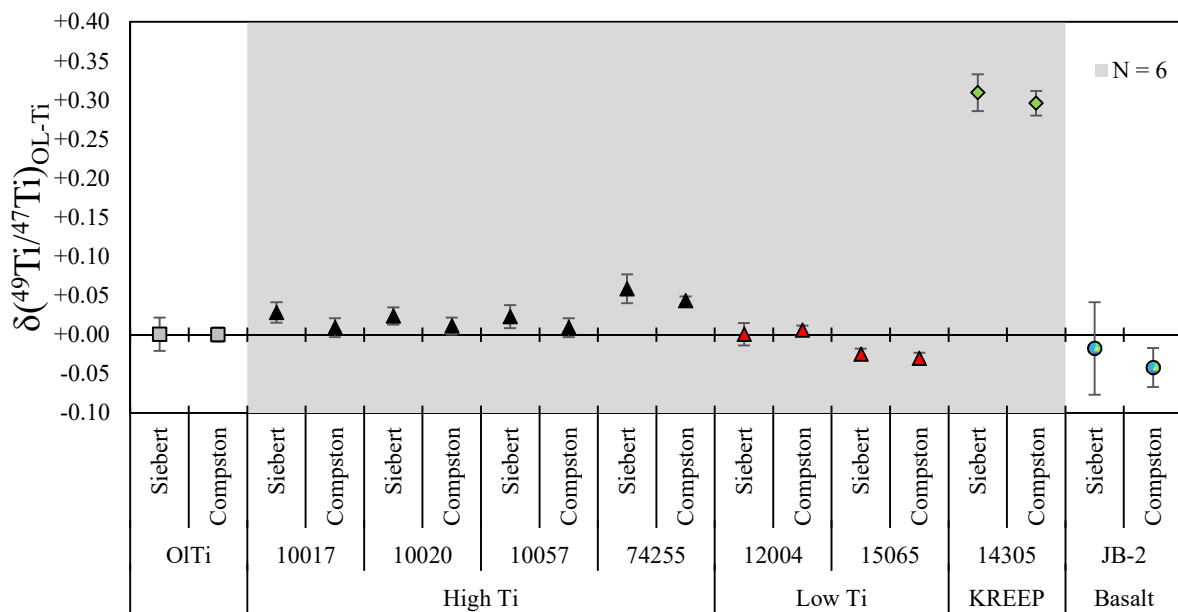


Figure 2-6: Comparison between Siebert *et al.*, (2001) and Compston and Oversby (1969). The larger uncertainty and discrepancy in results for some samples (such as 74255) is a quirk of the statistical treatment and the iteration performed. OL-Ti and BCR-2 have been measured more than 12 times.

Even if this may be a quirk of the statistical treatment of each cycle, given that references materials are also more precise with this method, the decision to adopt the Compston-scheme was made, aiming at better long-term reproducibility. Even if the final spreadsheet is working

with circular references, making it vulnerable to Excel errors, it proves easier to handle and keeps data file size within a reasonable range of ± 3 Mb.

2.2.2.4 Neutron capture correction

As described in section 2.2, the double spike equation (2-1) contains a component that takes into account secondary neutron capture effects:

$$\left(1 + \frac{\varepsilon_{Sample}^{i/j}}{10^4}\right) \quad 2-18$$

$=$ *mass-independent effect*

The quantification of the mass-independent effect, the ε -value, needs to be determined separately on a spike-free aliquot using the standard sample bracketing technique. Once this effect is known, it can be used to accurately calculate the $^{49}\text{Ti}/^{47}\text{Ti}$ of the sample. However, this is only necessary when working with meteorite samples, as the effects in lunar samples and terrestrial samples are either small or absent, respectively (Deng *et al.*, 2018b; Greber *et al.*, 2017b). See sub-section 3.2.1 for a discussion of neutron capture effects in analysed lunar samples.

2.3 MC-ICP-MS

All measurements were performed on the Thermo Scientific Neptune Plus MC-ICP-MS and results are given relative to the OL-Ti reference material. The instrument was operated in high resolution mode to clearly identify the peak shoulders of the Ti isotopes. This is required as non-resolvable, polyatomic interferences, such as $^{28}\text{Si}^{19}\text{F}$ or $^{14}\text{N}^{16}\text{O}_2^1\text{H}^+$ are potentially introduced into the system via the analyte solution (0.045 M HNO_3 – 0.005 M HF), resulting in an interference on ^{47}Ti (May and Wiedmeyer, 2008). The “peak shoulders” determine a mass range on the respective mass, that is interference-free, as polyatomic interferences tend to be heavier than the respective mass. As such, by performing mass scans one can identify the isotope, isotope + interference and interference region and adjust the cup configuration accordingly. An ESI APEX HF sample introduction system was used, as more interferences are expected when using the CETAC Aridus II, probably due to the membrane fitted in the Aridus.

In this study, two cup configurations were used (see Figure 2-8). The first one, labelled IC for isotope compositions was developed in light of nucleosynthetic studies. The nucleosynthetic effects are the largest on ^{50}Ti , ^{49}Ti and ^{47}Ti are used for mass bias correction. Due to their Ca-interferences and limitations of the instruments in simultaneously recording all masses from ^{44}Ca to ^{52}Cr , ^{46}Ti and ^{48}Ti and are usually excluded from nucleosynthetic studies (Gerber *et al.*, 2017; Trinquier *et al.*, 2009; Zhang *et al.*, 2012).

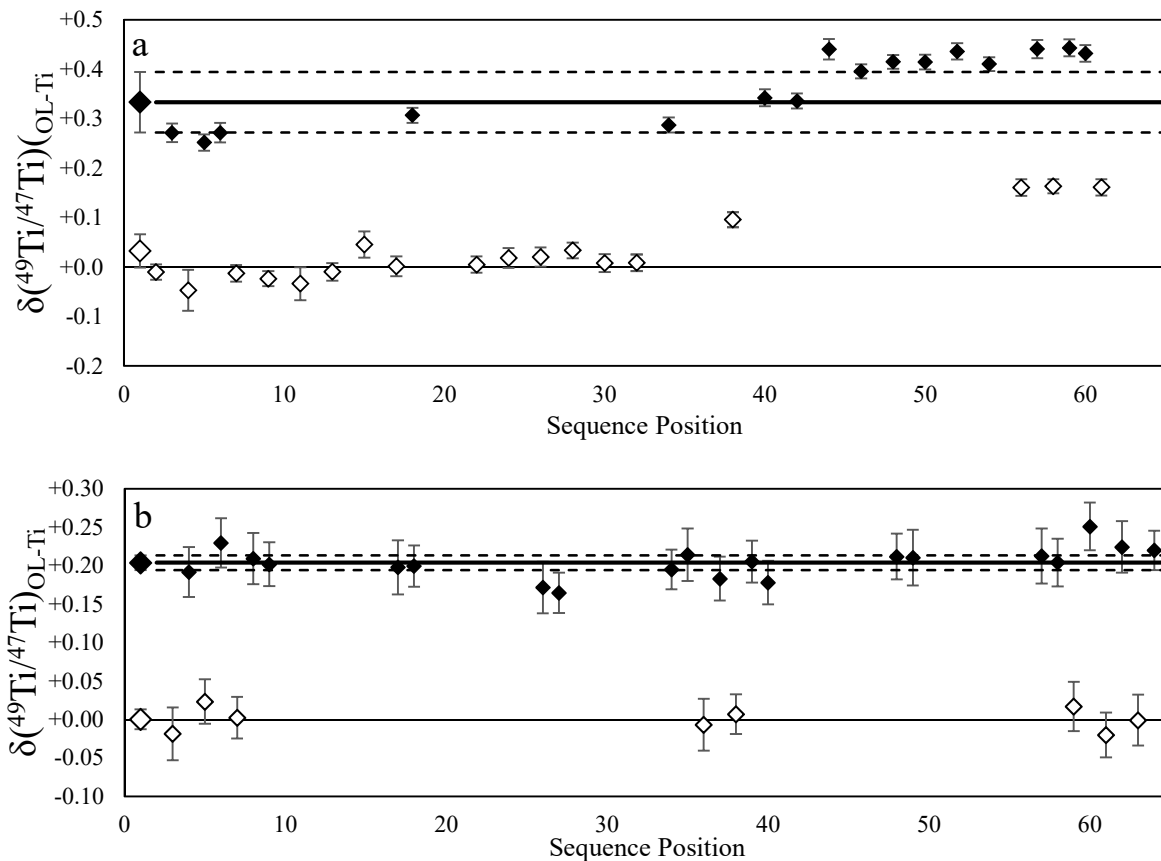


Figure 2-7: Drift of ^{49}Ti with time when using X-cone (a) and normal cone (b). While the relative difference may stay the same between OL-Ti (hollow symbols) and Col-Ti (black diamonds), the sequence would need to be split up in different parts which would each separately have to be adjusted to $\delta^{49}\text{Ti}$ (OL-Ti) = 0, decreasing the accuracy of the method. Dashed black lines give the 95 % c.i. all ColTi analysis of the sequence. The last has been omitted from the Col-Ti_{average}, which would lie at $0.4 \pm 0.1\%$

As such, only Cr and V need to be monitored closely. The second cup configuration (ID) was set up as part of the double spike study, as in this case ^{50}Ti is not used in the double spike deconvolution and interferences on ^{50}Ti can be neglected. However, as ^{46}Ti and ^{48}Ti are here part of the double spike deconvolution, interference correction for trace amounts of Ca are required and ^{44}Ca is monitored. Intermediate precision (long term reproducibility) of the all Ti isotope dilution measurement sequences is given in Figure 2.9. The lunar sequences included

terrestrial reference materials JB-2 and BCR-2, the terrestrial sequence BHVO-2, BCR-2 and occasionally JB-2. During the latter measurements aliquots of JB-2 and BHVO-2 have been mistaken for BCR-2, resulting in erroneous results.

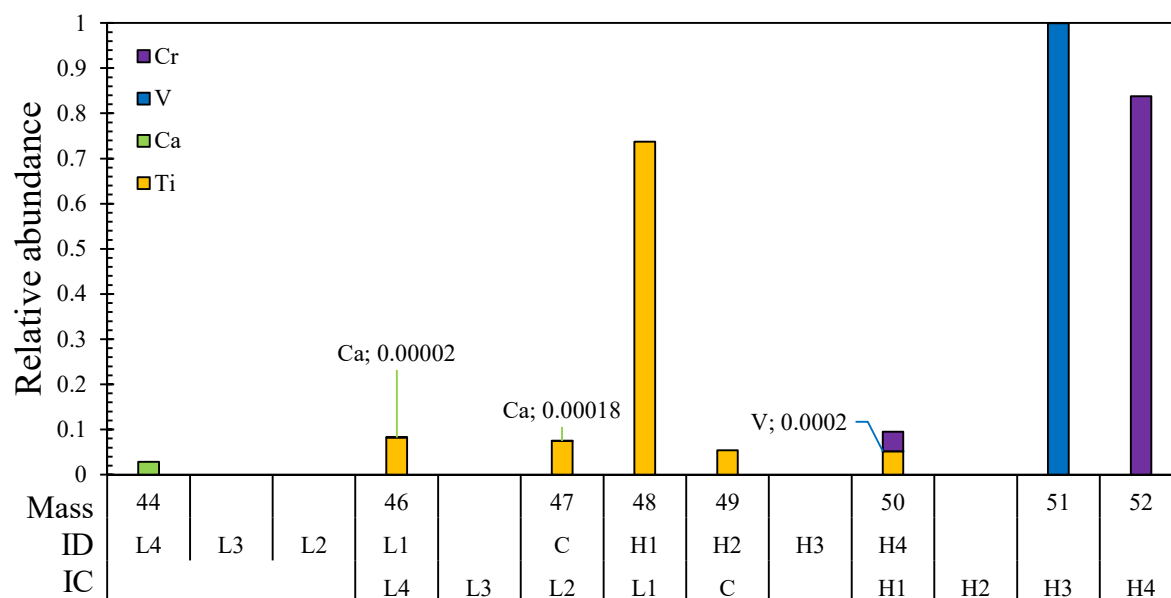


Figure 2-8: Cup configuration of IC- and ID set up. L4-L1, C and H1-H4 denote the respective faraday cups (L = light, C = centre, H = heavy). In case of Ca and V interferences, the contribution is very small and as such additionally given as decimal fraction.

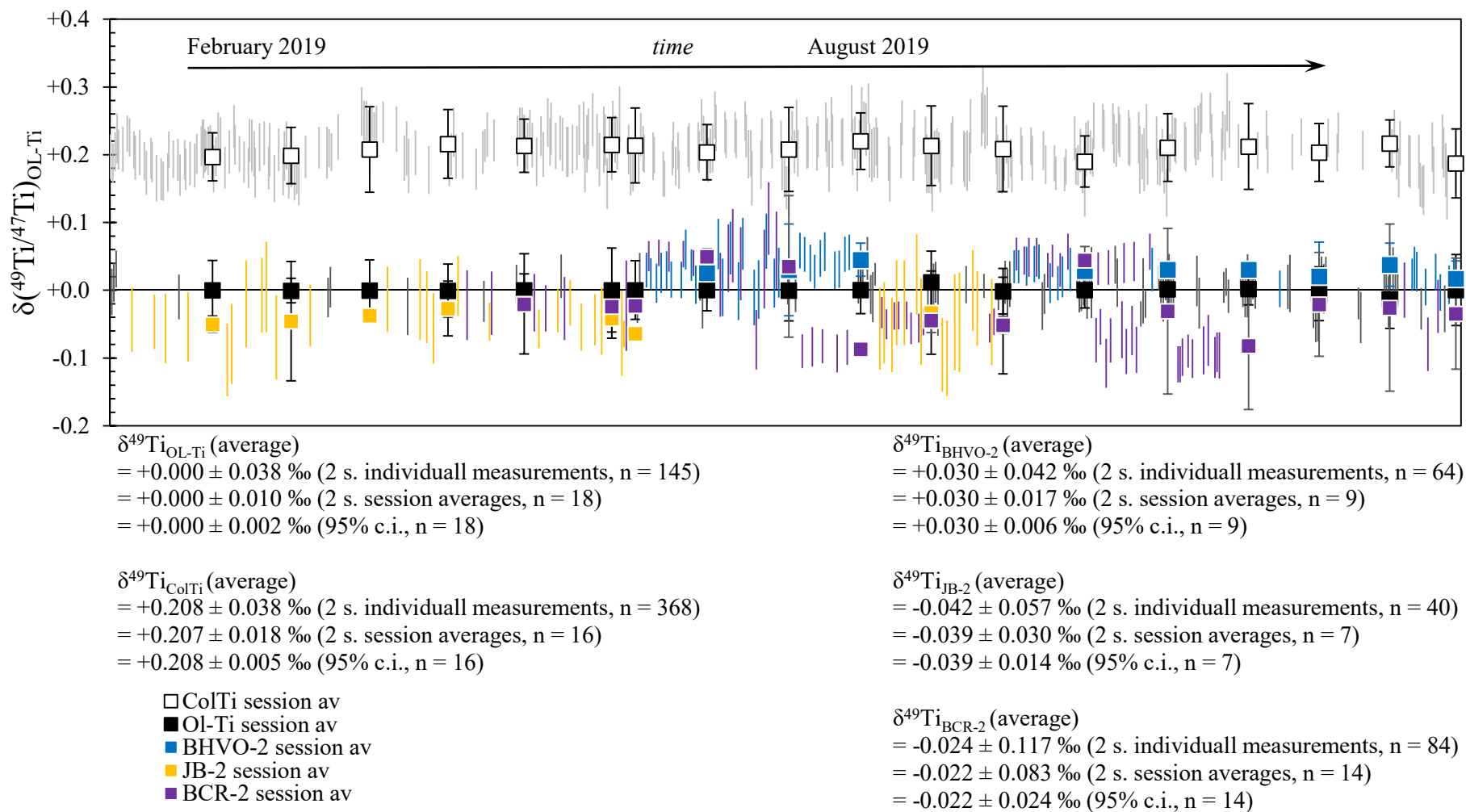


Figure 2-9: Long term precision and accuracy of the Ti method. Each coloured bar represents a sample measurement; the symbols give the sequence average. Detailed information about precision is given in the figure.

CHAPTER 3

UNRAVELLING LUNAR MANTLE

PROCESSES THROUGH THE TI ISOTOPE

COMPOSITION OF LUNAR BASALTS

3.1 Introduction

3.1.1 Formation of the Moon

3.1.1.1 The Giant Impact hypothesis

It is now widely accepted that the Earth-Moon system formed as a result of an impact or series of impact events between the proto-Earth and one or more planetesimals (Canup, 2014; Reufer *et al.*, 2012; Rufu *et al.*, 2017)). The exact number of impact(s), impact angle and composition of the impactors is still subject of much debate (Asphaug, 2014; Rufu *et al.*, 2017). Some models, however, found that the mass of the impactor(s) may contribute up to 80% of its mass into the accretion disc from which the Moon eventually formed. This is somewhat problematic given the similarities of Earth in Moon with respect to their isotopic characteristics, namely when considering refractory stable isotope systems - *e.g.*, oxygen ($^{17}\text{O}/^{16}\text{O}$ and $^{18}\text{O}/^{16}\text{O}$ within 12 ± 3 ppm; Herwartz *et al.*, 2014; Wiechert, 2001), iron (Sossi and Moynier, 2017: $\delta^{57}\text{Fe}_{\text{Mg-suite}} = \delta^{57}\text{Fe}_{\text{Earth mantle}}$), titanium ($^{50}\text{Ti}/^{47}\text{Ti}$ within ± 4 ppm; Zhang *et al.*, 2012), vanadium (no resolvable difference between $\delta^{51}\text{V}$ of lunar and terrestrial basalts after neutron capture correction of the former; Hopkins *et al.*, 2019), or silicon ($\delta^{30}\text{Si}_{\text{Moon,average}} = \delta^{30}\text{Si}_{\text{BSE}}$; Armytage *et al.*, 2012 and references therein).

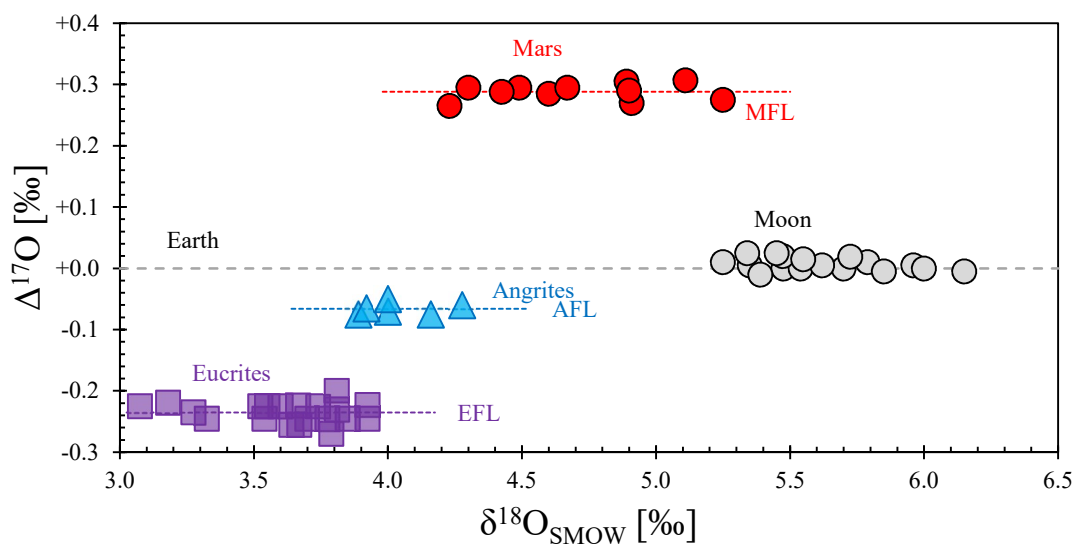


Figure 3-1: Departure from the terrestrial fractionation line expressed as $\Delta^{17}\text{O}$. Moon and Earth are identical, whereas other planetary bodies exhibit significant deviation from the TFL. Data modified from Asphaug (2014) and references therein. MFL, AFL and EFL describe the Mars, Angrite and Eucrite fractionation line, respectively

In contrast, most sampled bodies in the solar system (chondritic meteorites, achondrites and martian meteorites) show resolvable differences in various isotopic compositions (3-1). The isotopic similarities between Earth and Moon can be explained by chemical mixing during and after the lunar impact event, as both Earth and Moon are thought to have undergone a global magma ocean stage for an undetermined length of time (Gross and Joy, 2016). However, while the hot protoplanetary atmosphere may be sufficient to equilibrate oxygen isotopes, this is not sufficient for refractory Ti (Pahlevan and Stevenson, 2007; Zhang *et al.*, 2012). Rufu *et al.*, (2017) suggest that the Moon formed through a succession of smaller impacts, a so called multiple impact origin, which, according to their modelling, allows the formation of the Moon without violating compositional constraints or the angular momentum of the Earth-Moon system (Figure 3-2).

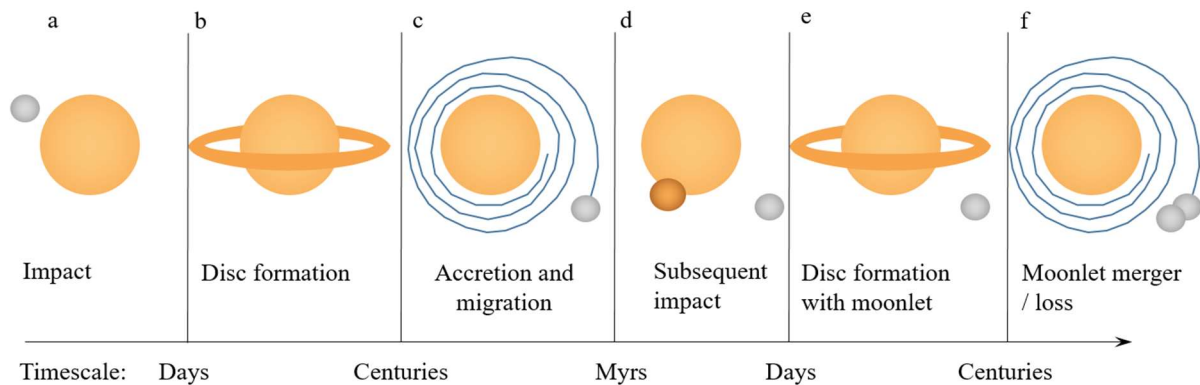


Figure 3-2: Multiple impact origin of the Moon. Moon-Mars sized impacts (a) form a debris disc (b) and tidal forces lead to outward migration of moonlets (c). Subsequent impact generates another disc and moonlet (d, e). With growing distance, tidal deceleration lets the moonlets their Hill radii and eventually merge or are lost (f). Figure modified from Rufu *et al.*, (2017).

The general consensus is that at least one impactor collided with the proto-Earth. The aftermath of this impact must have led to chemical homogenisation between the bulk silicate Earth and the Moon, as evidenced by homogeneity in refractory element isotope compositions such as Fe, Ti or Cr and less refractory elements such as oxygen (Sossi and Moynier, 2017; Trinquier *et al.*, 2009; Wiechert, 2001; Zhang *et al.*, 2012).

3.1.1.1 The Lunar Magma Ocean (LMO)

Trace element variations in different groups of lunar samples suggest that the Moon was at least partially molten, *i.e.*, covered by a Lunar Magma Ocean most likely due to the high energy of the lunar impact event (see Gross and Joy, 2016 and references therein; Warren and Wasson, 1979). The solidification of the LMO it thought to have occurred either in a single stage (fractional crystallization) or a two stage model (equilibrium crystallization in the early stage and then fractional crystallization, Figure 3-3 a; Gross and Joy, 2016). Mafic, Mg-rich olivine and orthopyroxene sank and formed mafic cumulates that make up the ambient lunar mantle, the residual magma became enriched in Fe and incompatible elements such as Ti (Figure 3-3 b). After 75% crystallization, anorthite crystallized at depths greater than 75 km (Gross and Joy, 2016 and references therein), and the higher buoyancy of this plagioclase-rich cumulate leads to its rise to the lunar surface (cf. Gross and Joy, 2016; Warren and Wasson, 1979). The crystallization and subsequent flotation of anorthosite lead to the formation of the lunar crust, which mitigated heat loss from the liquid remaining in the LMO (see Figure 3-3 c).

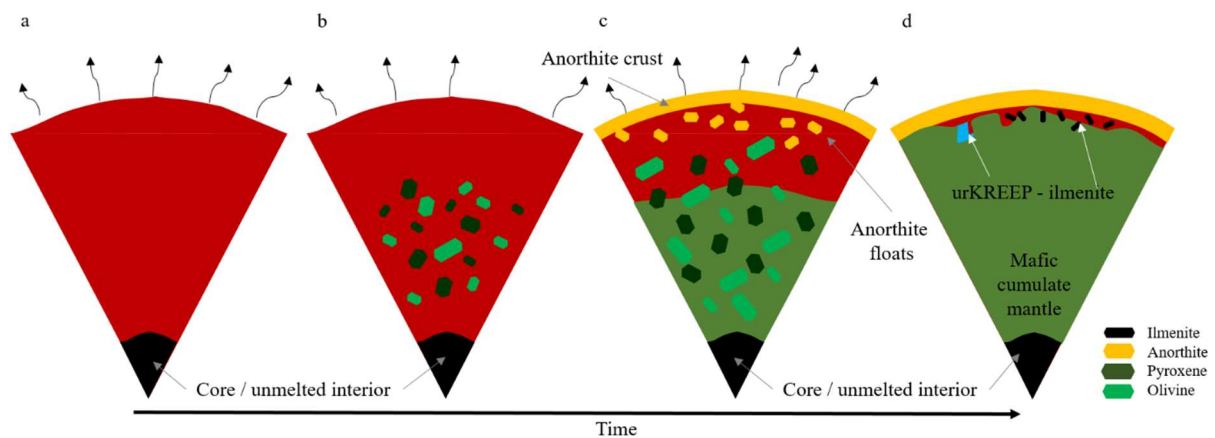


Figure 3-3: Formation model of the lunar crust, modified from Gross and Joy (2016 and references therein). Shown is differentiation (a) and crystallization (b) of the LMO. After 80% of LMO crystallization, the Anorthositic crust is formed (c). In the last figure (d), ilmenite crystallises and KREEP forms.

With ongoing fractional crystallisation of olivine and pyroxenes, which eventually formed the lunar cumulate mantle, the remaining melt then became increasingly Fe- and Ti-rich. Eventually, the contents of both FeO and TiO₂ of the melt became high enough that ilmenite saturation was reached, leading to abundant crystallisation of ilmenite (Figure 3-3 d Gross and Joy, 2016; Warren and Taylor, 2014; Warren and Wasson, 1979). Presumably, the last liquid

remaining in the LMO was highly enriched in incompatible elements like K, Rare Earth Elements, P (or KREEP), U and Th. Owing to its extremely high enrichment in incompatible trace elements compared to mare basalts and anorthosites (Figure 3-4), this so called KREEP component is easily traced in lunar extrusives, sampled during the Apollo missions, that may have assimilated KREEP cumulates on their way to the surface (Snyder *et al.*, 1992; Warren and Wasson, 1979). Models then suggest the presence of more buoyant Mg-rich lithologies under heavier, denser Fe-rich lithologies, the latter sitting closer to the surface than the former (Gross and Joy, 2016).

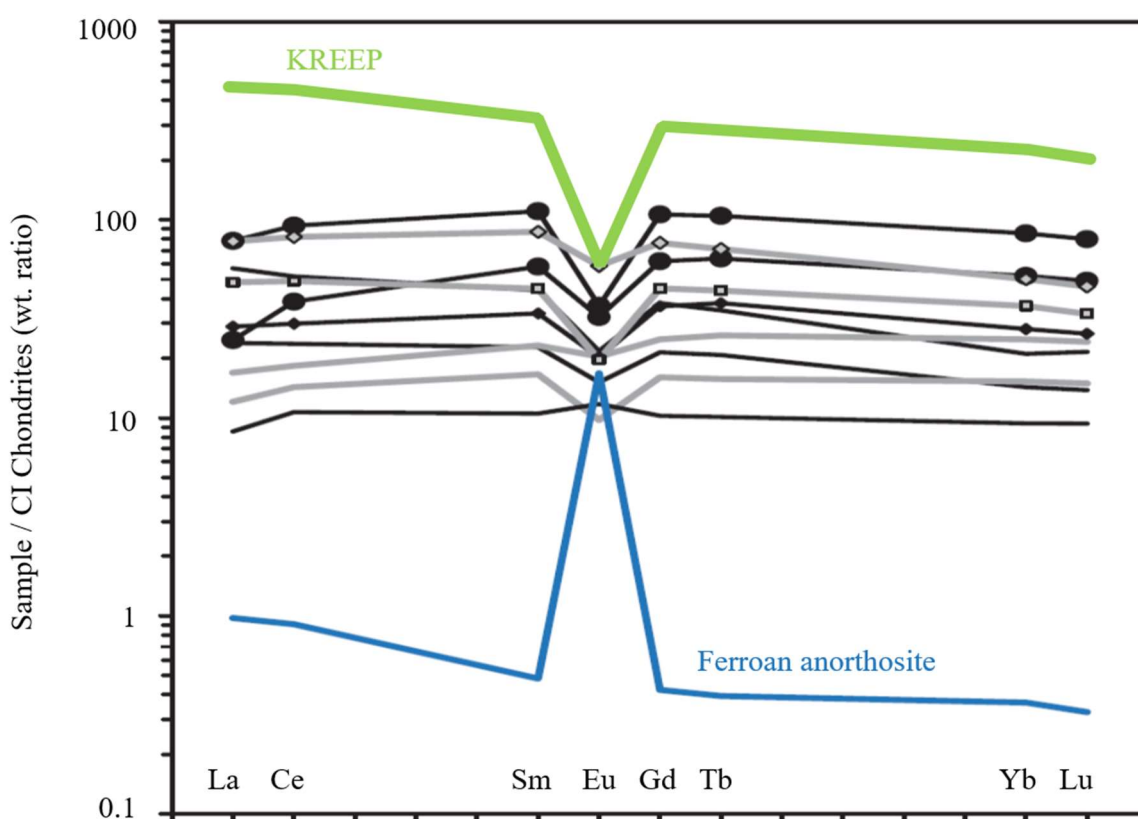


Figure 3-4: CI-Chondrite normalized REE element distribution of various lunar lithologies. Modified from Warren & Taylor (2014) and references therein.

This gravitational instability then is thought to have led to the denser ilmenite-bearing cumulates (IBC) inducing an overturn of the lunar mantle, with some arguing that these cumulates may have sunken as deep as the lunar core mantle boundary (Elkins Tanton *et al.*, 2002; Li *et al.*, 2019; Yu *et al.*, 2019; Zhao *et al.*, 2019). This mantle overturn most likely generated large volumes of magma and redistributed the IBC in the lunar mantle (Münker, 2010; Zhao *et al.*, 2019), which then intruded into the anorthositic crust. Up until ~ 3.8 Ga, the

Moon has been subjected to significant impact bombardment, as witnessed by its heavily cratered surface. The oldest lunar rocks date back 3.8 Ga and are thought to consist of partial melts of mafic lunar cumulates (Gross and Joy, 2016). Complementary rare earth element patterns and Eu/Eu* anomalies in KREEP-rich lithologies and ferroan anorthosites (Figure 3-4) suggest an identical source. However, this anomaly might have been produced by low pressure fractionation after effusion (Gross and Joy, 2016). The younger Mare basalts (between 3.9 and 3.1, possibly as young as 2.8 Ga; Hiesinger, 2006 and references therein), which are found filling older impact basins, can be grouped broadly into High-, Low-Ti, and very Low-Ti mare basalts, based on their TiO₂ content (Figure 3-5; Warren and Taylor, 2014). Various experimental studies were then performed in order to ascertain what petrogenetic processes were involved in the formation of these basalts (Longhi, 1992 and references therein).

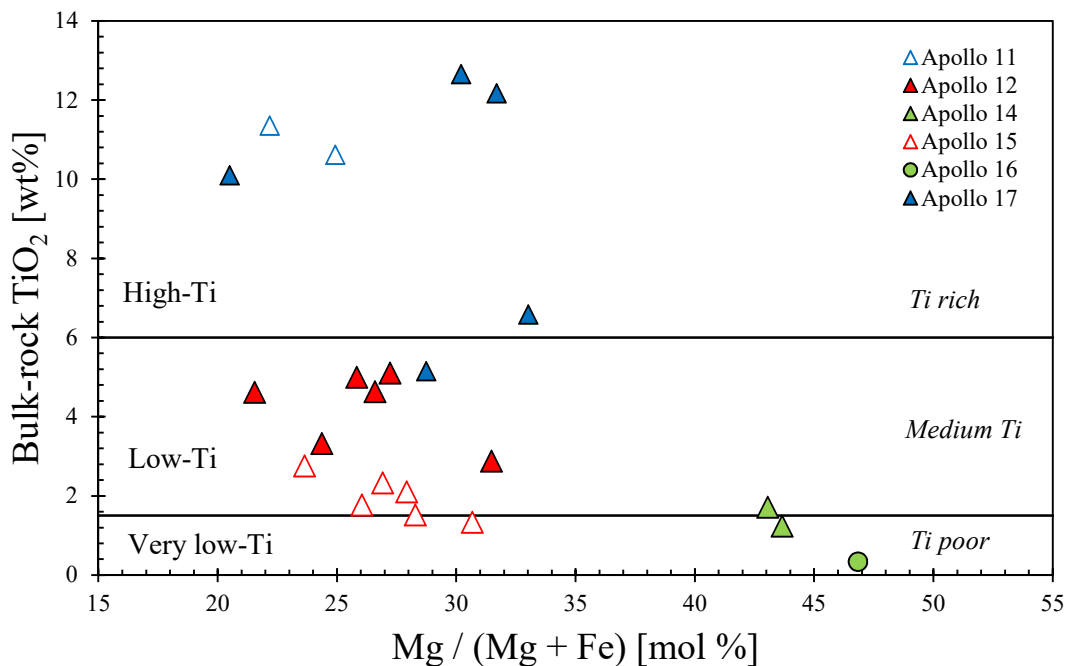


Figure 3-5: Classification of lunar rocks based on TiO₂ vs. Mg / (Mg + Fe). Criterion by Wood (1975) in solid black, modified from Warren and Taylor (2014) suggested a newer criterion (*italic*). Shown here are the samples used in this study with simplified symbols.

3.1.1.2 Experimental constraints on the petrogenesis of lunar samples

Longhi (1992) and Shearer (2006) give excellent literature overviews of experimental petrology research of lunar samples. In this section, I will briefly summarize findings relevant for the interpretation of the data. Walker *et al.*, (1977) argued that low-Ti olivine-normative-basalt

(ONB) 15555 formed as a result of melting from a -source region at around 170 km depth. Crystallisation experiments of a 15555-like composition shows that ilmenite does not appear along its liquid line of descent as a liquidus phase (Kesson, 1975). In absence of a Ti-bearing phase, no significant fractionation of Ti isotopes should take place (Millet *et al.*, 2016; assuming ilmenite or armalcolite are the only phases fractionating Ti isotopes), which is consistent with the results where $\delta^{49}\text{Ti}$ is the same as that of BSE within analytical uncertainty (*i.e.*, ca. 0 ‰). Low-Ti quartz-normative basalt (QNB) 15065 is thought to have originated from shallower regions of the lunar mantle of above 100 km (Walker *et al.*, 1977). At these depths, Kesson (1975 and references therein) suggested that low-Ti magmas assimilated a portion of an ilmenite-bearing cumulate (IBC) to form a high-Ti basalt. The bulk assimilation of IBC by a low-Ti magma would result in this magma inheriting the Ti isotopic composition of the IBC. The Ti isotopic composition of the IBC, depending on the timing IBC formation from the LMO, would range between -0.4 and -0.2 ‰ (very early crystallised ilmenite, depending on accuracy of ilmenite/melt fractionation factor of Johnson *et al.*, 2019 or; Millet *et al.*, 2016) or close to 0 ‰ (very late crystallised ilmenite). This means that if significant portions of an IBC were to be assimilated by a low-Ti magma, the resulting Ti isotope composition would either be negative or close to 0 ‰. Results from experiments carried out using compositions akin to low-Ti QNB 15065 also shows no evidence for fractional crystallisation of ilmenite, meaning the variations observed in the $\delta^{49}\text{Ti}$ of the QNB samples could be ascribed to source heterogeneity. Crystallisation experiments carried out using a composition from low-Ti ilmenite basalt 12022, show that ilmenite is, unsurprisingly, among the first phases appear on the liquidus (Green *et al.*, 1971), which would induce Ti isotope fractionation. Green *et al.*, (1975 and references therein) report that most Apollo 17 high-Ti basalts have around 10 % ilmenite as a liquidus phase, which can potentially indicate $\delta^{49}\text{Ti}$ fractionation in some high-Ti mare basalts due to ilmenite crystallisation. The source region of Apollo 11 and 17 high-Ti mare basalts is at an estimated depth of 250 km (Delano and Lindsley, 1982). Based on their high MgO/FeO, high K/Rb, and experimental results from these samples, Shih *et al.*, (1975 and references therein) assume that Apollo 11 and 17 high-Ti mare basalts evolved from a parent magma similar in composition to Apollo 17 sample 70017. The analysed suite of Apollo 11 and 17 basalts compositions is accurately reproduced by partial melting modelling. In detail, high-Ti mare basalts compositions of 75035, 74255 and 74275 are reproduced by Shih *et al.*, (1975) assuming batch melting of a mantle source with 90% cpx and 10 % ol+ilm (75035) and 70% cpx and 30% ol+ilm (74255, 74275). Based on this model Apollo 11 and 17 low-K high-Ti basalts (10020

and 75035) are the result of 20% batch melting, whereas Apollo 11 high-K basalts (10017 and 10057) result from around 1 % batch melting. Partial melting of ilmenite-bearing domains is expected to lead to more fractionated Ti isotope compositions in the melt (*i.e.*, higher $\delta^{49}\text{Ti}$), especially if ilmenite remains a residual phase throughout melting.

3.1.1.3 Summary

In the aftermath of the lunar Giant Impact and LMO crystallization, new volumes of magma were generated by the overturn of denser ilmenite bearing cumulates (Gross and Joy, 2016; Li et al., 2019; Yu et al., 2019; Zhao et al., 2019). Basaltic lunar samples analysed today now reflect various mixtures of these cumulates:

- KREEP-rich rocks represent the last residual liquid of LMO crystallisation, urKREEP
- Low-Ti mare basalts represent the ambient lunar mantle,
- High-Ti mare basalts reflect the ambient lunar mantle interacting with an ilmenite bearing domain.

The advantage in studying lunar mare basalts lies in the simplicity of the system, as the absence of mechanisms that allow crustal recycling (such as plate tectonics) and the continuous homogenization of the lunar mantle (convection) have been absent or limited throughout lunar history. Because of this, the Moon provides us with a snapshot of early planetary evolution to an extent that is not possible by solely studying terrestrial samples.

3.2 Titanium isotope systematics of lunar basalts

Experimental studies and the Hf and Nd isotope composition of mare basalts suggest that low-Ti mare basalts likely result from partial melting of lunar mafic cumulates, whereas high-Ti mare basalts are thought to reflect IBC involvement (*e.g.*, Longhi, 1992; Sprung *et al.*, 2013). However, whether high-Ti basalts result from IBC assimilation by mafic low-Ti magmas (Münker, 2010), or from the partial melting of a hybridized lunar mantle source (Snyder *et al.*,

1992), remains ambiguous. Titanium isotope variations in mare basalts may be used to discriminate between the two scenarios: Refractory, lithophile, and fluid-immobile Ti is predominantly tetravalent albeit lunar samples may contain significant amounts of Ti^{3+} (Leitzke *et al.*, 2018; Simon and Sutton, 2017). The principal Ti-bearing phase in the lunar mantle is ilmenite whose VI-fold coordinated crystal site preferentially incorporates lighter over heavier Ti isotopes (Schauble, 2004). The Ti isotope composition of terrestrial samples (given as $\delta(^{49}Ti/^{47}Ti)_{OL-Ti}$, relative to the Origins Lab reference material, henceforth $\delta^{49}Ti$; Millet and Dauphas, 2014) ranges between -0.046 and +1.8 ‰. Observed covariations between $\delta^{49}Ti$ and SiO_2 , TiO_2 , and FeO contents of terrestrial volcanic rocks suggest that stable Ti isotope variation is mainly driven by the onset of fractional crystallisation of Fe-Ti oxides during magmatic differentiation (Deng *et al.*, 2018a, 2019; Greber *et al.*, 2017b; Mandl *et al.*, 2018; Millet *et al.*, 2016). Consequently, the Ti isotope composition of lunar magmas might be a sensitive indicator to the crystallisation of the IBC, and its assimilation or partial melting: Millet *et al.*, (2016) reported $\delta^{49}Ti$ variations in three low-Ti mare basalts with a pooled $\delta^{49}Ti$ of -0.008 ± 0.019 ‰ and five high-Ti mare basalts with $\delta^{49}Ti$ between +0.011 and +0.033 ‰. The presence of more fractionated $\delta^{49}Ti$ in mare basalts, although suggested, has not yet been reported (Millet *et al.*, 2016). Indeed, for the urKREEP end-member, as represented by the lunar meteorite Sayh al Uhaymir (SaU) 169, a tentative $\delta^{49}Ti$ of $+0.330 \pm 0.034$ ‰ was obtained (Greber *et al.*, 2017b). In the following the $\delta^{49}Ti$ of 24 representative lunar samples is reported, in order to investigate their mantle sources in the context of three major end-members: the ambient lunar mantle (low-Ti), the late-stage cumulates (IBC, high-Ti), and the residual KREEP-rich component. Notably, the processes that affect $\delta^{49}Ti$ in lunar mantle cumulates and corresponding melts also fractionate high field strength element ratios (HFSE; Münker, 2010). High-precision HFSE, W, U, and Th data, obtained for the same samples (Thiemens *et al.*, 2019), can help to constrain $\delta^{49}Ti_{urKREEP}$, $\delta^{49}Ti_{IBC}$ and to identify the processes leading to $\delta^{49}Ti$ variations in lunar samples.

3.2.1 Neutron capture effects and potential sampling bias

Inasmuch as the Ti isotope analyses of lunar samples is concerned, secondary neutron capture effects due to the long-term exposure to cosmic rays can be an issue, and this possibility needs to be addressed (see also: Sprung *et al.*, 2013). Moreover, potential sampling bias due to small processed sample quantities may occur, which would lessen the representability of any reported

$\delta^{49}\text{Ti}$ values. What follows is a discussion of what has been done to investigate these issues and what steps, if any, were taken to mitigate them.

The effect of neutron capture on Ti isotopes using thermal neutron capture cross sections and epithermal resonance integrals was evaluated, calculated as described in Sprung *et al.*, (2010, 2013) and by using the JENDL 3.3 pointwise library at 300 K. Including these values and Ca/Ti, as well as Sc/Ti from Meyer (2012), into the neutron capture model of Sprung *et al.*, (2010, 2013) it becomes clear that the dominant process is the production of ^{49}Ti via neutron capture by ^{48}Ti .

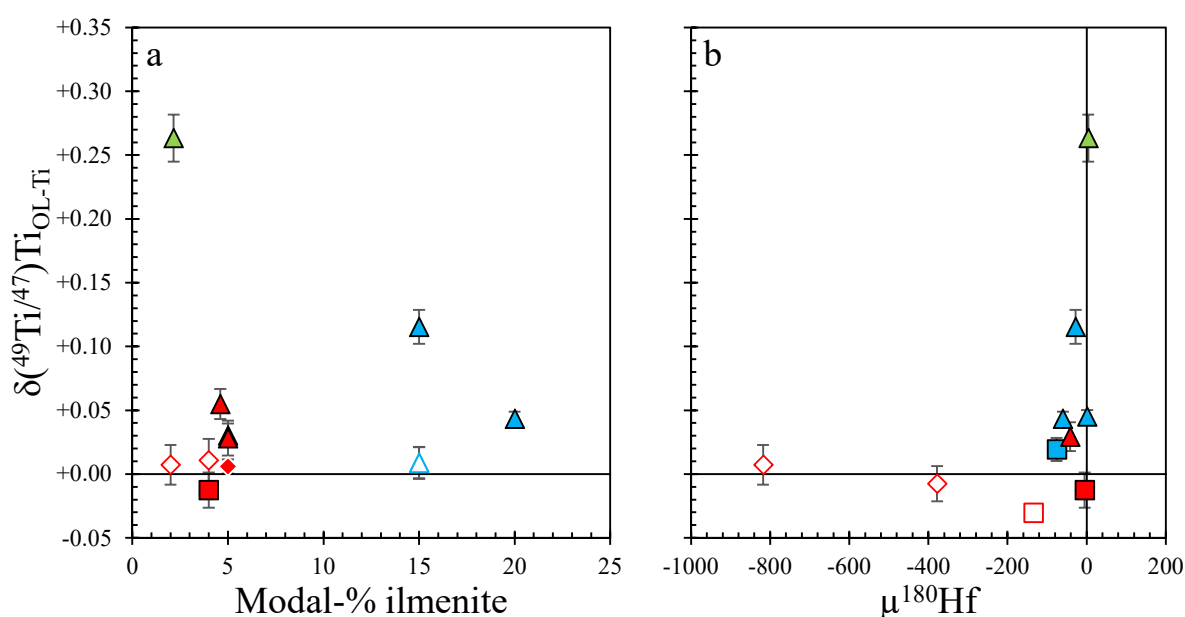


Figure 3-6 a and b: Sampling bias and neutron capture effects. a) Modal-% ilmenite vs. $\delta^{49}\text{Ti}$ plot shows no correlation of ilmenite content with $\delta^{49}\text{Ti}$. Symbols are the same as in Figure 3-7. b) Previous studies conclude secondary neutron capture effects to be negligible in Ti DS studies (Greber *et al.*, 2017b; Mandl *et al.*, 2018). Indeed, known proxy $\mu^{180}\text{Hf}$ shows no correlation with $\delta^{49}\text{Ti}$ (Data by Sprung *et al.*, 2013); Y-axis are identical in a and b.

Thus, the dominant effect of neutron capture on Ti isotope ratios referenced to ^{47}Ti is an increase of $^{49}\text{Ti}/^{47}\text{Ti}$, which is commonly used for mass bias correction. For samples that are strongly affected by neutron capture, the mass bias corrected ratios of ^{50}Ti , ^{48}Ti , and ^{46}Ti normalized to ^{47}Ti should display coupled anomalies. The magnitudes of such anomalies are expected to scale with the mass difference to ^{47}Ti because of erroneously addressing the neutron capture-induced shift in $^{49}\text{Ti}/^{47}\text{Ti}$ to mass bias. For example, neutron capture effects on Ti in lunar rocks have been reported primarily for ^{50}Ti (Gerber *et al.*, 2017; Trinquier *et al.*, 2009; Zhang *et al.*, 2012) whose mass differs the most from ^{47}Ti . From this evaluation, it is evident that the *true* neutron

capture-induced anomalies in $^{46}\text{Ti}/^{47}\text{Ti}$ and $^{48}\text{Ti}/^{47}\text{Ti}$, which are used in the double spike deconvolution (Greber *et al.*, 2017b) are at least one order magnitude lower than the (artificial) anomaly observed in $^{50}\text{Ti}/^{47}\text{Ti}$, while in $^{49}\text{Ti}/^{47}\text{Ti}$ they are ca. 1.5 times lower. Judging from the available data for lunar rocks (Gerber *et al.*, 2017; Trinquier *et al.*, 2009; Zhang *et al.*, 2012), no significant effects outside of the measurement reproducibility are expected, even for more strongly neutron-irradiated samples such as low-Ti mare basalt 15556 (Sprung *et al.*, 2013; See Figure 3-6). The lack of any observable correlation between $\delta^{49}\text{Ti}$ and $\mu^{180}\text{Hf}$, which is a known monitor for epithermal neutron, or with other proxies for prolonged cosmic-ray-exposure (exposure age data, Meyer, 2012 and references therein; as well as *e.g.*, $\varepsilon^{149}\text{Sm}$, Sprung *et al.*, 2013; See Figure 3-6 b) supports this conclusion. A similar assertion was reached for lunar samples using the Ti double spike method (Greber *et al.*, 2017b; Mandl *et al.*, 2018). Regarding sampling bias, sample weights in this study range from 3 to 10 mg and were taken from ~ 0.5 g powdered aliquots. The primary Ti phase in all relevant samples is ilmenite, whose crystallisation is thought to be the foremost process fractionating Ti isotopes (Millet *et al.*, 2016). The absence of any clear correlation between $\delta^{49}\text{Ti}$, SiO_2 , and TiO_2 content, or with the modal abundance of Fe-Ti oxides reported for each sample, indicates that the sample $\delta^{49}\text{Ti}$ is independent of ilmenite (and TiO_2) content (Figure 3-6 a). Consequently, sampling bias is unlikely to have affected the $\delta^{49}\text{Ti}$ results.

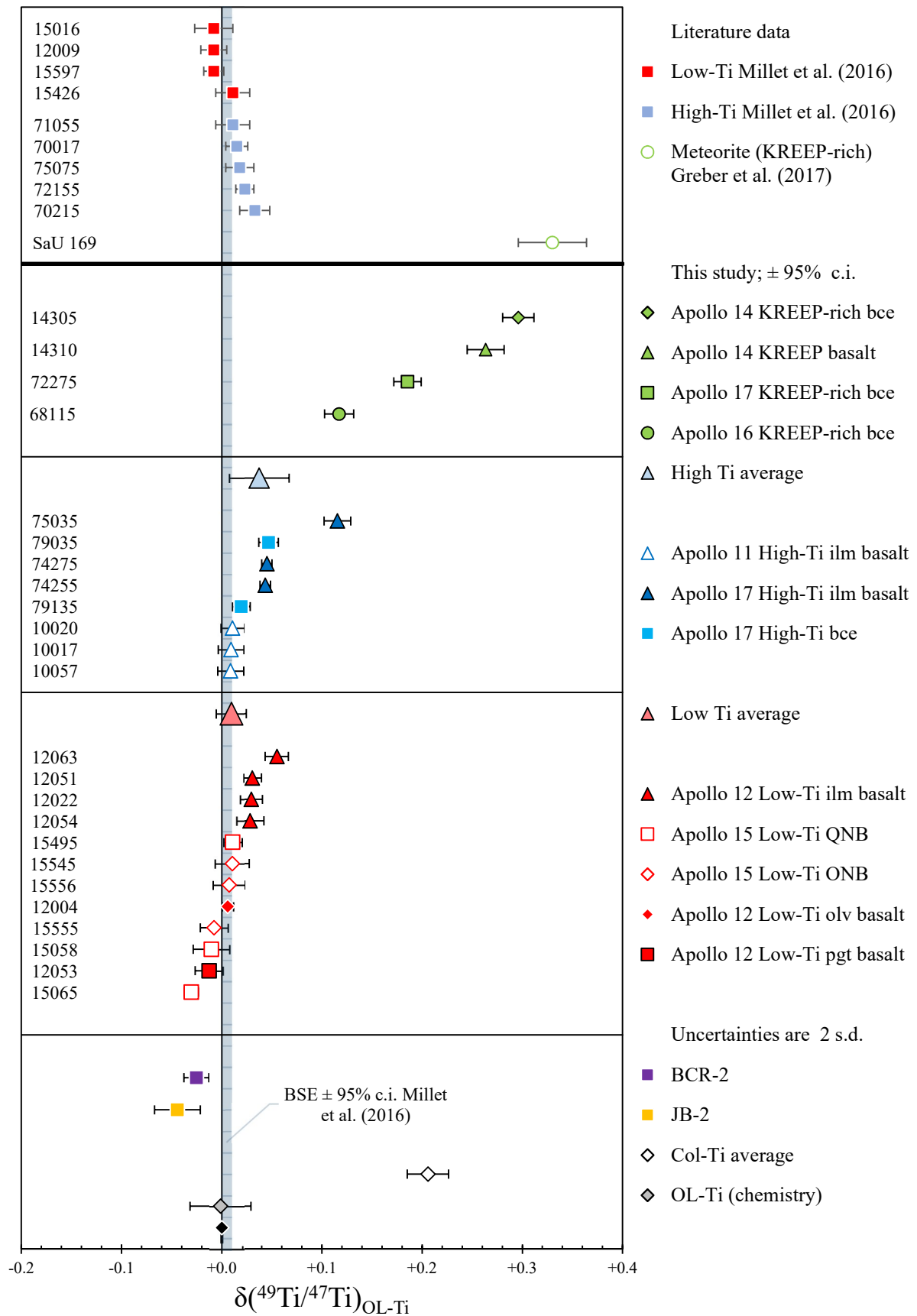
3.3 Results

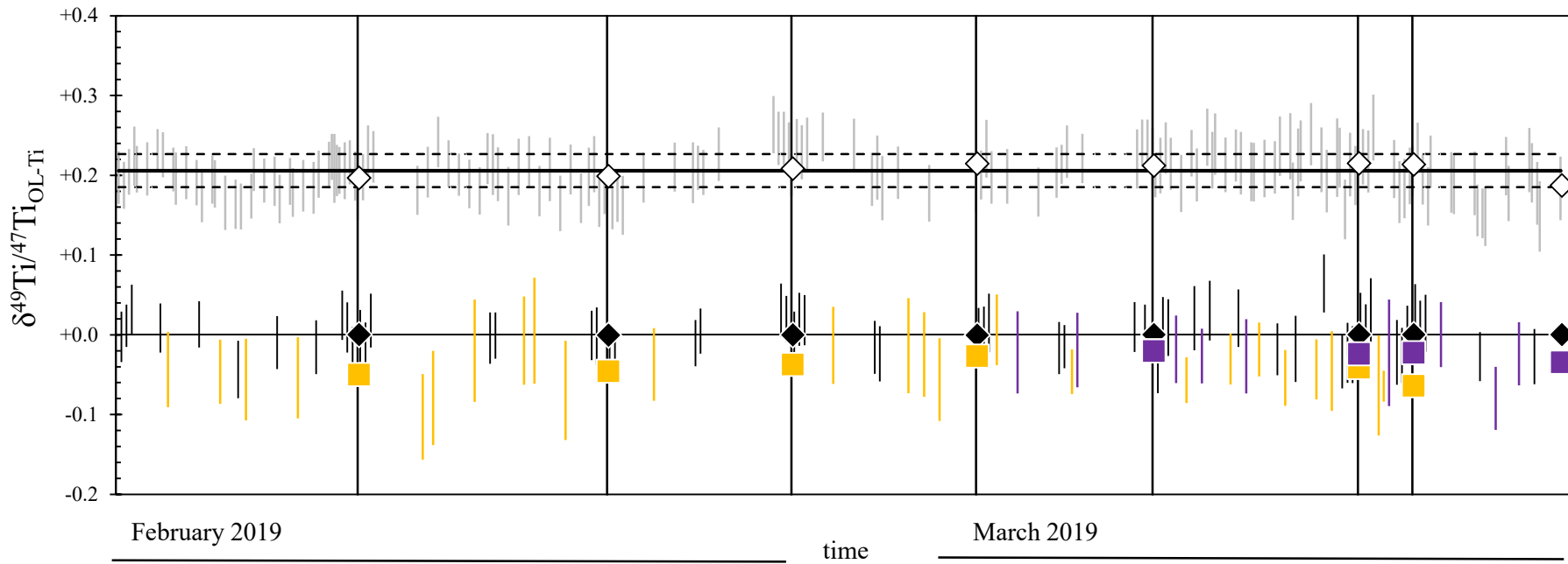
Titanium isotope measurements were performed using the Thermo Neptune Plus MC-ICPMS at Cologne with an intermediate precision better than ± 0.023 ‰ (2 x standard deviation, henceforth s) for spiked reference materials BCR-2, JB-2, OL-Ti, and Col-Ti. Total blank contribution was always less than 10 ng total Ti and is negligible compared to at least 30 μg of processed sample Ti (20 μg for 68115). Samples were also measured using the standard-sample bracketing technique to account for possible unresolved polyatomic interferences and for additional quality control and drift monitoring, in addition to mass-bias correction using the double-spike method. The intermediate precision of these measurements is depicted in Figure 3-8. The best gauge for the precision of the method is the long-term variation of values obtained for terrestrial reference materials (twice the standard deviation, henceforth s), which is always better than 0.023 ‰. Intermediate precision (2 s) of both Col-Ti and OL-Ti are better than 0.021

‰ (2 s). Results for processed reference materials JB-2 and BCR-2 are -0.044 ± 0.023 ‰ (2 s, $n = 7$ sequences) and -0.025 ± 0.012 ‰ (2 s, $n = 4$ sequences), respectively. Both terrestrial reference materials were processed three times and measured between six to 12 times during each sequence. Ideally spiked JB-2 and BCR-2 reproduce previously reported values (Deng *et al.*, 2018a, 2019; Greber *et al.*, 2017b, 2017a; Millet *et al.*, 2016). Two aliquots of BCR-2 were poorly spiked having a sample:spike proportions of 0.85:0.15 rather than the optimal 0.51:0.49 (calculated with the *double spike toolbox*; Rudge *et al.*, 2009). These BCR-2 measurements resulted in erroneously low $\delta^{49}\text{Ti}$ values of ~ -0.2 ‰, which is consistent with the results of standard measurements with sample/spike ratios outside the optimal range (described in section 2.3). With two exceptions all samples have been measured with an $^{44}\text{Ca}/^{47}\text{Ti}_{\text{measured}}$ below 0.0006. The only two exceptions were samples 15055 and 12022, which displayed $^{44}\text{Ca}/^{47}\text{Ti}_{\text{measured}}$ of 0.0016 and 0.0012, respectively. This is still well below the maximum acceptable ratio of 0.01. Given the results of the Ca-interference test, the interferences in the samples are in all cases negligible. Chemically processed OL-Ti and Col-Ti reference materials are identical to their pure, unprocessed counterparts (Figure 3-7, Table 3-1). Except for KREEP-rich sample 68115, all analysed lunar samples and reference materials lie inside the ideal sample:spike range between $^{48}\text{Ti}/^{47}\text{Ti}_{\text{Mix,measured}} = 1.7$ and 3 (Figure 2-5). Sample 68115 has a $^{48}\text{Ti}/^{47}\text{Ti}_{\text{Mix,measured}}$ of ~ 3.7 . Poorly spiked samples systematically yield lower δ -values, which is not observed in this case. The excellent correlation between $\delta^{49}\text{Ti}$ and the U content of KREEP-rich samples, which indicates the presence of a KREEP-component, supports the notion that the determined Ti isotope composition for 68115 is accurate. In addition, it should be noted that two of the BCR-2 reference materials were poorly spiked with a $^{48}\text{Ti}/^{47}\text{Ti}_{\text{Mix}} \sim 4.9$ and resulting in erroneous values ($\delta^{49}\text{Ti}$, ~ -0.2 ‰ instead of -0.015 ‰) consistent with the calibration tests. The sample/spike proportion in this case would be close to 0.85:0.15. Low-Ti mare basalts show small, resolvable variations in $\delta^{49}\text{Ti}$ between -0.030 and $+0.055$ ‰ with an average of $+0.010 \pm 0.015$ ‰ (2 s; $n = 12$, Figure 3-7, Table 3-1. Most high-Ti samples range from $+0.009$ to $+0.047$ in $\delta^{49}\text{Ti}$ (average of $+0.026 \pm 0.036$ ‰, 2 s.; $n = 7$), sample 75035 has a comparatively high $\delta^{49}\text{Ti}$ value of $+0.115$ ‰. The high-Ti average (including 75035) yields a $\delta^{49}\text{Ti}$ of 0.037 ± 0.071 ‰. KREEP-rich lithologies have $\delta^{49}\text{Ti}$ values between $+0.117$ and $+0.296$ ‰.

Table 3-1: Summary of reference materials and measured samples. For reference materials, n gives the number of sequences in which the material has been measured at least 6 times. Abbreviations are the same as in Figure 3-7. Two aliquots of OL-Ti were ran through the chemical separation process and are given as OL-Ti (chemistry).

			$\delta^{49}\text{Ti}$	2 s.	n	95% c.i.
	JB-2		-0.044	0.023	7	0.011
	BCR-2		-0.025	0.012	4	0.010
	OL-Ti mean		0.000	0.001	8	0.000
	OL-Ti (chemistry)		-0.001	0.030	2	0.137
	Col-Ti mean		0.206	0.021	8	0.009
<hr/>						
<i>Low Ti rocks</i>						
12022	Apollo 12	Low-Ti ilm basalt	0.029	0.022	6	0.011
12051		Low-Ti ilm basalt	0.030	0.022	8	0.009
12063		Low-Ti ilm basalt	0.055	0.022	6	0.012
12054		Low-Ti ilm basalt	0.028	0.026	6	0.014
12004		Low-Ti olv basalt	0.006	0.010	6	0.005
12053		Low-Ti pgt basalt	-0.013	0.026	6	0.014
15495	Apollo 15	Low-Ti ONB	0.011	0.017	6	0.009
15555		Low-Ti ONB	-0.008	0.026	6	0.014
15556		Low-Ti ONB	0.007	0.030	6	0.016
15065		Low-Ti QNB	-0.030	0.014	6	0.007
15058		Low-Ti QNB	-0.010	0.034	6	0.018
15545		Low-Ti QNB	0.011	0.032	6	0.017
Low Ti mean \pm 2 s.			0.010		12	0.047
<hr/>						
<i>High Ti rocks</i>						
10017	Apollo 11	High-Ti ilm basalt	0.009	0.024	6	0.012
10020		High-Ti ilm basalt	0.011	0.022	6	0.011
10057		High-Ti ilm basalt	0.009	0.024	6	0.012
74255	Apollo 17	High-Ti ilm basalt	0.043	0.010	6	0.005
74275		High-Ti ilm basalt	0.045	0.010	6	0.005
75035		High-Ti ilm basalt	0.115	0.025	6	0.013
79135		High-Ti bce	0.019	0.017	6	0.009
79035		High-Ti bce	0.047	0.018	6	0.010
High Ti mean 1 \pm 2 s.			0.026		7	0.036
High Ti mean 2 \pm 2 s.			0.037		8	0.071
<hr/>						
<i>KREEP-rich rocks</i>						
14305	Apollo 14	KREEP-rich bce	0.296	0.030	6	0.016
14310		KREEP basalt	0.263	0.035	6	0.018
72275	Apollo 17	KREEP-rich bce	0.185	0.026	6	0.014
68115	Apollo 16	KREEP-rich bce	0.117	0.027	6	0.014





$\delta^{49}\text{Ti}_{\text{JB-2}}$ (average)
 $= -0.042 \pm 0.052\text{‰}$ (2 s.d. individual measurements, $n = 15$)
 $= -0.041 \pm 0.029\text{‰}$ (2 s.d. session mean values, $n = 7$)
 $= -0.043 \pm 0.014\text{‰}$ (95% c.i., $n = 7$)

$\delta^{49}\text{Ti}_{\text{BCR-2}}$ (average)
 $= -0.027 \pm 0.043\text{‰}$ (2 s.d. individual measurements, $n = 9$)
 $= -0.025 \pm 0.012\text{‰}$ (2 s.d. session mean values, $n = 4$)
 $= -0.025 \pm 0.010\text{‰}$ (95% c.i., $n = 4$)

$\delta^{49}\text{Ti}_{\text{ColTi}}$ (average)
 $= 0.204 \pm 0.048$ (2 s.d. individual measurements, $n = 157$)
 $= 0.206 \pm 0.021\text{‰}$ (2 s.d. session mean values, $n = 8$)
 $= 0.206 \pm 0.009\text{‰}$ (95% c.i., $n = 8$)

◆ Sequence average OL-Ti
 ◇ Sequence average Col-Ti
 ■ Sequence average JB-2
 ■ Sequence average BCR-2

Figure 3-8: Intermediate precision (long term reproducibility) for the analysed terrestrial reference materials.

3.4 Discussion

3.4.1 Modelling the Ti isotope composition of urKREEP

The co-genetic relationship between urKREEP and IBC permits studying the $\delta^{49}\text{Ti}$ evolution of both reservoirs. UrKREEP represents the last vestige of the LMO prior to its full crystallization (Warren & Wasson, 1979), and is expected to have developed higher $\delta^{49}\text{Ti}$ due to the prior crystallization of the IBC (Greber *et al.*, 2017b; Millet *et al.*, 2016). Two different approaches have been used to constrain the Ti isotope composition of the pristine urKREEP-component. Pre-existing high-precision HFSE, U, Th and W data by Thiemens *et al.*, (2019) is available for the same samples studied here. UrKREEP is enriched in incompatible elements like U and Th, whereas Ti, Hf and Zr, and Ta are preferentially incorporated into ilmenite, and are therefore expected to have fractionated into the IBC (Gross and Joy, 2016; Münker, 2010; Snyder *et al.*, 1992). Therefore, the U/Ti, U/Hf and U/Zr should be highest in the pristine urKREEP component assuming its coeval formation with the IBC. Moreover, urKREEP should also have the highest $\delta^{49}\text{Ti}$ due to the contemporaneous extraction of lighter Ti isotopes into the IBC (Greber *et al.*, 2017b; Millet *et al.*, 2016). This expectation was met by lunar meteorite SaU 169, which is thought to represent urKREEP, and has an $\delta^{49}\text{Ti}$ of $+0.330 \pm 0.034$ ‰ (Greber *et al.*, 2017b). Two KREEP-rich samples with the highest U/Ti, U/Hf and U/Zr (14310 and 14305) yield $\delta^{49}\text{Ti}$ of $+0.263 \pm 0.018$ and $+0.296 \pm 0.016$ ‰ values that are very similar to those reported for SaU 169 (Greber *et al.*, 2017b). Furthermore, estimates for U/Ti, U/Hf and U/Zr by Warren and Taylor (2014) show that 14305 and 14310 fall well within the estimated range of these ratios for urKREEP (Figure 3-9 a-c). The same can be shown for SaU 169 using trace-element data by Gnos *et al.*, (2004). Assuming the KREEP-rich samples and SaU 169 are in the same range as the U/Zr of the pristine urKREEP-component, the modelling results in a value for $\delta^{49}\text{Ti}_{\text{urKREEP}}$ of $+0.296 \pm 0.067$ ‰ (propagated uncertainty). In a second approach, the evolution of the $\delta^{49}\text{Ti}$ of the LMO, and its Ti, Hf and Ta concentration was modelled, as it crystallises. Millet *et al.*, (2016) assumed all mass-dependent Ti isotope fractionation occurs in the last stages of LMO crystallisation once the solidus of ilmenite is reached.

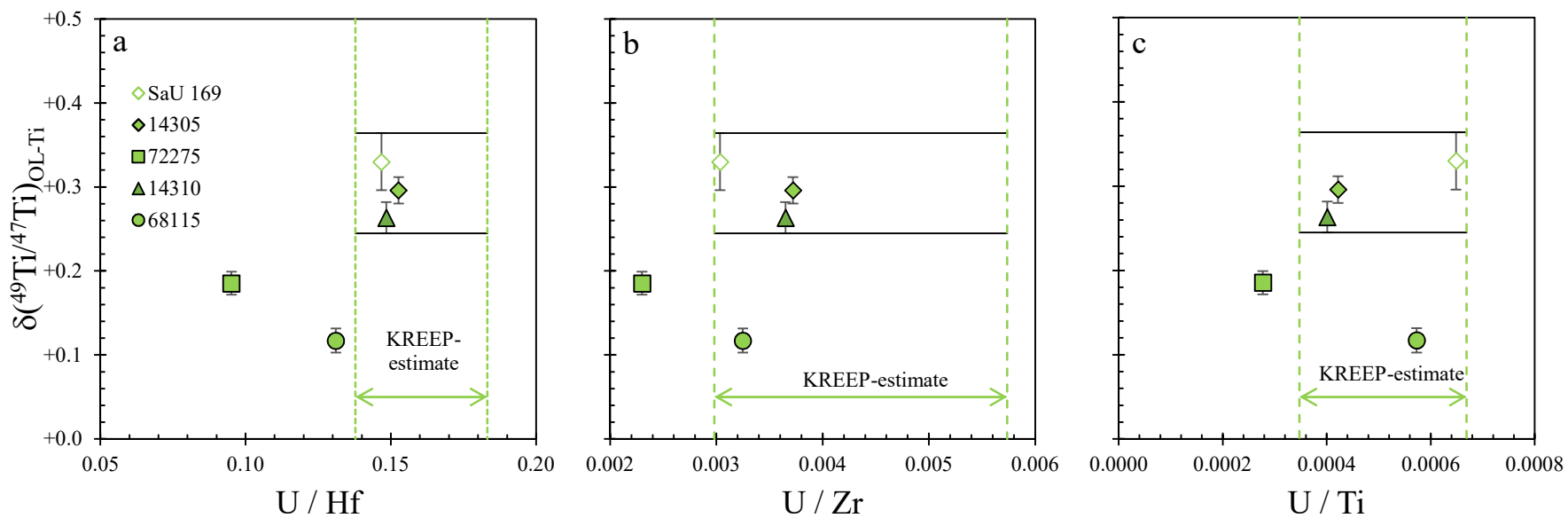


Figure 3-9 a-c: Estimating the $\delta^{49}\text{Ti}$ of KREEP based on HFSE/element ratios for **a)** U/Hf, **b)** – U/Zr and **c)** – U/Ti. Y-axes are identical for a, b and c. KREEP-range constrained by estimates of Warren and Taylor (2014).

The different LMO crystallisation models predict different mineral assemblages but all share a common, late stage ilmenite crystallisation phase (Charlier *et al.*, 2018; Elkins-Tanton *et al.*, 2011; Lin *et al.*, 2017; Rapp and Draper, 2018; Snyder *et al.*, 1992; Wang *et al.*, 2015; Table 3-2). However, silicate minerals, mainly pyroxenes (clino- and orthopyroxene and pigeonite), can also incorporate Ti, causing variations in its bulk partition coefficient ($D_{Ti}^{bulk/melt}$) during LMO crystallisation.

Table 3-2: Relevant mineral assemblages for Trace element and isotope modelling.

Used mineral assemblages						
Xs	OI	Opx	Cpx	Plg	Pig	Ilm
Snyder <i>et al.</i>, (1992)						
10	1					
40		1				
76	0.25			0.53	0.22	
95			0.24	0.32	0.34	0.11
Lin <i>et al.</i>, (2017)						
10	0.83	0.15	0.02			
50	0.36	0.54	0.096			
63.8	0.59	0.34	0.074			
68.5	0.11	0.41	0.138	0.34		
76.1	0.1	0.46	0.144	0.3		
79.3	0.1	0.23	0.072	0.6		
82.8		0.32	0.101	0.58		
87.2		0.35	0.15	0.5		
91.1		0.32	0.235	0.45		0.05
96.4		0.16	0.168	0.39		0.12
Charlier <i>et al.</i>, (2018)						
10	1					
51.1	0.9	0.1				
78.1	0.05	0.2		0.5	0.25	
81.1			0.2	0.48	0.32	
97.1	0.2		0.16	0.42		0.12
Rapp <i>et al.</i>, (2018)						
10	1					
52.3		1				
74.6	0.27	0.06	0.31	0.36		
89.5			0.54	0.46		
97.3			0.5	0.45		0.045
97.8	0.091		0.409	0.27	0.045	0.091

Whatever role these phases may play in fractionating Ti isotopes is currently unknown and merits further study; however, Johnson *et al.*, (2019) have recently suggested silicates have little to no influence on the Ti isotope composition of lavas from Kilauea Iki lava lake. This view has been reinforced by recent *ab initio* modelling by Wang *et al.*, (2019) who found no evidence that substitution of tetravalent Ti in clino- and orthopyroxene results in significant mass-dependent Ti isotope fractionation. Therefore, and as in previous studies, this study will assume that the bulk of the Ti isotope fractionation in the LMO during crystallization is ilmenite-controlled (following Millet *et al.*, 2016). As such, prior to ilmenite saturation, the $\delta^{49}\text{Ti}$ of the LMO will be assumed to be 0‰.

Rapp and Draper (2018) include large fractions of clinopyroxene in their experimentally-constrained model starting from around 75% solidification (between 35% and 50%). Titanium is weakly incompatible into clinopyroxene in its tetravalent form, with $D_{\text{Ti}}^{\text{cpx/melt}}$ of ~ 0.2 (Mallmann and O'Neill, 2009; Leitzke *et al.*, 2016). However, at more reduced lunar $f\text{O}_2$, Ti^{3+} is also present, which is compatible in clinopyroxene with a $D_{\text{Ti}}^{\text{cpx/melt}} \sim 1$ (Leitzke *et al.*, 2018; Mallmann and O'Neill, 2009). As such, the potential presence of Ti^{3+} needs to be considered when assessing the partitioning behaviour of Ti during LMO crystallisation. Using recent mineral/melt partition data from Leitzke *et al.*, (2016), the concentrations of Ti, Hf, Zr, and Ta in the mineral assemblage and the residual liquid can be calculated assuming fractional crystallisation with $C_s = C_0 \cdot DX_l^{(D-1)}$ and $C_l = C_0 \cdot X_l^{(D-1)}$. In these equations, $C_{s,l,0}$, are the concentrations of the modelled element in the solid, liquid and the initial LMO (Snyder *et al.*, 1992), D is its bulk mineral/melt partition coefficient, and X_l the liquid that remains after each LMO crystallisation step. Snyder *et al.*, (1992) do not include Ta in their model, but Münker (2010) calculated Ta contents based on the Nb content given in Snyder *et al.*, (1992) and a Nb/Ta of 17. In addition, Snyder *et al.*, (1992) do not provide a partition coefficient for Ta in pigeonite as they model Nb instead. In this case, Ta partitioning data for a pigeonite-like pyroxene published by van Westrenen *et al.*, (2000) is used.

With ilmenite at liquidus, the bulk solid-melt fractionation factor for Ti ($\Delta T i_{\text{solid-melt}}$) should be almost equal to the oxide-melt fractionation factor ($\Delta T i_{\text{oxide-mel}}$). The Ti isotope composition can then be calculated using a simple Rayleigh distillation model:

$$\Delta T i_{\text{solid-mel}} \approx \Delta T i_{\text{oxide-melt}} = -0.23 \cdot 10^6 / T_2 \quad 3-1$$

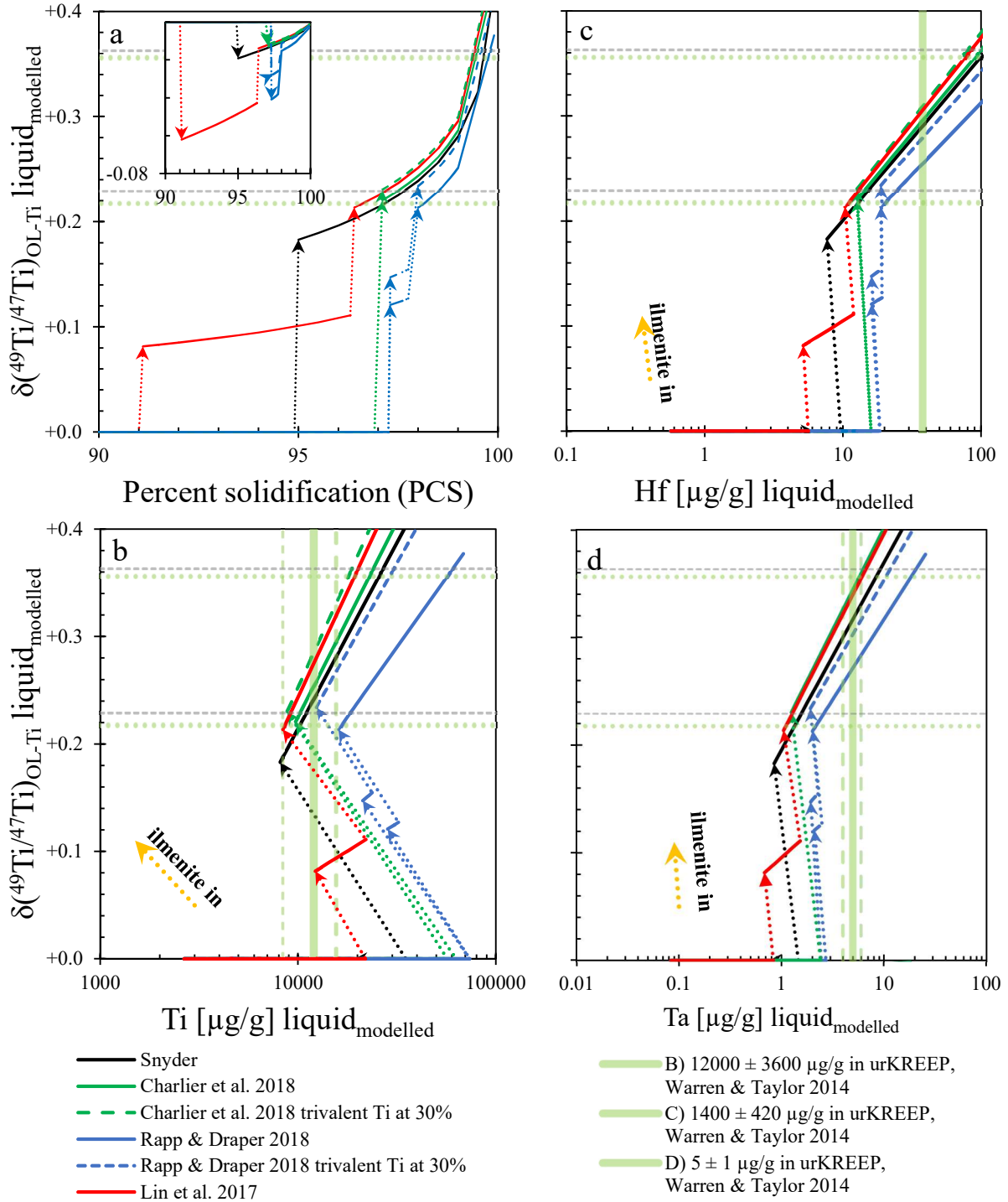


Figure 3-10 a-d: LMO solidification modelling results. All diagrams have identical y-axes and scale. a) Modelled $\delta^{49}\text{Ti}$ as a function of percent solidification, the inset contains the modelled cumulates. b) Modelled Ti concentration in the remaining liquid and $\delta^{49}\text{Ti}$ of the liquid. c) Modelled Hf and d) modelled Zr concentrations in the residual liquid, i.e., urKREEP. Dotted arrows mark the point at which ilmenite is part of the mineral assemblage. Green vertical fields give the estimate of the given element by Warren and Taylor (2014), dashed vertical green lines mark the upper and lower limits of the estimates. For Hf, the limit is smaller than the size of the green bar. Horizontal green and grey lines mark the $\delta^{49}\text{Ti}_{\text{urKREEP}}$ estimate the average intersects evolution of the respective element and using U/Hf, U/Ti and U/Zr, respectively

The intersect between the minimum, average and maximum Ti, Hf and Ta concentrations in urKREEP (Warren and Taylor, 2014), and the modelled $\delta^{49}\text{Ti}_{\text{urKREEP}}$ evolution result in

$\delta^{49}\text{Ti}_{\text{IurKREEP}}$ of $+0.26 \pm 0.10$ ‰, $+0.29 \pm 0.07$ ‰ and 0.31 ± 0.05 ‰, respectively. These values can be used to constrain the Ti isotope composition of the complementary IBC, which results in a $\delta^{49}\text{Ti}_{\text{IBC}}$ of -0.010 ± 0.013 ‰, -0.0075 ± 0.0062 ‰ and -0.0060 ± 0.0034 ‰, respectively.

3.4.2 Modelling the Ti isotope evolution of mare basalts

Several petrogenetic processes can potentially lead to the variations in $\delta^{49}\text{Ti}$ seen in the low- and high-Ti basalt samples. These processes include: 1) partial melting of an IBC, or of an hybridized mantle source in the presence of residual ilmenite; 2) fractional crystallization of ilmenite from a mare basaltic magma; 3) bulk assimilation of IBC, assimilation of IBC followed by fractional crystallization; 4) Mixing between IBC partial melts and a low-Ti magma (*e.g.*, Longhi, 1992; Warren and Taylor, 2014 and references therein). In the following, the Ti, Hf, Ta concentrations and the Ti isotope composition in a mare basalts during these processes are modelled.

Low-Ti mare basalts: Mid- to late-stage cumulates, *i.e.*, (olivine-) pyroxenites (Green *et al.*, 1971; Longhi, 1992) are the inferred source for partial melts that eventually produce low-Ti mare basalts (corresponding to around 50 % - 90 % percent solidification (PCS) found in Charlier *et al.*, 2018; Lin *et al.*, 2017; Rapp and Draper, 2018; Snyder *et al.*, 1992). The concentration of an element in the cumulate (fractional crystallisation, C_s) can be calculated by $C_s = C_0 \cdot DX_l^{(D-1)}$. An aggregate modal fractional melting model is used (Shaw, 1970) to create a partial melt from this cumulate composition. At low degrees of partial melting (between 5 % and 35 %; Binder, 1985), the fractional crystallisation of ilmenite is modelled, with a crystallising mineral assemblage modelled after Apollo 12 low-Ti ilmenite basalt 12063 (10% olivine, 60 % orthopyroxene, 20 % plagioclase and 10 % opaques = ilmenite; Meyer, 2012). Before the occurrence of ilmenite, 99 – 80 % of the total Ti still remains in the melt and determines its isotope composition. As such, the absence of ilmenite leads us to assume an unfractionated Ti isotope composition of the ilmenite-free cumulate (*i.e.*, before ilmenite occurrence $\delta^{49}\text{Ti}_{\text{cumulate}} = 0$ ‰, see also Millet *et al.*, 2016; and Wang *et al.*, 2019). Fractional crystallisation of ilmenite produces a negative, near vertical covariation of $\delta^{49}\text{Ti}$ with Ta/Hf in a low-Ti melt (Figure 3-11 a). However, the partial melt results in a very low Ta/Hf of ~ 0.05 and it is not possible to accurately reproduce the samples in a single or two stage model from

this composition. Increasing the degree of partial melting barely affects the Ta/Hf of the partial melt, as the cumulate itself contains little to no Ta or Hf. All other cumulate compositions from the different LMO crystallization models are tested (Charlier *et al.*, 2018; Lin *et al.*, 2017; Rapp and Draper, 2018; Snyder *et al.*, 1992), and all models resulted in Ta/Hf well below the observed range of Ta/Hf in lunar mare basalts. However, once the cumulate is assumed to contain ilmenite (> 95 % PCS), the Ta/Hf of the resulting partial melt becomes fractionated from its source, due to the higher compatibility of these elements into ilmenite. In this case, the modelled evolution of $\delta^{49}\text{Ti}_{\text{melt}}$, and especially Ta/Hf_{melt}, is consistent with observed values. However, the notion that the low-Ti source could contain ilmenite is not supported by previous studies (Green *et al.*, 1971; Kesson and Ringwood, 1976; Longhi, 1992), and thus a different approach is necessary.

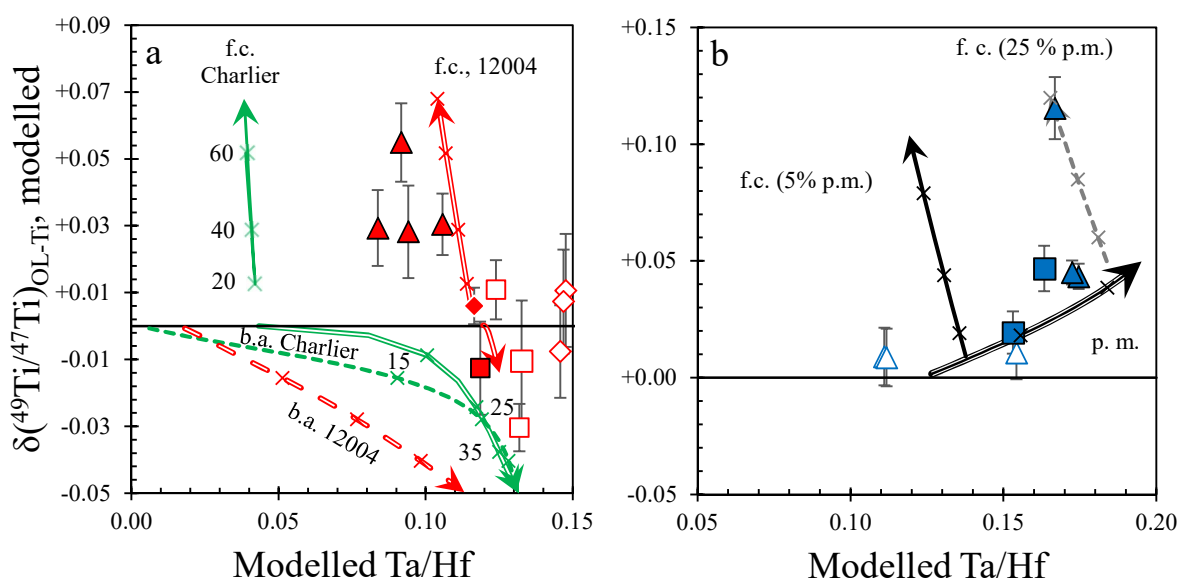


Figure 3-11 a and b: Results for partial melting, fractional crystallisation and AFC. models. a) Modelled evolution lines for $\delta^{49}\text{Ti}$ vs. Ta/Hf for low-Ti samples and b) high-Ti samples. Crosses mark 20 % steps in the fractional crystallisation, 10 % steps in the AFC/bulk addition model (15, 25 and 35 % of fractional crystallisation) and 10 % steps in partial melting model. a) . Solid green and red lines above $\delta^{49}\text{Ti} = 0\text{‰}$ display the trends of fractional crystallisation of ilmenite (f.c.) for the respective source compositions. Fractional crystallisation of ilmenite (green arrow, “f.c., Charlier”) from a partial melt from an ilmenite-free Charlier *et al.*, (2018) cumulate results in a Ta/Hf well below the observed range. Green and red dashed arrow show bulk addition (b.a.) trend for the two different melt compositions of Charlier *et al.*, (2018) (green) 12004 (red). The hollow green and red lines in the negative $\delta^{49}\text{Ti}$ range display the trend for AFC for the same respective sources. High-Ti sample are displayed in b) and are mostly reproduced by partial melting of an IBC (p.m., black, hollow arrow), fractional crystallisation from this source cannot reproduce observed values (f.c., 5% p.m. black solid arrow) at lower degrees of partial melting. Combining partial melting and fractional crystallisation would (f.c., 25% p.m., grey, dashed arrow) would require 35 % partial melting and concurrent fractional crystallisation of up to 60 % to reach observed $\delta^{49}\text{Ti}$ and Ta/Hf of 75035.

If the most primitive sample from this study, the low-Ti mare basalt 12004, represents the ambient lunar mantle composition, then its Ta, Hf and Ti contents may be used as a source

composition in this model. The liquid generated from partial melting of this source composition (15 to 35% melting of an assemblage of 90% PCS Charlier *et al.*, (2018): 20% clinopyroxene, 48 % plagioclase and 32% pigeonite) is then used in a fractional crystallisation model. Fractional crystallisation of minerals in a composition of Apollo 12 low-Ti ilmenite basalt 12063 (10% olivine, 60 % orthopyroxene, 20 % plagioclase and 10 % opaques = ilmenite; Meyer, 2012) results in a decreasing Ta/Hf_{melt} as the $\delta^{49}\text{Ti}_{\text{melt}}$ increases. The 12004-like source composition accurately reproduces the observed $\delta^{49}\text{Ti}$ and Ta/Hf in the analysed low-Ti ilmenite basalts (Figure 3-11 a). This suggests that the Apollo 12 sample 12004 is closer in its HFSE and Ti isotope composition to the source composition of the low-Ti samples than the modelled cumulate compositions. It also suggests that the variations in $\delta^{49}\text{Ti}$ in the low-Ti ilmenite basalts most likely stem from the fractional crystallisation of ilmenite. It is thus also possible to use low-Ti mare basalt 12004 as a reference-point regarding fractional crystallisation of ilmenite in low-Ti mare basalts.

High-Ti mare basalts: Ringwood (1970) reports that Apollo 11 basalts most probably result from the partial melting of an IBC component, which is supported by Shih *et al.*, (1975 and references therein). Based on main- and trace elements constraints, Shih *et al.*, (1975) use the composition of (ilmenite-bearing) Apollo 17 sample 70017 as the initial liquid composition. The more evolved Apollo 11 and Apollo 17 high-Ti mare basalt compositions are then accurately reproduced by a partial melting model. Estimated degrees of partial melting are between ~ 5 % and more than 20 %, respectively (Binder, 1985; Shih *et al.*, 1975). In order to investigate the partial melting of the IBC, and its effect on the Ti isotope composition and the Ta/Hf of the resulting melt and residue, the same source composition and proposed mineral modes utilized by Shih *et al.*, (1975) is used, coupled with the mineral partitioning dataset from Leitzke *et al.*, (2016; consistent with *e.g.*, van Kan Parker *et al.*, 2011) and van Westrenen *et al.*, (2000; for pigeonite). As before, the same fractionation factor for Ti isotopes used by Millet *et al.*, (2016 see equations 3-1 to 3-3) is used, and degrees of melting consistent with previous studies (1 to 25 % melting).

Applying an aggregate fractional melting model to the composition of (ilmenite-bearing) Apollo 17 sample 70017 (similar to Shih *et al.*, 1975), a steady increase in Ta/Hf with degree of partial melting is observed, and a positive covariation between Ta/Hf and $\delta^{49}\text{Ti}$ in the melt. Most of the sample compositions can be reproduced within degrees of partial melting consistent with what was proposed by Shih *et al.*, (1975) and by Binder (1985) in this single stage approach

(between 5 and 25 % melting - Figure 3-11 b). The positive covariation of $\delta^{49}\text{Ti}$ and Ta/Hf, estimated degrees of partial melting (Shih *et al.*, 1975), as well as the model results, strongly support a petrogenesis by partial melting of an ilmenite-rich source (Figure 3-11 b). This possibility is also consistent with the modelled depth of the deep source for high-Ti mare basalts 74275 and 74255 (~250 km; Delano and Lindsley, 1982). Petrographic evidence for early fractional crystallisation of ilmenite (large laths of ilmenite penetrating most other minerals; Meyer, 2012 and references therein) in Apollo 17 sample 75035 may be reconciled by a combination of partial melting and fractional crystallisation: Partial melting (ca. 25%) of a source with the 70017-like composition results in a liquid with a $\delta^{49}\text{Ti}$ value of ~ 0.04 ‰ and a Ta/Hf of ~ 0.18 . Subsequent fractional crystallisation of ilmenite (crystallising mineral assemblage: 15% olivine, 70 % clinopyroxene and 15% ilmenite) from this melt composition can accurately reproduce the observed $\delta^{49}\text{Ti}$ and Ta/Hf of Apollo 17 sample 75035 (after 50 - 60 % fractional crystallisation). This can reconcile the partial melting origin (Shih *et al.*, 1975) and the observations that ilmenite is often a near-liquidus phase in high-Ti mare basalts (Longhi, 1992 and references therein) with the $\delta^{49}\text{Ti}$ and Ta/Hf data. It is nevertheless evident that based on the results and modelling from this study, IBC partial melting plays a major role in high-Ti mare basalt petrogenesis (74275 and 74255). It should also be noted that these trends are mostly constrained by their source composition, which in this case corresponds to that of Apollo 17 sample 70017. It is however possible to model the partial melting of the different ilmenite-bearing cumulates from the LMO models.

3.4.3 Partial melting of different cumulate compositions

Inasmuch as the evolution of $\delta^{49}\text{Ti}_{\text{urKREEP}}$ is concerned, the models by Snyder *et al.*, (1992), Lin *et al.*, (2017), Charlier *et al.*, (2018), and Rapp & Draper (2018) all result in Ti isotope compositions that agree well with the conclusions from this study and those from previous studies (Greber *et al.*, 2017b; Millet *et al.*, 2016). The previous section showed that partial melting of late-stage ilmenite-bearing cumulates likely plays a key role in high-Ti mare basalt petrogenesis (*e.g.*, Shih *et al.*, 1975; Sossi and Moynier, 2017). Here, the effect of partial melting of the different late stage IBC compositions, as produced by the different LMO solidification models, on the $\delta^{49}\text{Ti}_{\text{melt}}$ and $\text{Ta}/\text{Hf}_{\text{melt}}$ of the melt is constrained. Like in sections 3.5.1 and 3.5.2, the partition coefficients by Leitzke *et al.*, (2016) and van Westrenen *et al.*,

(2000; for pigeonite), the petrogenetic source composition of the ilmenite-bearing cumulate at 99 % PCS of each LMO crystallization model and the calculated Ti, Hf, and Ta concentrations are used. With ilmenite now present, the Ti isotope composition of the IBC for each model can be constrained with:

$$R_{X,cumulate} = R_0 / \left(\frac{X_{cumulate}}{X_0} \right)^{(\alpha-1)} \quad 3-4$$

The $\delta^{49}\text{Ti}_{\text{modelled}}$ versus $\text{Ta}/\text{Hf}_{\text{modelled}}$ for each LMO solidification model is shown in Figure 3-12. Results obtained using the Snyder *et al.*, (1992) model yield the minimum values for $\delta^{49}\text{Ti}_{\text{melt}}$, $\text{Ta}/\text{Hf}_{\text{melt}}$, whereas the Rapp and Draper (2018) result in the maximum values for $\delta^{49}\text{Ti}_{\text{melt}}$ and $\text{Ta}/\text{Hf}_{\text{melt}}$. The Charlier *et al.*, (2018) model and the Lin *et al.*, (2017) model overlap during the entirety of the evolution and evolve from $\text{Ta}/\text{Hf}_{\text{melt}}$ lower than that predicted with the Snyder *et al.*, (1992) model to higher $\text{Ta}/\text{Hf}_{\text{melt}}$ at the same $\delta^{49}\text{Ti}_{\text{melt}}$.

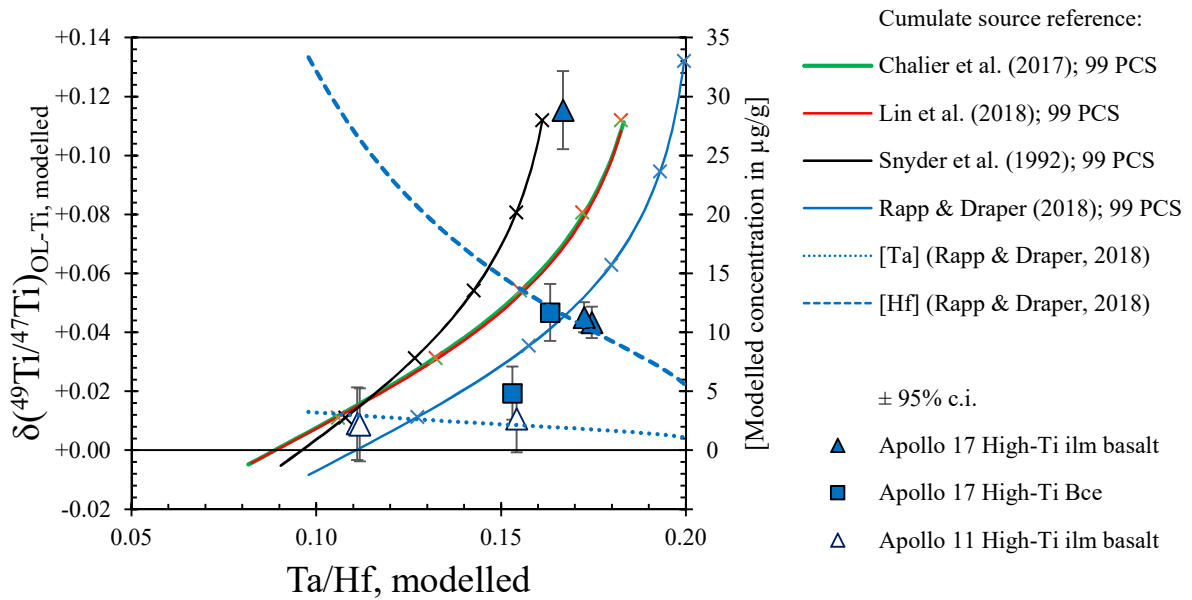


Figure 3-12: Modelled Ti isotope composition and Ta/Hf during partial melting of an ilmenite-bearing cumulate. IBC composition corresponds to the respective model. Each cross mark represents a 10% increase in partial melting degree. Dashed and dotted line are the modelled Hf and Ta concentration in the melt for the Rapp & Draper (2018) model.

The evolution line calculated assuming the Rapp & Draper (2018) LMO evolution model fits best with most samples. The two high-K high-Ti Apollo 11 basalts intersect with the Rapp and

Draper (2018) model between 5 and 10 % partial melting, which is consistent with has been predicted by Shih *et al.*, (1975). Most of the Apollo 17 high-Ti samples are reproduced by the Rapp & Draper (2018) model curve at 10 – 20 % partial melting, while the $\delta^{49}\text{Ti}$ and Ta/Hf of Apollo 17 high-Ti basalt 75035 is reached at around 50 % of partial melting. These results reinforce the notion that the high-Ti mare basalts analysed in this study are the products of partial melting of the IBC in the presence of residual ilmenite, and that the variations in $\delta^{49}\text{Ti}$ and Ta/Hf can potentially be explained with partial melting alone.

3.4.4 Assimilation of an IBC component by a low-Ti magma

While the TiO_2 contents in the Apollo 15 samples are too low to be consistent with the assimilation of IBC during fractional crystallisation, it is worth investigating this process in light of high-Ti mare basalt petrogenesis. Three approaches are used to constrain the admixing of an IBC component into a low-Ti magma: Bulk addition of a portion of an IBC into a low-Ti magma, assimilation-fractional crystallisation (henceforth AFC, described in DePaolo, 1981), and mixing of an 12004-derived magma with and IBC-derived magma. Kesson and Ringwood (1976) mention that in order to reach the TiO_2 contents found in high-Ti mare basalts, the low-Ti parental magma would need to assimilate up to 60 % of IBC material. The authors further point out that this range of AFC is problematic because the high-Ti basalt parental magma would need experience up to 40 – 45 % of fractional crystallization in order to produce the required heat to drive wall-rock assimilation, which is hard to reconcile with the Mg# and Cr-contents of high-Ti mare basalts. In section 3.4.2 it is pointed out that using the composition of the most primitive low-Ti sample (12004), in lieu of a modelled cumulate, accurately reproduces the analysed low-Ti ilmenite basalts. For both AFC and bulk addition, a liquid produced from the modelled cumulate (90 % PCS; Charlier *et al.*, 2018) is used. In addition, the same mineral assemblage as 90 % PCS Charlier *et al.*, (2018), but with a 12004-like trace element composition will be used to model the same processes. Millet *et al.*, (2016) constrain a Ti isotope composition of these late stage IBC components between $\delta^{49}\text{Ti}_{\text{cumulate}} = -0.1 \text{ ‰}$ and $\sim 0 \text{ ‰}$. With the onset of ilmenite crystallisation all the models initially result in $\delta^{49}\text{Ti}$ above the Millet *et al.*, (2016) estimate of -0.06 ‰ to -0.01 ‰ , which is likely due to the different model approaches. Specifically, while Millet *et al.*, (2016) assume that at the point of ilmenite occurrence the amount of Ti remaining in the melt is 100%, the model considers that up to 15%

of the bulk Ti resides in LMO silicates at the point of ilmenite-saturation (Millet *et al.*, 2016). The closest modelled cumulate composition that is consistent with the estimate for the high-Ti source of Millet *et al.*, (2016) is the Lin *et al.*, (2017) cumulate (91% PCS, $\delta^{49}\text{Ti}_{\text{cumulate}} = -0.06$ ‰; Millet *et al.*, (2016) $\delta^{49}\text{Ti}_{\text{cumulate}} = -0.068$ ‰). This IBC component, containing 5 % of ilmenite, is assimilated (AFC) by a low-Ti magma (at 20 % partial melting). With ongoing fractional crystallisation of this low-Ti basaltic magma (crystallising mineral assemblage 60 % olivine, 40 % opx + cpx), the portion of assimilated IBC material to 45 % is subsequently increased. For bulk-addition, the same partial melt composition as for AFC is used. Via a mass balance $c_{\text{tot}} = c_{\text{low-Ti}}X_{\text{low-Ti}} + c_{\text{IBC}}(1 - X_{\text{low-Ti}})$ an increasing amount of the IBC component ($\delta^{49}\text{Ti}_{\text{cumulate}} = -0.06$ ‰) is added into the melt as fractional crystallisation proceeds (crystallising mineral assemblage 60 % olivine, 40% opx + cpx). The models (Figure 3-11 a) consistently show that $\delta^{49}\text{Ti}$ and Ta/Hf of the melt converge towards the IBC compositions, as this component dominates the HFSE and Ti budget. Both AFC and bulk-addition models evolve slightly differently with regards to their source. This is because the 12004-like composition initially starts with significantly higher Ta and Hf compared to the modelled cumulate. These higher concentrations lessen the impact of IBC-assimilation onto the 12004-derived magma in both processes. In all cases, however, the mixing process imparts a negative $\delta^{49}\text{Ti}$ onto the existing melt as assimilation proceeds. This effect is smallest in the AFC-evolution line from the 12004-derived composition, as the initial Ti concentration of the melt is initially higher than for the modelled cumulate. This in turn dilutes the Ti isotope composition imparted onto the melt by the IBC component. In a third approach, the mixing between an IBC-derived partial melt and a low-Ti partial melt is modelled. Similar to section 3.4.2, the composition of (ilmenite-bearing) Apollo 17 sample 70017 (similar to Shih *et al.*, 1975) is used as an IBC-derived partial melt. The low-Ti magma is a partial melt from the 90 % PCS Charlier *et al.*, (2018) cumulate assemblage with the 12004-like composition. With an aggregate fractional melting model, a partial melt from both source compositions is modelled. These two generated melts are then mixed in three scenarios: The IBC-derived partial melt (fixed at 10%) is mixed into the low-Ti melt in a fixed mixing proportion of 0.2:0.8, while the degree of partial melting in the low-Ti melt is subsequently increased up to 35 %. In the second scenario, a partial melt from the IBC (fixed at 10 % partial melting) is mixed into a low-Ti magma (fixed at 25 % partial melting) in gradually increasing proportions. Lastly, an IBC-derived partial melt (fixed at 25 % partial melting) is mixed into a low-Ti magma (fixed at 25 % partial melting). Again, the proportion of the IBC-derived melt admixed into the low-Ti melt is subsequently increased.

The concentrations of the resulting magma-mixture are calculated with a mass balance $c_{\text{tot}} = c_{\text{low-Ti}}x_{\text{low-Ti}} + c_{\text{IBC}}(1-x_{\text{low-Ti}})$. Due to the absence of ilmenite in the source of the low-Ti melt, its Ti isotope composition is expected to be unfractionated relative to OL-Ti. The IBC-derived melt will have fractionated, *i.e.*, positive $\delta^{49}\text{Ti}$ due to the partial melting of ilmenite-bearing cumulate. In the first scenario, the Ta/Hf of the low-Ti magma decreases in the mixture from ~ 0.2 to 0.15 at low degrees of partial melting, with only a small increase in $\delta^{49}\text{Ti}$. At around 6 % partial melting, the resulting melt shows an increase in both its Ta/Hf and $\delta^{49}\text{Ti}$. Finally, at 35 % partial melting, the resulting mixed melt has a Ta/Hf of ~ 0.14 and a $\delta^{49}\text{Ti}$ of $\sim +0.015$, well below the observed range for high-Ti mare basalts. However, as the proportion of IBC steadily increases, the mixture of the two partial melts (fixed at 10% partial melting for IBC-component and 25% partial melting for the low-Ti component, respectively) is characterised by a steady increase of $\text{Ta/Hf}_{\text{melt}}$ and $\delta^{49}\text{Ti}_{\text{melt}}$. In order to reach even the observed range of $\delta^{49}\text{Ti}$ and Ta/Hf in high-Ti mare basalts, the required proportion of IBC-material in the mixed melt would need 100 % of IBC-derived material (essentially 0 % of the low-Ti magma), which is an unrealistic expectation. In the third scenario, the degree of partial melt for the IBC-component is increased to 25 %. Again, the scenario (fixed IBC-derived partial melt 25 %, fixed low-Ti derived partial melt 25 %, and subsequently increasing addition of IBC-melt into the mixture) only reaches the observed range of $\delta^{49}\text{Ti}$ and Ta/Hf in high-Ti mare basalts once the partial melt is essentially exclusively derived from the IBC component. The observed range of $\delta^{49}\text{Ti}$ and Ta/Hf in the high-Ti basalts cannot be explained by mixing. The IBC component partial melting model in section 3.4.2 shows that the observed range in $\delta^{49}\text{Ti}$ and Ta/Hf in Apollo 17 high-Ti samples is accurately reproduced after 20-30 % partial melting. The low-Ti magma is not expected to have experienced prior Ti isotope fractionation, thus the $\delta^{49}\text{Ti}_{\text{melt}}$ in this mixing model is constrained by the partial melt generated from the IBC component. Even if a melt (45-50 % partial melting) would be assimilated by a low-Ti magma, as long as it does not consist of 100 % IBC-derived melt, the $\delta^{49}\text{Ti}$ of the resulting mixture would be lower (*i.e.*, diluted) by a low-Ti magma with an $\delta^{49}\text{Ti} = 0$ ‰.

3.4.5 Identifying magmatic processes in lunar basalt sources

The average $\delta^{49}\text{Ti}$ values obtained for low- and high-Ti mare basalts ($+0.010 \pm 0.015$ ‰ and $+0.037 \pm 0.071$ ‰) are consistent with findings by Millet *et al.*, (2016) and are indistinguishable

from their Bulk Silicate Earth estimate (BSE: $+0.005 \pm 0.005$ ‰, 95% c.i.; see Figure 3-1). The $\delta^{49}\text{Ti}$ value of the most primitive sample, the Apollo 12 olivine basalt 12004 (possibly tapping bulk lunar mantle) is identical with the $\delta^{49}\text{Ti}_{\text{BSE}}$ estimate by Millet *et al.*, (2016) and the chondritic $\delta^{49}\text{Ti}$ value proposed by Greber *et al.*, (2017b) but lower than the chondritic $\delta^{49}\text{Ti}$ value suggested by Deng *et al.*, (2018b).

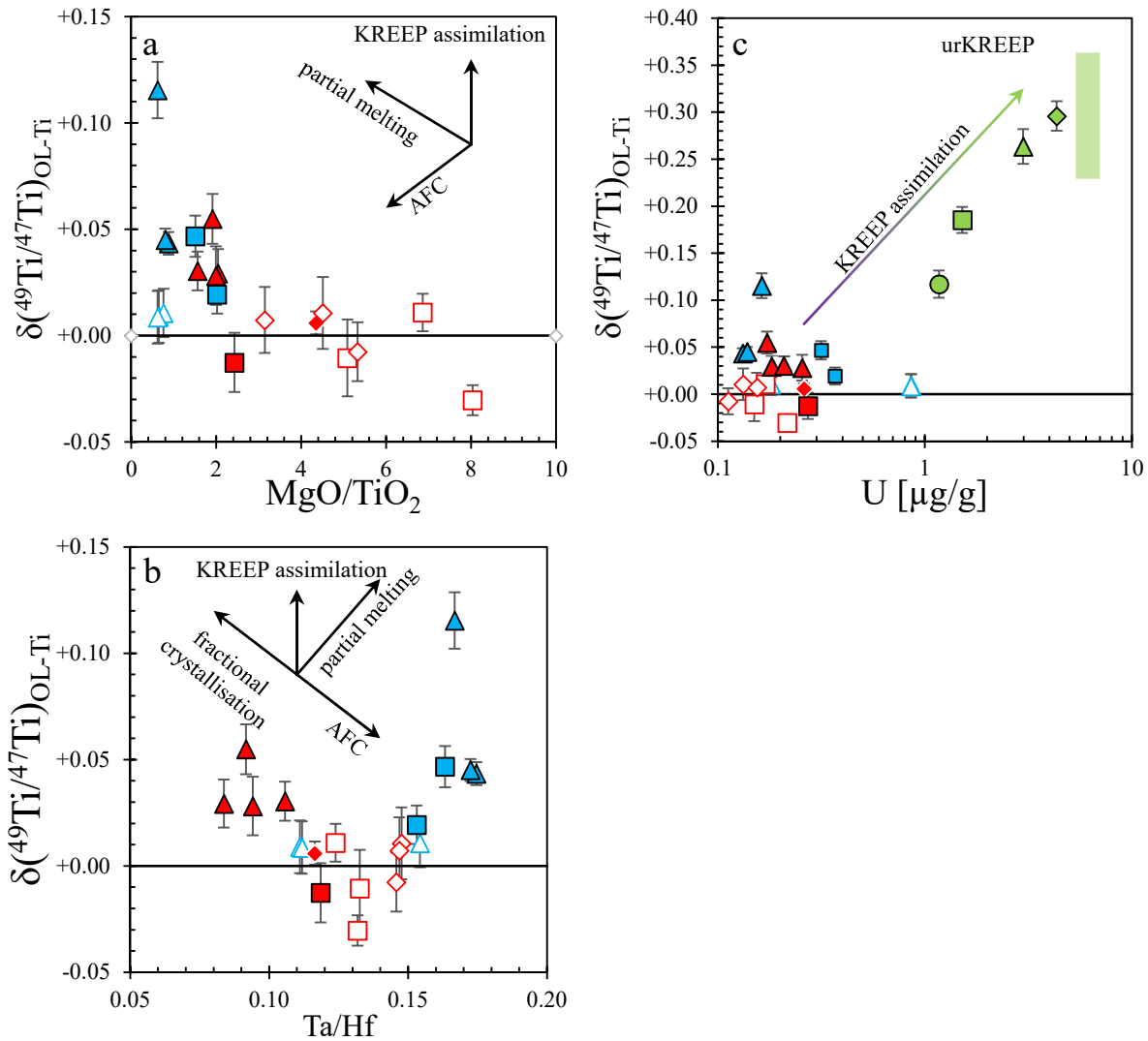


Figure 3-13 a-c: Plots of a) $\delta^{49}\text{Ti}$ vs. MgO/TiO_2 , b) $\delta^{49}\text{Ti}$ vs. Ta/Hf and c) $\delta^{49}\text{Ti}$ vs. U . These can be used to discriminate between processes leading to variations in $\delta^{49}\text{Ti}$. Symbols are the same as in Figure 3-7, black arrows indicate the direction in which a process would influence the values along y- and x-axes. Partial melting assumes the presence of ilmenite in the source, fractional crystallisation always implies fractional crystallisation of ilmenite. AFC implies the assimilation of an IBC-component during ilmenite-free fractional crystallisation of a low-Ti magma. b) The estimated Ta/Hf value of urKREEP is ~ 0.11 (Warren and Taylor, 2014). c) Contamination by urKREEP (coloured arrow), would imply higher U contents (not observed). urKREEP is based on the first model.

Possible explanations for the observed intra-group $\delta^{49}\text{Ti}$ variations in mare basalts include fractional crystallisation of ilmenite during petrogenesis, assimilation of an IBC- or KREEP-

component during fractional crystallisation, partial melting an IBC or mantle source heterogeneity. To distinguish between these processes the results of experimental studies that simulated the petrogenesis of lunar basalts are considered (see the relevant sub-section in 3.2.1; Longhi, 1992 and references therein). For instance, experimentally synthesised low-Ti-like samples showed that ilmenite has been one of the first solidus phases (Longhi, 1992 and references therein), which would preferentially incorporate light Ti isotopes, increasing the $\delta^{49}\text{Ti}_{\text{melt}}$ during fractional crystallisation of ilmenite (Millet *et al.*, 2016). High-Ti basalts from Apollo 17 were shown to originate from greater depths than Apollo 12 and 15 low-Ti and were successfully modelled by partial melting of an ilmenite-rich source (Longhi, 1992 and references therein). This can explain the observed elevated $\delta^{49}\text{Ti}_{\text{high-Ti}}$ values (See Figure 3-12; Millet *et al.*, 2016). In contrast, the full assimilation of an IBC-component during fractional crystallisation of a low-Ti magma would decrease the $\delta^{49}\text{Ti}$ value of the basaltic melt (Figure 3-11 a). Thus, the small intra-group variations in $\delta^{49}\text{Ti}$ values of low- and high-Ti basalts can best be explained by fractional crystallisation of ilmenite and melting of ilmenite-bearing sources, respectively. In addition to experimental petrological studies, geochemical tools can help distinguish between the discussed processes. For example, the compatibility of HFSEs in ilmenite is variable (Münker, 2010): Tantalum is the most compatible HFSE in ilmenite, whereas Hf is the most incompatible (*e.g.*, $D_{\text{Ta}} > 1 > D_{\text{Hf}}$; Leitzke *et al.*, 2016; or $D_{\text{Ta}} > D_{\text{Hf}}$, van Kan Parker *et al.*, 2011). Thus, fractional crystallisation of ilmenite would increase the $\delta^{49}\text{Ti}_{\text{melt}}$ (Millet *et al.*, 2016) but decrease the Ta/Hf_{melt} (Münker, 2010). In contrast, partial melting of an IBC-component would increase the Ta/Hf_{melt} and the $\delta^{49}\text{Ti}_{\text{melt}}$ value ($D_{\text{Ta}} \sim 2 \times D_{\text{Hf}}$ for ilmenite, Leitzke *et al.*, 2016). Apollo 12 low-Ti ilmenite basalts show lower Ta/Hf and positive $\delta^{49}\text{Ti}$ relative to the most primitive lunar basalt analysed in this study, (12004, see Figure 3-11 and 3-13), indicating the early fractional crystallisation of ilmenite, which is consistent with experimental results (Longhi, 1992 and references therein). Relatively low $\delta^{49}\text{Ti}$ values in Apollo 15 low-Ti basalts may indicate the assimilation of an IBC material (Longhi, 1992 and references therein). However, assimilation of an IBC-component seems inconsistent with relatively low Ta/Hf and comparatively low TiO₂ contents of ~ 1.3 %. The assimilation of a KREEP-component would cause a substantial increase in $\delta^{49}\text{Ti}$ and U concentration of the melt while barely fractionating Ta/Hf. Such trends are not observed indicating that KREEP-components played an insignificant role during the petrogenesis of low- and high-Ti basalts (Figure 3-13 c). Apollo 17 high-Ti samples are rich in TiO₂, exhibit relatively low MgO/TiO₂ but high $\delta^{49}\text{Ti}$ and higher Ta/Hf relative to the most primitive sample. In agreement with the

experimental evidence, this geochemical pattern strongly indicates partial melting of an IBC-component during the petrogenesis of Apollo 17 high-Ti basalts (Longhi, 1992 and references therein).

3.4.6 Other isotope systems

Elements with similar partitioning behaviour to Ti should be affected by the same processes, *i.e.* fractional crystallisation and partial melting, respectively. The partitioning of such elements should also lead to isotope fractionation, if the coordination in melt and mineral are similar to Ti.

Vanadium: Vanadium and its isotopes behave similarly to Ti and Fe (*e.g.*, Millet *et al.*, 2016; Sossi and Moynier, 2017), and should primarily be fractionated during crystallisation or melting of ilmenite (Ringwood, 1970). Hopkins *et al.*, (2019) determined V isotopes for a representative range of lunar samples. The observed V isotope variations by Hopkins *et al.*, (2019) show no systematic covariation with TiO₂ or SiO₂. It is demonstrated in their study that the variation in $\delta^{51}\text{V}/^{50}\text{V}_{\text{AlfaAesar}}$ is directly proportional to exposure age and the Ti and Fe content in the sample. As such, after correction for neutron capture (nc) effect, V isotope compositions show no resolvable variations relative to the Earth.

Hafnium (coupled with Neodymium): Sprung *et al.*, (2013) could associate heterogeneous petrogenetic sources to Apollo mare basalts after nc-correction using Hf and Nd isotope systematics. Although promising, the number of samples where ϵNd_i and μHf_i as well as $\delta^{49}\text{Ti}$ have been determined is too small to come to any robust conclusion regarding the effect of source heterogeneity on the Ti isotope composition.

Iron: As in the case of Ti, Fe is compatible in ilmenite and displays lower spatial coordination in silicate melts, and because of this, ilmenite-melt equilibria during melting or crystallization will lead to mass-dependent Fe isotope fractionation (Sossi and Moynier, 2017 and references therein). Poitrasson *et al.*, (2004) observe a systematic shift towards heavier Fe isotope compositions in lunar samples relative to the Earth. Later studies found that the Mg Suite rocks have lower $\delta^{57}\text{Fe}/^{54}\text{Fe}_{\text{IRMM-014}}$ (henceforth $\delta^{57}\text{Fe}$) than low-Ti basalts, which in turn have lower $\delta^{57}\text{Fe}$ than high-Ti mare basalts (Poitrasson *et al.*, 2019; Sossi and Moynier, 2017; Weyer *et al.*, 2005). The bimodal $\delta^{57}\text{Fe}$ distribution of low-Ti and high-Ti mare basalts is attributed to

whether ilmenite is involved or not during partial melting (Sossi and Moynier, 2017; Sossi and O’Neill, 2017). The higher $\delta^{57}\text{Fe}$ of high-Ti mare basalts originates from the partial melting of their ilmenite-bearing source (IBC), which is supported by previous experimental studies (Shih *et al.*, 1975) and by findings from this study using Ta/Hf and $\delta^{49}\text{Ti}$ systematics. Observed intra-group variations of $\delta^{49}\text{Ti}$ in low-Ti ilmenite basalts, ONBs and QNBs in this study do not persist in Fe isotope compositions reported by Weyer *et al.*, (2005), Sossi and Moynier (2017) or Poitrasson *et al.*, (2019). The absence of a distinguishable Fe isotope signature of fractional crystallisation of ilmenite or lack thereof in low-Ti mare basalts is consistent with the uniform Fe fractionation factor for olivine and ilmenite of $\Delta^{57}\text{Fe}_{\text{Ilm-Ol}} = +0.01 \text{ ‰}$ (Sossi and O’Neill, 2017). This uniform Fe fractionation factor imparts $\delta^{57}\text{Fe}$ of the same magnitude onto low-Ti ilmenite basalts, ONBs and QNBs. The different fractionation behavior of Ti and Fe reveal an offset in low-Ti ilmenite basalts compared to ONBs/QNBs and high-Ti mare basalts (Figure 3-12 a). Consequently, a coupled $\delta^{49}\text{Ti}$ - $\delta^{57}\text{Fe}$ study may be able to investigate the petrogenetic processes of lunar sample in further detail, especially as comparatively high elemental abundances require low sample volumes. The number of samples where both Ti and Fe isotope compositions have been determined however is yet too little to confidently investigate the different petrogenetic trends in $\delta^{57}\text{Fe}$ vs. $\delta^{49}\text{Ti}$ or Ta/Hf.

Chromium: Mass-dependent isotope variations have also been reported for moderately volatile Cr (Bonnand *et al.*, 2016). Chromium in general can be compatible in pyroxene, spinel and ilmenite (Leitzke *et al.*, 2016). At lunar $f\text{O}_2$, the predominant Cr species is Cr^{2+} , whereas its dominant terrestrial redox species is Cr^{3+} . The difference in $\delta(^{53}\text{Cr}/^{52}\text{Cr})_{\text{NBS-979}}$, henceforth $\delta^{53}\text{Cr}$, between Bulk Silicate Earth and Bulk Silicate Moon is attributed to mass-dependent fractionation during to evaporative loss (Sossi *et al.*, 2018). Unlike in Ti and Fe isotope systematics, fractional crystallisation of Cr-bearing minerals imparts a lighter $\delta^{53}\text{Cr}$ onto the melt. The variations of $\delta^{53}\text{Cr}$ in low-Ti and high-Ti mare basalts are consistent with fractional crystallisation of pyroxene and spinel (Apollo 12 low-Ti mare basalts) and (pyroxene,) spinel and ulvospinel (Apollo 11 and 17 high-Ti mare basalts; Bonnand *et al.*, 2016). If both Cr and Ti were to be affected by fractional crystallisation, a negative covariation between $\delta^{49}\text{Ti}$ and $\delta^{53}\text{Cr}$ would be expected. This is especially interesting given an observed negative covariation of $\delta^{53}\text{Cr}$ vs. TiO_2 in Apollo 12 low-Ti samples analysed by Bonnand *et al.*, (2016). Low-Ti ilmenite basalts should have experienced fractional crystallisation of ilmenite and ulvo-spinel (supported by this study and the steady decrease in TiO_2 -contents observed in Bonnand *et al.*, 2016). However, even combining data from Millet *et al.*, ($\delta^{49}\text{Ti}$; 2016) Bonnand *et al.*, ($\delta^{53}\text{Cr}$;

2016), Sossi *et al.*, ($\delta^{53}\text{Cr}$; 2018), available data are scarce. Sample groups where both systems have been determined include two Apollo 11 samples (sample 10057 was measured by both Bonnand *et al.*, (2016) and Sossi *et al.*, (2018)), one Apollo 12 sample, one Apollo 14 sample, three Apollo 15 samples (sample 15555 has been determined by Bonnand *et al.*, (2016), and Sossi *et al.*, (2018)) and three Apollo 17 samples (negative correlation, Figure 3-14 b). While promising, to the scarcity of available data prevents us to reliably investigate possible coupled mass-dependent isotope variations in $\delta^{53}\text{Cr}$ and $\delta^{49}\text{Ti}$ for these samples.

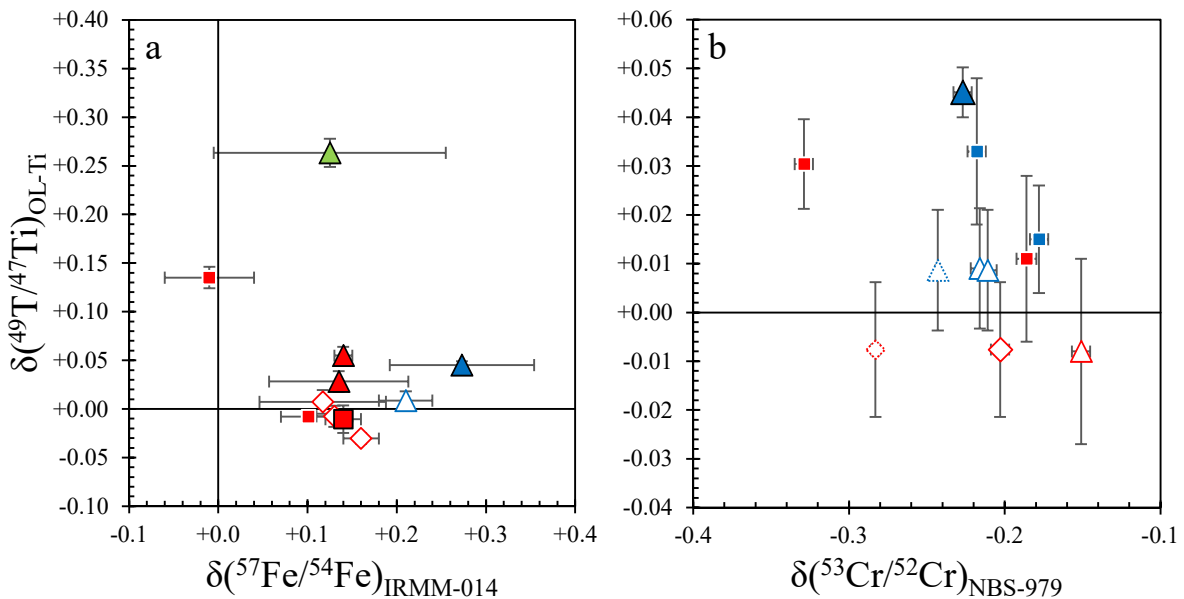


Figure 3-14 a and b: Ti isotope compositions vs. other stable isotope systems a) Coupled Fe and Ti isotope compositions of lunar samples. Additional Fe and Ti isotope data provided by previous studies basalts (Ti data: Millet *et al.*, 2016; Iron data: Poitrasson *et al.*, 2019; Sossi and Moynier, 2017; Weyer *et al.*, 2005). b) Coupled Cr and Ti isotope compositions of lunar samples. Data compilation includes data from studied by Millet *et al.*, (2016), Bonnand *et al.*, (2016) and Sossi *et al.*, (2018). Dotted symbols in b) are samples where two Cr isotope compositions have been determined (samples 10057 and 15555). Uncertainties for Fe and Cr are (recalculated) 2.s.e., uncertainties for Ti are 95% c.i..

3.5 Conclusion

New Ti isotope data for a representative set of lunar samples show that there is a clear offset between KREEP-rich samples and mare basalts, in agreement with previous work (Greber *et al.*, 2017b; Millet *et al.*, 2016). Data reveal intra-group variation amongst olivine- and quartz-normative and (low-Ti) ilmenite mare basalts with the latter recording higher $\delta^{49}\text{Ti}$ than the former. High-Ti mare basalts have overall higher $\delta^{49}\text{Ti}$. The $\delta^{49}\text{Ti}$ of the lunar sample suite, coupled with HFSE data, suggests that the fractional crystallisation of ilmenite and partial

melting of an IBC-component are the principal processes affecting the $\delta^{49}\text{Ti}$ of Apollo 12 low-Ti mare basalts, and of Apollo 17 high-Ti mare basalts, respectively. This conclusion is consistent with results of previously published experimental studies (Longhi, 1992 and references therein). This is in excellent agreement with previous experimental data and the high $\delta^{57}\text{Fe}$ of high-Ti mare basalts (Charlier *et al.*, 2018; Longhi, 1992; Sossi and Moynier, 2017; Weyer *et al.*, 2005). Based on coupled HFSE and $\delta^{49}\text{Ti}$ data, the petrogenesis of high-Ti mare basalts by assimilation of IBC-component by low-Ti magma is unlikely.

CHAPTER 4

TITANIUM ISOTOPE VARIATIONS IN
SUBDUCTION ZONE DERIVED ROCKS

4.1 Introduction

4.1.1 Convergent plate margins and arc volcanism

Subduction plays a key role in terrestrial tectonics, melt generation and crustal evolution (Stern, 2002). The denser downgoing oceanic slab and its overlying sedimentary cover are gradually brought to greater depths. The water-rich fluids released during slab de-hydration lower the solidus of the subducting slab and/or the overlying peridotitic mantle wedge promoting partial melting. For instance, the trace element budget of subduction zone related rocks is characterised by four primary components, the mantle wedge, subducted oceanic crust, subducted metasediments, and the arc lithosphere (McCulloch and Gamble, 1991; Pearce and Peate, 1995). While the exact process of geochemical mixing in subduction zone settings is not yet well constrained, two models describe the process (Figure 4-1). In the first model, the down going slab dehydrates and the migrating fluids induce partial melting of the overlying peridotitic mantle (Schmidt and Poli, 1998; Stern, 2002). An alternative solution may be provided by a mechanical mixture of these three components that forms on the slab-mantle boundary. This tectonic *mélange* may contain varying contributions from the respective components (Codillo *et al.*, 2018; Cruz-Uribe *et al.*, 2018; Marschall and Schumacher, 2012; Nielsen and Marschall, 2017). The resulting lava can show large variations in their trace element concentrations and ratios, like those sensitive to, for example, fluid-mobility (W/Th, W/U or Mo/Th), residual phases such as rutile (like Nb/Ta, Hf/Zr) or amphibole (such as Th/La and Zr/Sm). The study of the trace element systematics of subduction-related magmatic samples allow the detailed assessment of their provenance and insights into the petrogenetic processes taking place in the subduction zone itself (*e.g.*, König *et al.*, 2008; Schuth *et al.*, 2009). In particular, fluid-mobile W or variations in HFSE ratios can be used to investigate whether there was a fluid-like or a melt-like component that dominates the trace element budget of subduction- related arc basalts (*e.g.* Cyprus; Fonseca *et al.*, 2017; König *et al.*, 2010), whether there was involvement of rutile or amphibole present in the subducted material during partial melting (Sunda arc: Residual rutile; Handley *et al.*, 2011; New Britain, Papua New Guinea: Residual amphibole; Kurzweil *et al.*, 2019 and references therein; Solomon Islands: Subducted volcanic sediment and potentially residual rutile; Schuth *et al.*, 2009). The source of Ti isotope fractionation (and the HFSE budget) can be split into two connected groups, process-induced and component-induced fractionation of Ti isotopes. The relevant processes can be narrowed down to fractional

crystallisation or partial melting in the presence of a Fe-Ti oxide, as olivine, pyroxene-group minerals and pyrope are not fractionating Ti isotopes at terrestrial fO_2 (Deng *et al.*, 2019; Millet *et al.*, 2016; Wang *et al.*, 2019). The relevant components are the subducted sediment, the depleted mantle wedge or the slab-related fluids, this is independent of the geochemical model of subduction zone melt generation. The lithophile and fluid-immobile nature of Ti and to an extent the HFSE means that its budget in arc basalts is constrained to variable contributions from partial melts produced in the overlying mantle wedge and from subducted material (sediment and oceanic crust, tectonic mélanges; *e.g.*, König *et al.*, 2010; Marschall and Schumacher, 2012). Both components should have distinct Ti isotope compositions. Mantle-derived samples and MORBs show no significant Ti isotope fractionation whereas granitic and sedimentary samples (shales) are enriched in heavy Ti isotopes (Greber *et al.*, 2017a; Millet *et al.*, 2016).

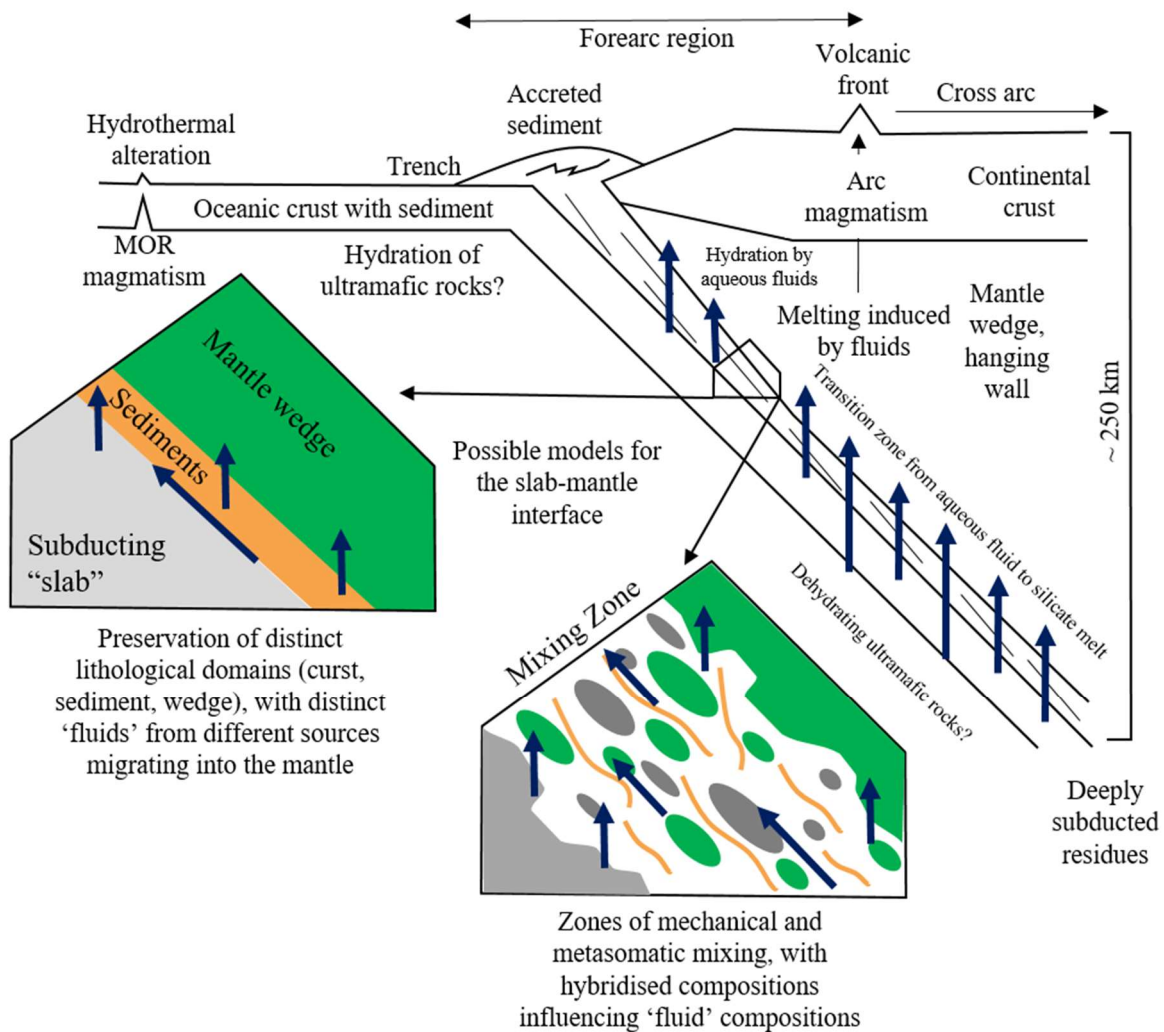


Figure 4-1: Processes at subduction zones. Schematic description of the processes taking place at subduction zone (modified from Bebout, 2014). The two wedges depict two existing models on the slab-wedge interface.

4.1.2 Titanium isotope systematics in subduction zones

Primitive magmatic lithologies and mantle-derived melts show little to no Ti isotope fractionation relative to ultramafic mantle peridotites (Millet *et al.*, 2016). However, in Ocean Island Basalts (OIB), and other more differentiated arc lithologies, samples show distinct positive correlations between $\delta^{49}\text{Ti}$ and SiO_2 , which are thought to be the result of the fractional crystallization of Fe-Ti oxides during magmatic differentiation (arc array; Deng *et al.*, 2019; Millet *et al.*, 2016). Deng *et al.* (2019) argued that in plume-related OIB magmas, owing to their lower $f\text{O}_2$ compared to arc magmas, Fe-Ti-oxide saturation is delayed, leading to their enrichment in TiO_2 during fractional crystallization of olivine and pyroxene (plume array; Deng *et al.*, 2019). This leads to higher TiO_2 contents in mantle plume-related OIB melts, allowing for larger magnitudes of Ti isotope fractionation at the eventual onset of Fe-Ti-oxide saturation (Deng *et al.*, 2019).

Titanium-rich oxides (*e.g.*, rutile and ilmenite) act as the primary hosts for TiO_2 , and owing to their resilience of weathering, are potentially enriched in subducted detrital sediments. Moreover, these phases exert a strong control on the behaviour of the HFSE (Nb, Ta, Hf, and Zr) budget during partial melting and crystallization (Plank, 2014), due to their similar charge and ionic radii compared to Ti. The presence (or absence) of these phases in subducted material may have ramifications for the Ti isotope composition of rocks originating from arc settings during partial melting. Subduction zone rocks occur at complex tectonic settings that can be influenced by a multitude of components, like the metasediments covering the subducted oceanic crust, or fluid- and melt-like components that form as a result of the dehydration and subsequent partial melting of the subducted slab. Because of its immobility in fluids, Ti is not expected to be mobilised during slab-dehydration (Kessel *et al.*, 2005). However, depending what residual phases are present during partial melting of a given subducted slab, Ti isotope variations for arc magmas with similar SiO_2 contents could occur. This chapter presents a detailed study of the Ti isotope compositions of basaltic and boninitic rocks from various subduction zone settings (Solomon Islands, Sunda Arc, New Britain and Cape Vogel in Papua New Guinea, and Cyprus). To better constrain the potential sediment component in Cyprus samples and Sunda Arc lavas, a set of drill core sediments from the vicinity of both locations was also analysed for their Ti isotope composition. Results from this chapter show that Ti isotope variations in subduction-related basalts and boninites are decoupled from slab-

dehydration fluids, but boninites are systematically more enriched in heavier Ti isotopes at similar SiO₂ content compared to arc tholeiites from the same localities. While the presented data further confirm that the key mechanism fractionating Ti isotopes are equilibria between Fe-Ti oxide and silicate melt (Millet *et al.*, 2016), the new data suggests that source processes, as well as other mineral components, may also play a role in fractionating Ti isotopes.

4.1.3 Geological background and sample selection

For this study well-characterised samples from a pre-existing dataset were selected that, in addition to extensive radiogenic isotope systematics and trace element data, includes high-precision HFSE data and, with the recent study by Kurzweil *et al.* (2019), high-precision tungsten isotope data (see *e.g.*, Fonseca *et al.*, 2017; König *et al.*, 2008, 2010; Kurzweil *et al.*, 2019; Schuth *et al.*, 2009). This will permit further identification of any source processes and components operating during petrogenesis of the different arc sample suites.

4.1.3.1 Troodos ophiolite complex (Cyprus)

With an area of ca. 3000 km², the Troodos ophiolite complex (TOC) forms the core of the island of Cyprus. It is a well preserved 90 Ma old supra-subduction zone ophiolite (Fonseca *et al.*, 2017; Marien *et al.*, 2019; Regelous *et al.*, 2014; Woelki *et al.*, 2018). Heavily serpentinised sequences of ultramafic rocks are overlain by gabbros and a sheeted dyke complex, as well as evolved tholeiitic arc andesites and dacites. These dacites are overlain by a series of more primitive pillow lavas, the so-called lower and upper pillow lava units (LPL and UPL, respectively). Whereas the LPL show extensive hydrothermal alteration, UPL samples, which comprise picrites and high-Ca boninites, are glassy and only display restricted low-temperature alteration in the form of glass devitrification and palagonitization (Fonseca *et al.* 2017). Samples from this locality include tholeiitic basalts and high-Ca boninites from the UPL. Both basalts and boninites overlap in their SiO₂ content (51.5 to 57.9 wt.%, and 53.3 to 58 wt.%, respectively), yet boninites show higher Cr and Ni concentrations and Mg# than the basalts. The UPL were emplaced in a subduction zone setting with a significant subducted sediment component (fluid or melt; Fonseca *et al.*, 2017; König *et al.*, 2008; Kurzweil *et al.*, 2019; Regelous *et al.*, 2014; Woelki *et al.*, 2018). Moreover, these samples have low Nb/Ta, and high

Nb/La, which argues for the absence of rutile and ilmenite being present in their mantle sources (König *et al.*, 2010). The clear influence of a sediment-like component in the sources of Troodos UPL samples, coupled to the absence of a residual Ti-phase in Troodos' source regions make samples from the UPL suite a valid end-member to study the influence of subducted (pelagic) sediments on the Ti isotope composition of these samples.

4.1.3.2 Solomon Islands

The Solomon Island arc is a subduction zone located in a complex tectonic setting. Two NW-SE trending island chains mark the collision zone, where the Indian-Australian and the Pacific plates collide. Active since Eocene times, this collision zone experienced a reversal of subduction polarity during the Neogene (Schuth *et al.*, 2009 and references therein). Due to the reversal of subduction polarity, young and hot oceanic crust (Woodlark basin, *ca.* 4-5 Ma old; Schuth *et al.*, 2009), covered mostly by volcanic sediments, is being subducted and is associated with arc-volcanism. Samples analysed here were the subject of various studies investigating the mobility of W and HFSE in subduction zones (König *et al.*, 2008; Schuth *et al.*, 2009). Samples analysed here have SiO₂ contents between ~ 46 and 53 wt.%. The trace element budget is dominated by volcanic sediments, as evidenced by large overlap of lead isotope compositions between volcanoclastic sediments from the North Loyalty Basin (Peate *et al.*, 1997) and magmatic samples from the Ontong Java Plateau (See Fig. 6a and b in Schuth *et al.*, 2009; Tejada *et al.*, 2004). As such, samples from this locality consist of a good end-member to investigate the potential influence of subducted volcanic sediments on the Ti isotope compositions of Solomon Island arc tholeiite samples.

4.1.3.3 Sunda Arc

Sunda is part of the Indonesian arc system, which extends from the islands of Java to Flores. Calc-alkaline volcanism on the Sunda-arc originates from flux-melting of a mantle wedge that was induced by the subduction of the Indonesian-Australian plate beneath the Eurasian plate (Handley *et al.*, 2007, 2011, 2014). Previous trace element and Hf-Nd-Pb isotope studies reveal a complex magmatic history that involves several different magma source components. The arc can be separated into West and East-Central Java. The samples from Sunda in this study have

SiO₂ contents between 45 and 58 wt.%. West Java magmatism is dominated by subducted detrital sediments and the assimilation of primitive mafic crustal rocks (low Ba/Hf at constant ²⁰⁶Pb/²⁰⁴Pb), whereas samples from East-Central Java appear to be affected by fluids derived from subducted altered oceanic crust, as well as variable amounts of subducted pelagic sediments (*e.g.*, elevated Ba/Hf at constant ²⁰⁶Pb/²⁰⁴Pb isotope compositions - cf. Handley *et al.*, 2014). Seven sediment samples from southeast of Java were included in this study (Site 261 of Deep Sea Drilling Project 27), which comprise fine-grained mudstones, carbonates and Fe-Mn-rich samples (Kurzweil *et al.*, 2019). A negative covariation between Zr/Sm and Nb/Ta suggests the presence of residual rutile during basalt petrogenesis. Partial melting in the presence of a Ti-bearing (oxide-)phase is expected to result in Ti isotope fractionation, making Sunda arc basalts a viable target to study the influence of residual Ti-oxides in the source of subduction zone magmas.

4.1.3.4 Papua New Guinea – Cape Vogel

The Papuan Ultramafic belt is an ophiolite complex that developed during a continent-island arc collision in the late Paleocene (Walker and McDougall, 1982). The allochthonous ophiolite sequence represents the early stage of island arc magmatism, that formed close to a subduction zone. Samples in this study are low-Ca boninites and tholeiitic basalts from Cape Vogel that were previously analysed for their HFSE and later for their W isotope composition (König *et al.*, 2010; Kurzweil *et al.*, 2019). Boninites show limited variation in SiO₂ content (55 to 57 wt.%) whereas basalts have slightly lower SiO₂ contents from 50 to 53 wt.%. Variations in Nb/Ta and Zr/Sm in Cape Vogel samples suggest the presence of residual amphibole at the source of the Papua New Guinea (PNG) samples (Foley *et al.*, 2002; König *et al.*, 2010). König *et al.* (2010) suggest, based on HFSE systematics, that the PNG samples represent the (depleted mantle) melt-component end-member. This possibility is further supported by coupled variations between Zr/Sm and εHf and primitive mantle (PRIMA) Gd/Yb in PNG boninites (König *et al.*, 2010). Given that Ti⁴⁺ is compatible in Ca-bearing amphiboles in similar spatial coordination as in oxides (VI-fold in oxides; Millet *et al.*, 2016; Tiepolo *et al.*, 2007 and references therein), amphibole-melt equilibria may promote Ti isotope fractionation, a possibility that remains to be tested. As such the presence of residual amphibole in PNG mantle

sources makes the Cape Vogel PNG suite attractive for determination of their Ti isotope composition.

4.1.3.5 Papua New Guinea – New Britain (Rabaul)

The Island of New Britain (Northwest of Papua New Guinea) evolved by subduction of the Solomon plate beneath the Bismarck plate, ca. 30 Ma ago (Joshima *et al.*, 1986). The samples analysed here, consist of a suite of arc-related rocks (basaltic to andesitic composition) and originate from the Tavurvur volcano. High Sr/Nd and U/Th of arc lavas from New Britain show that slab-derived fluids, enriched in Sr and U, dominate the trace element inventory. The lack of a characteristic Ti anomaly, which is found in N-MORB normalised trace element patterns of sediments from Solomon Plate, but cannot be seen in the analysed lavas, supports the notion that a residual Ti-bearing oxide phase was of negligible importance in the petrogenesis of these rocks (Woodhead *et al.*, 1998). Samples from Neogene eruptions analysed in this study were analysed for their trace element contents and Sr-Pb-Nd and W isotope compositions in studies by König *et al.*, (2011) and Kurzweil *et al.*, (2019). Samples from the Rabaul are from the inner caldera (n = 3) and the outer caldera (n = 7). The SiO₂ content of these samples varies between ~ 50 and 68 wt.%. Hohl *et al.*, (under review) argued that fractional crystallisation of magnetite and amphibole play significant roles in the petrogenesis of these rocks, based on characteristic trace element variations in Zr/Sm and Nb/La. Given that both phases could affect the behaviour of Ti and its isotopes, this makes the Rabaul sample suite quite attractive to investigate its Ti isotope evolution during partial melting or fractional crystallisation of magnetite and amphibole.

4.2 Methods

4.2.1 Sample digestion and column chemistry

A detailed description of the chemical separation procedure can be found in the study by Kommescher *et al.*, (2020). Analytical grade concentrated acids (p.a. grade, Merck, 24 M HF, 14 M HNO₃ and 10 M HCl) are purified in Savillex DST-1000 sub-boiling distils. All chemical

reagents (HCl, HF, HNO₃, and H₂O₂) were regularly checked for blank concentrations. All dilutions were prepared with Merck Milli-Q 18.2 MΩ water. Typical Ti concentrations in used reagents were in the sub ng/mL range. Powdered samples were weighed in Savillex beakers with the goal of having at least 30 μg of sample Ti. Consequently, blank contribution from chemical reagents was negligible for Ti isotope analysis. All beakers and ICP-MS test tubes (4 mL and 12 mL) were thoroughly cleaned prior to use. The ⁴⁹Ti/⁴⁷Ti double spike was added in the ideal sample/spike ratio, which was calculated using the double spike toolbox (sample/spike = 0.51:0.49; Rudge *et al.*, 2009; see Kommescher *et al.* (2020), for double-spike calibration). Concentrated and distilled acids were then mixed in a 3:1 proportion (14 M HNO₃ : 24 M HF; 4 mL total) for digestion. The beakers were closed and placed on a hotplate at 120 °C for 48 hours. Samples were then dried down and refluxed in conc. HNO₃ >> 0.5 M HCl : 0.5 M HF to prevent fluoride formation. After the samples dried, they were refluxed in 6M HCl – 0.06M HF to convert the sample into Chloride form, and afterwards taken up in 1 mL of 1 M HCl – 2 % H₂O₂ for column chemistry. In most cases, complete dissolution was achieved, and only three samples from PNG showed a small black mineral residue (2 -3 grains, <0.25 mm large). Whether or not these refractory phases are Ti-rich was tested after data-reduction, by checking whether the measured sample/spike ratio was shifted towards the spike. Such a shift is not observed, and samples remained always near the optimal sample:spike ratio throughout the chemistry. Samples were loaded onto pre-cleaned and conditioned columns in 1 M HCl – 2 % H₂O₂. Titanium was purified using a five step chemistry modified after Münker *et al.*, (2001), see also Kommescher *et al.*, (2020). Each run of samples included at least one terrestrial (JB-2, BCR-2 or BHVO-2) or synthetic (OL-Ti, Col-Ti) reference material, or in some cases both. For matrix-free synthetic reference materials the first chemistry step had to be modified, because in the absence of matrix from that Ti could be separated, Ti was adsorbed onto the resin instead of being eluted. As such, processing of these chemical reference materials required slightly higher acid strength so that Ti could be eluted (1.75 M HCl – 2 % H₂O₂ instead of 1 M HCl – 2 % H₂O₂). After column chemistry, samples were dried down and refluxed in 6 M HNO₃ – 0.1 M HF and H₂O₂ in a 9:1 mixture to remove remaining organic phases derived from the resin. After drying, samples were taken up in 0.045 M HNO₃ – 0.005 M HF prepared for measurement of their Ti isotope composition by MC-ICP-MS.

4.2.2 MC-ICP-MS measurements

Samples were measured in the clean-lab facility of the University of Cologne using a Neptune Plus MC-ICP-MS. Samples were introduced into the instrument with an APEX HF desolvating system, additional Ar and N₂ gas, and an extra glassware (cyclonic/Scott hybrid spray chamber) between APEX and injector for enhanced stability. The instrument was fitted with Ni sample and Ni (H) skimmer cones. Lens and gas settings were adjusted daily and resolution power (5 – 95% peak definition, $\Delta M/M$) was in the range of $\sim 10,000$ (high-resolution mode). At the beginning, middle and end of each sequence multiple spiked aliquots of OL-Ti and a synthetic in-house reference material Col-Ti were measured to control for long-term drift and to account for possible, unresolved polybaric interferences. In addition to chemical reference materials, each sequence contained at least one spiked and chemically processed terrestrial reference material, which was measured before and/or after each sample to gauge intermediate precision (external reproducibility). Sample solutions contained at least 1 $\mu\text{g/mL}$ of Ti at intensities of ca. 2.5, 3.5 and 2.5 $\times 10^{-11}$ A for ⁴⁷Ti, ⁴⁸Ti and ⁴⁹Ti, respectively. The pure analysis solutions (on peak zero) gave background intensities that were a factor of 1,000 lower, ca. 1, 2 and 1 $\times 10^{-14}$ A for ⁴⁷Ti, ⁴⁸Ti and ⁴⁹Ti, respectively. Measured signals were recorded with 10¹¹ Ω amplifiers. Samples were measured, in 60 cycles with 8 seconds integration time, at least four times to account for outliers and constrain internal precision. Data were reduced offline using an iterative method described by Compston and Oversby (1969) and improved by Heuser *et al.*, (2002) and Schönberg *et al.*, (2008).

4.3 Results

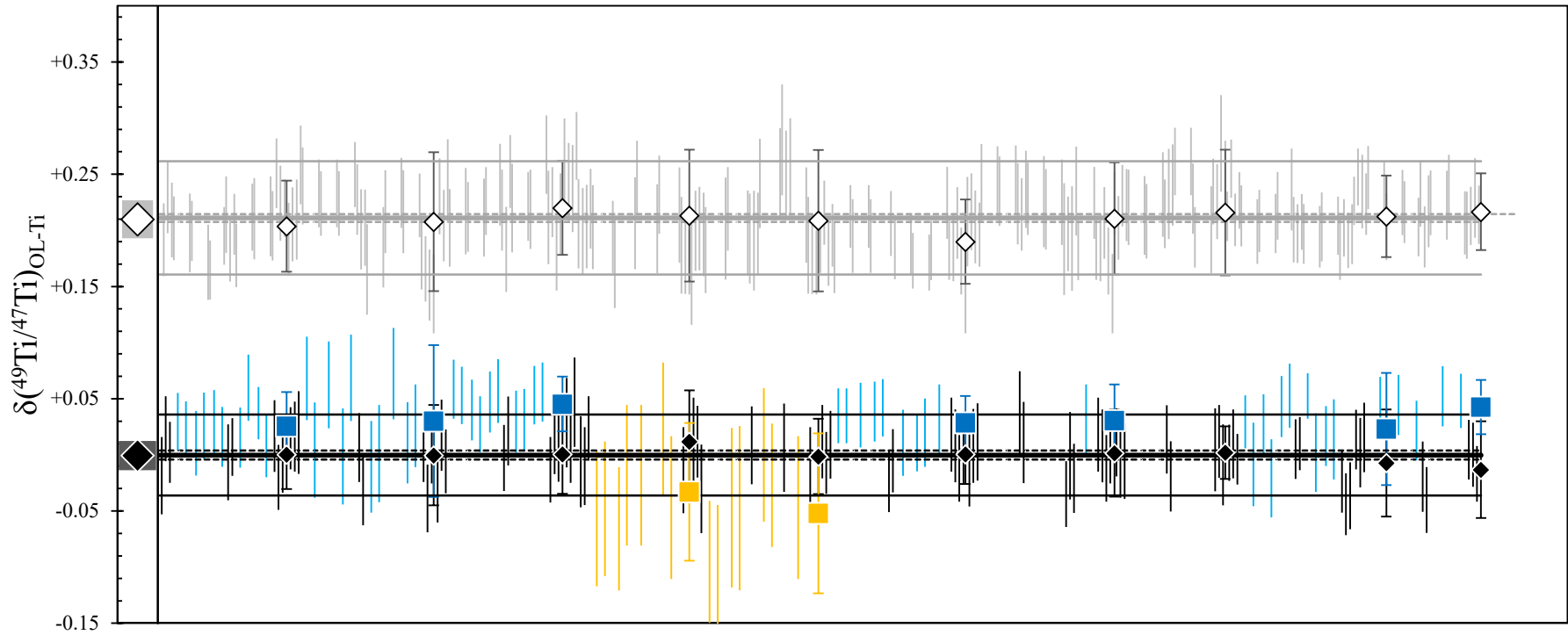
All results are given as the deviation of the ⁴⁹Ti/⁴⁷Ti ratio of the sample relative to the Origins-Lab OL-Ti reference material in permil (Millet *et al.*, 2016; Millet and Dauphas, 2014): $\delta(^{49}\text{Ti}/^{47}\text{Ti})_{\text{OL-Ti}} = (^{49}\text{Ti}/^{47}\text{Ti}_{\text{sample}}/^{49}\text{Ti}/^{47}\text{Ti}_{\text{OL-Ti}} - 1) \times 1000$ (henceforth $\delta^{49}\text{Ti}$). The Ti isotope composition for each sample is shown in Table 4-1, additional trace element data used in this study is compiled in the appendix. All samples show negligible deviations from the predicted ⁴⁹Ti/⁴⁷Ti_{mixed} ratio, meaning that all significant Ti-phases were digested. The synthetic reference materials, Col-Ti and OL-Ti, were measured 217 and 86 times, respectively, over a course of ten sessions.

Table 4-1: Ti isotope compositions of subduction zone derived samples and related sediments

Sample ID	Sample type	$\delta(^{49}\text{Ti}/^{47}\text{Ti})_{\text{OL-Ti}}$	2 s	n	95% c.i.
OL-Ti		0.000	0.013	10	0.004
Col-Ti		0.209	0.017	10	0.006
JB-2		-0.043	0.027	2	0.121
BHVO-2		0.031	0.015	8	0.006
<i>Cyprus Basalts</i>					
CY-1	Basalt	0.090	0.010	4	0.008
CY-4b	Basalt	0.070	0.013	4	0.010
CY-A	Basalt	0.045	0.010	4	0.008
CY-D	Basalt	0.087	0.011	4	0.009
ZY-61	Basalt	0.076	0.019	4	0.015
CY 15	Basalt	0.063	0.024	4	0.019
CY 45	Basalt	0.102	0.027	4	0.021
CY 12	Basalt	0.107	0.018	4	0.014
CY 31	Basalt	0.033	0.046	4	0.037
CY 33	Basalt	0.149	0.035	4	0.028
CY 34	Boninite	0.168	0.032	4	0.025
CY 36	Boninite	0.146	0.045	4	0.036
CY 39	Boninite	0.166	0.014	4	0.011
CY-4b	Boninite	0.077	0.029	4	0.023
Cy1	Basalt	0.10	0.27	1	0.035
Cy4	Basalt	0.03	0.37	1	0.048
Cy61	Basalt	0.06	0.25	1	0.033
Cy62	Basalt	0.10	0.26	1	0.034
cy63c	Basalt	0.09	0.27	1	0.035
<i>Papua New Guinea - Cape Vogel</i>					
PNG 1	Boninite	0.114	0.016	4	0.012
PNG 8	Boninite	0.133	0.040	4	0.032
PNG 10	Boninite	0.143	0.045	4	0.036
PNG 12	Boninite	0.112	0.031	4	0.024
PNG 14	Boninite	0.136	0.071	4	0.056
PNG 25	Boninite	0.109	0.045	4	0.036
PNG 27	Boninite	0.123	0.030	4	0.024
PNG 62	Basalt	0.035	0.016	3	0.020
PNG54	Basalt	0.11	0.28	1	0.036
PNG59	Basalt	-0.03	0.31	1	0.040
PNG63	Basalt	0.03	0.23	1	0.030
<i>Sunda Arc</i>					
I2Kr2	basalt. Andesit	0.105	0.028	4	0.022
I4Sm1	Basalt	0.045	0.017	4	0.013
I12Mu2	Absarokit	0.067	0.017	4	0.013
I29Ag2	basalt. Andesit	0.125	0.016	4	0.013
I32Ri3	Basalt	-0.008	0.010	4	0.008
I3 Ga1	Basalt	0.023	0.024	4	0.019
I 25Pe1	basalt. Andesit	0.082	0.025	4	0.020
I16Mu6	Absarokit	0.276	0.026	4	0.020

CHAPTER 4 - TITANIUM ISOTOPE VARIATIONS IN SUBDUCTION ZONE DERIVED ROCKS

<i>Solomon Islands</i>						
S 3	Basalt	0.036	0.060	5	0.037	
S 18	Basalt	0.042	0.032	4	0.026	
S E 15	Basalt	0.095	0.029	4	0.023	
S 153 Mbo	Basalt	0.039	0.031	4	0.024	
S 187 Van	Basalt	0.045	0.026	4	0.021	
S 207 Tin	Basalt	0.051	0.036	4	0.028	
S 217 SC	bas. Andesite	0.070	0.012	4	0.009	
S 220 SC	bas. Andesite	0.034	0.031	4	0.024	
<i>New Britain</i>						
SHR5	trachytic andesite	0.275	0.014	5	0.009	
SHR9	andesite	0.215	0.012	5	0.007	
SHR13	trachytic andesite	0.241	0.029	5	0.018	
SHR31	basaltic andesite	0.269	0.012	5	0.007	
SHR32	dacite, trachytic andesite	0.373	0.010	5	0.006	
SHR24	basaltic andesite	0.264	0.022	5	0.014	
SHR26	andesite	0.132	0.028	5	0.017	
SHR14	basalt	-0.0128	0.0068	4	0.005	
SHR16	basalt	-0.022	0.023	4	0.018	
SHR22	andesite	0.079	0.032	4	0.025	
<i>Sunda arc sediments</i>						
DSDP 27-261-2-2-11.92m	Mudstone	0.616	0.122	4	0.097	
DSDP 27-261-3-3-51.33m	Carbonate	0.227	0.021	4	0.017	
DSDP 27-261-5-1-162.48m	Mn-oxid-rich muds	0.6097	0.0075	4	0.006	
DSDP 27-261-6-1-177.41m	Mudstone	0.5468	0.0085	4	0.007	
DSDP 27-261-9-3-202.95m	Mudstone	0.246	0.067	4	0.054	
DSDP 27-261-22-2-344.31m	Sandstone	0.206	0.037	4	0.030	
DSDP 27-261-28-2-448.42m	Carbonate	0.475	0.029	4	0.023	
<i>Mediterranean sediments</i>						
DSDP-13-127-2-5-140/141cm	Graded sands; marl oozes	0.185	0.015	4	0.012	
DSDP-13-128-6-3-50/52cm	Graded silt/sand	0.193	0.013	4	0.011	
DSDP-13-127-18-1-100/102cm	Limestone	0.160	0.024	4	0.019	
ODP-160-970-A-9X-1-32/34cm	Clust-rich mud; debris flow	0.008	0.033	4	0.026	
ODP-160-970-A-16X-2-44/46cm	Clust-rich mud; debris flow	0.224	0.050	4	0.040	



$\delta^{49}\text{Ti}$ ColTi average: $+0.211 \pm 0.050$ ‰ 2 s., n = 211
 $\delta^{49}\text{Ti}$ ColTi sessions: $+0.210 \pm 0.017$ ‰ 2 s., n = 10
 $\delta^{49}\text{Ti}$ ColTi sessions: $+0.210 \pm 0.006$ ‰ 95% c.i., n = 10

$\delta^{49}\text{Ti}$ OL-Ti average: $+0.000 \pm 0.036$ ‰ 2 s., n = 82
 $\delta^{49}\text{Ti}$ OL-Ti sessions: $+0.000 \pm 0.019$ ‰ 2 s., n = 10
 $\delta^{49}\text{Ti}$ OL-Ti sessions: $+0.000 \pm 0.002$ ‰ 95% c.i., n = 10

$\delta^{49}\text{Ti}$ JB-2 average: -0.043 ± 0.067 ‰ 2 s., n = 14
 $\delta^{49}\text{Ti}$ JB-2 sessions: -0.043 ± 0.027 ‰ 2 s., n = 2
 $\delta^{49}\text{Ti}$ JB-2 sessions: -0.043 ± 0.121 ‰ 95% c.i., n = 2

$\delta^{49}\text{Ti}$ BHVO-2 average: $+0.031 \pm 0.043$ ‰ 2 s., n = 55
 $\delta^{49}\text{Ti}$ BHVO-2 sessions: $+0.031 \pm 0.017$ ‰ 2 s., n = 7
 $\delta^{49}\text{Ti}$ BHVO-2 sessions: $+0.031 \pm 0.008$ ‰ 95% c.i., n = 7

◇ Col-Ti
 ◆ OL-Ti
 ■ BHVO2
 ■ JB2

Figure 4-2: Intermediate precision of the analysed reference materials. Each line represents one measurement (± 2 s.). Symbols to the left represent average Col-Ti and OL-Ti (± 2 s) over the course of all sequences.

The twofold standard deviation (henceforth “2 s” following IUPAC guidelines) for Col-Ti and OL-Ti is below ± 0.020 ‰, which corresponds to a 95% c.i. of ± 0.006 ‰ and ± 0.004 ‰, for ten sequences ($n = 10$), respectively. Terrestrial reference materials JB-2 and BHVO-2 accurately reproduce published values with -0.043 ± 0.027 ‰, and $+0.031 \pm 0.015$ ‰ (2 s), respectively. BHVO-2 was measured in all ten sessions, whereas JB-2 was measured in two sessions (Figure 4-2). Titanium isotope compositions of tholeiitic basalts Troodos UPL suite (UPL) range between $+0.033$ ‰ and $+0.102$ ‰ and boninites from Troodos UPL suite vary between $+0.146$ and $+0.168$, respectively. Drill core sediments from the Mediterranean Sea, offshore the island of Cyprus were also measured for their $\delta^{49}\text{Ti}$ and range between $+0.008$ and $+0.193$ ‰. Basaltic samples from the Solomon Islands suite exhibit $\delta^{49}\text{Ti}$ between $+0.026$ and $+0.095$ ‰. Sunda arc samples display $\delta^{49}\text{Ti}$ between -0.008 and $+0.276$ ‰. Drill core sediment samples from the proximity of the Sunda arc display Ti isotope variations between $+0.206$ and $+0.616$ ‰. Tholeiitic basalts from Cape Vogel range between -0.027 and $+0.110$ whereas boninites range between $+0.109$ and $+0.143$ ‰. Samples from New Britain have $\delta^{49}\text{Ti}$ between -0.02 and $+0.37$ ‰, with the three samples from the outer caldera having the lowest $\delta^{49}\text{Ti}$ in this sample suite (-0.02 to $+0.08$ ‰).

4.4 Discussion

When all magmatic samples are taken together, they show a broad correlation between $\delta^{49}\text{Ti}$ and their SiO_2 , in similar fashion to what has been previously observed (Figure 4-3; Deng *et al.*, 2019; Greber *et al.*, 2017a; Millet *et al.*, 2016), and follow the overall trend defined by arc samples worldwide (Deng *et al.*, 2019). However, there appear to be some exceptions. For example, three samples plot well outside the arc-array, two Rabaul- and one Sunda-sample, which show higher $\delta^{49}\text{Ti}$ than any other samples at similar SiO_2 contents (ca. 52 wt.%), and seemingly fall in the plume-array defined in Deng *et al.*, (2019). Cyprus UPL and Papua New Guinea boninites and boninitic basalts show systematically higher $\delta^{49}\text{Ti}$ than their respective tholeiitic samples. While PNG boninites show constant $\delta^{49}\text{Ti}$ of $+0.10$ to 0.14 ‰ for MgO-contents of 10 to ~ 23 wt. %, and Sunda and Rabaul show a covariation of $\delta^{49}\text{Ti}$ with FeO (and MgO)-content, the remaining samples show no observable covariation for MgO, TiO_2 or FeO. Rabaul samples show a negative correlation between their MgO their contents and $\delta^{49}\text{Ti}$ values

from 6 wt.% and +0.27 ‰ to ~ 3 wt.% and +0.13 ‰, respectively, followed by an increase in $\delta^{49}\text{Ti}$ with decreasing MgO from ~3 wt.% and +0.13 ‰ to 1.24 wt.% and +0.37 ‰.

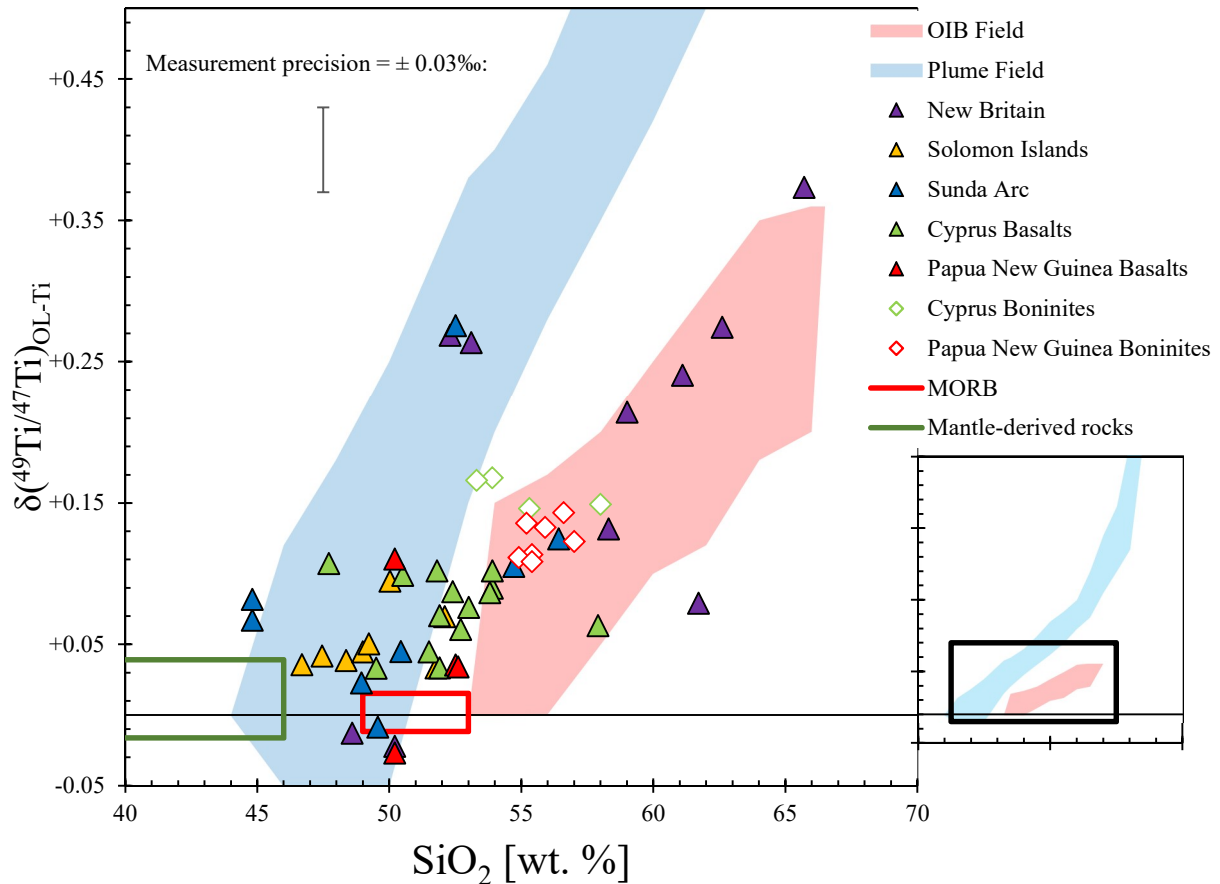


Figure 4-3: Ti isotope composition of analysed samples relative to SiO_2 . Shaded fields and boxes constrained by previous studies (Millet *et al.* 2016, Deng *et al.* 2019), green and red boxes illustrate the range of analysed mantle derived and MORB samples, respectively (Millet *et al.* 2016). The right, small diagram shows a zoom-out view of the Ti isotope composition vs. SiO_2 arrays (Millet *et al.* 2016, Deng *et al.* 2019).

4.4.1 General remarks on coupled $\delta^{49}\text{Ti}$ – (trace) element systematics

As stated earlier, the samples depicted here have been well characterised trace element and radiogenic and stable isotope systematics (Fonseca *et al.*, 2017; Kirchenbaur *et al.*, 2012; Kirchenbaur and Münker, 2015; König *et al.*, 2008, 2010, 2011; Kurzweil *et al.*, 2019; Schuth *et al.*, 2009). In this discussion, the Ti isotope data for these samples will be combined with these previous geochemical data, to investigate how the presence or absence of residual phases in the sub-arc mantle, and/or the involvement of subduction components (fluids, slab melts, etc.) may affect the Ti isotopic composition of arc magmas. For example, the HFSE (Nb, Ta.,

Zr, Hf) group is linked to subducted sediments, because they can be enriched in detrital phases (Ti-bearing oxides) and to a certain degree in Ca-amphiboles (Klemme *et al.*, 2005; Kurzweil *et al.*, 2019; Plank, 2014; Tiepolo *et al.*, 2007). As the HFSE and Ti isotope composition are sensitive to the crystallisation of Ti-bearing oxide phases (Schuth *et al.*, 2009 and references therein), a study that combines the Ti isotope composition, HFSE systematics, as well as other relevant trace elements such as W (for fluid mobility) and Th (contribution from a hydrous sediment melt), may provide deeper insights into the Ti isotope systematics in subduction-related samples than just the co-variation between $\delta^{49}\text{Ti}$ and SiO_2 alone. If, for example, a ratio like Nb/Ta shows a positive correlation with $\delta^{49}\text{Ti}$, this suggests the preferential retention of Ta over Nb, and that of light Ti isotopes over heavier ones, in the source during partial melting in the presence of Fe-Ti bearing oxides. The silicate melt that results from this process will then have subsequently higher $\delta^{49}\text{Ti}$ and Nb/Ta than its mantle source. This is expected since the oxide-melt fractionation factor $\Delta^{49}\text{Ti}_{\text{oxide-melt}}$ is typically between -0.2 and -0.4 ‰ (Johnson *et al.*, 2019; Millet *et al.*, 2016), rutile/melt partition coefficients (Klemme *et al.*, 2005) for Ta are higher than those for Nb. On the other hand, highly incompatible but fluid-immobile elements are expected to be enriched in hydrous sediment melts, which can either mix with primitive arc magmas, or re-fertilise a mantle wedge that has been depleted due to prior melt extraction. Conversely, arc magmas that have mixed with slab-derived fluids would be expected to be enriched in elements like W (König *et al.* 2008). If the trace element budget and $\delta^{49}\text{Ti}$ of a subduction zone setting is heavily dominated by hydrous sediments melts, then this should result in a correlation between the abundances and ratios involving fluid-immobile elements like Th (Ba/Th, W/Th, etc.) with $\delta^{49}\text{Ti}$. Moreover, the observation that Ti shows limited fluid mobility (Kessel *et al.*, 2005) makes it unlikely that subduction fluids may influence the Ti isotope composition of arc magmas. As such, the subduction end-members that may impart unto arc magmas any variability in their Ti isotope composition consist of subducted metasediments (*e.g.*, as in Cyprus and the Solomon Islands), partial melts that reflect the Ti isotopic characteristics of the mantle wedge (Cape Vogel, Papua New Guinea and Sunda), and of course primary processes like the partial melting in the presence of Fe-Ti oxides and fractional crystallisation of Fe-Ti oxides (Sunda and potentially Papua New Guinea and the Solomon Islands).

4.4.2 Can the recycling of subducted sediments affect the Ti isotope composition of arc lithologies? – Cyprus, Solomon Islands

Larger contributions from sediment-derived melts or fluids are usually coupled with incompatible element enrichment (*e.g.*, König *et al.*, 2011; Plank, 2014). If significant amounts of Ti oxides are present in the sediment, this should be reflected by a low value of $\delta^{49}\text{Ti}$ in the bulk sediment, as its Ti budget is controlled by its oxide content. In case of partial melting, this component would impart a positive $\delta^{49}\text{Ti}$ onto the resulting silicate melt as long as it remains a residual phase. However, if the sediment is comprised mostly of eroded felsic minerals, it should exhibit positive $\delta^{49}\text{Ti}$, similar to that of shales and granitic samples ($\delta^{49}\text{Ti}$ of up to +0.6 ‰; Greber *et al.*, 2017a; Millet *et al.*, 2016). Based on a mass balance model, Kurzweil *et al.*, (2019 electronic supplements) estimated that in order to account for the elevated W/Th in the Troodos' UPL samples, nearly 70% of total W need to be derived from a subducted sediment component, regardless of whether it consists of a fluid or a melt. This observation is echoed by Fonseca *et al.*, (2017) who estimated that ca. 10% of a hydrous sediment melt must have been mixed with a primitive arc magma in order to reproduce the range in B, Nd, Pb and Sr isotope compositions of UPL tholeiites and boninites. Therefore, it could be entirely possible that the slightly elevated $\delta^{49}\text{Ti}$ of UPL tholeiites and boninites is inherited from this putative sediment-like component, which would necessarily have to consist of a melt given the fluid immobile nature of Ti (Kessel *et al.*, 2005). Indeed, the eastern Mediterranean sediments analysed here have $\delta^{49}\text{Ti} \sim +0.2$ ‰ and an average $^{87}\text{Sr}/^{86}\text{Sr}$ of 0.7085 (Klaver *et al.*, 2015), and mixing between primitive arc magmas and partial melts from these sediments could potentially account for the more radiogenic Sr and heavier Ti isotope composition of the UPL suite (see Figure 4-4 a). An issue with this hypothesis is that Mediterranean sediments are as TiO_2 -poor as the bulk of the UPL suite, and Ti is generally compatible during partial melting of metasediments (Hermann and Rubatto, 2009; Skora and Blundy, 2010), meaning that any sediment melt will be depleted in TiO_2 when compared to a primitive arc magma. Given that fewer than 10 % of hydrous sediment melts mixed with Troodos parental magmas (Fonseca *et al.*, 2017), there would be insufficient Ti present in the sediment melt to drive the $\delta^{49}\text{Ti}$ of the Troodos suite to its maximum value of +0.15‰ (as seen in the boninites). As such, this process cannot explain the range in $\delta^{49}\text{Ti}$ of the UPL suite. This assessment is reinforced by the conclusions of König *et al.*, (2010) who argued for the absence of Ti-rich phases like rutile and ilmenite during boninite petrogenesis in UPL sources, as evidenced by their low Nb/Ta. The presence of either

rutile and ilmenite during sediment melting would have resulted in elevated Nb/Ta ratios (Klemme *et al.*, 2005, 2006b) in the hydrous sediment melt, which is not seen in the UPL suite (König *et al.*, 2010). As such, the elevated $\delta^{49}\text{Ti}$ probably represents the Ti isotope composition of the UPL suite's depleted mantle sources, and is not the result of mixing between sediment melts and primitive arc magmas.

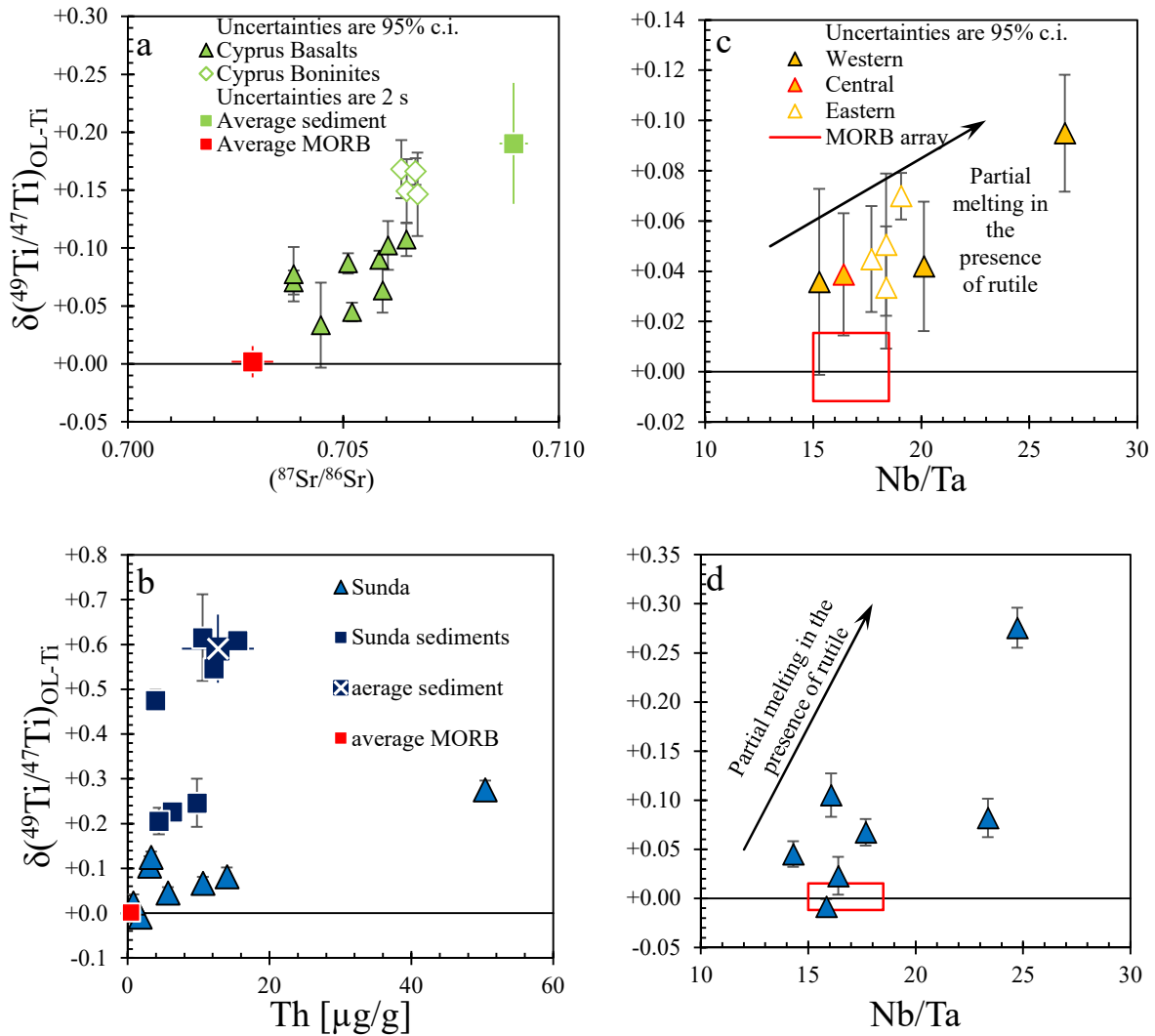


Figure 4-4 a - d: Ti isotope composition vs. trace element ratios. (a and b) $\delta^{49}\text{Ti}$ vs. $^{87}\text{Sr}/^{86}\text{Sr}$ for Cyprus UPL and $\delta^{49}\text{Ti}$ vs. Th content for Sunda arc samples illustrating the putative mixing array between MORB and sediments, or lack thereof. Sr isotope data for Mediterranean sediments from Klaver *et al.*, (2015), average Sr from MORB by White and Klein (2014) and Ti isotope composition of average MORB by Millet *et al.*, (2016). Solomon Islands samples (c) and Sunda arc samples (d) showing the potential effect of rutile in $\delta^{49}\text{Ti}$ vs. Nb/Ta. Trends in c and d are based on observed fractionation behaviour of Ti and partition coefficients from Klemme *et al.*, (2005). Symbols are the same in 4b and 4d (Sunda arc samples).

Volcanic samples from the Solomon Island Arc are a clearer example of recycling of subduction components (*i.e.*, sediment melts). Solomon Island picrites and tholeiites show enrichments in the fluid-immobile Th (up to 2.2 $\mu\text{g/g}$) and show highly variable Zr/Nb (13 to 73), a ratio that

is a measure of source depletion or refertilisation. Both features, when taken together, argue for the involvement of sediment melts in the sources of the Solomon sample suite. This view is reinforced by the large overlap between the lead isotope compositions of volcanoclastic sediments, and those displayed by picrites and basalts from the Solomon arc (See Fig. 6a and b in Schuth *et al.*, 2009; Tejada *et al.*, 2004). Moreover, distinct low Nb/Ta and Zr/Hf in BSE-normalized trace element patterns argue for the presence of Ti-bearing oxides in the sources of the Solomon Islands basalts. As stated earlier, Ta is more compatible than Nb in phases like rutile and ilmenite (Klemme *et al.*, 2005, 2006b). If these phases are present during partial melting of a Solomon Island mantle wedge that has been refertilised by sediment melts, the resulting magma would have elevated Nb/Ta and higher $\delta^{49}\text{Ti}$. Indeed, this expectation is borne by the positive correlation between Nb/Ta and $\delta^{49}\text{Ti}$ (Figure 4-4 c), which is consistent with the putative presence of residual Fe-Ti oxides, most probably rutile (König *et al.*, 2008), in the source of magmas from the Solomon Islands. As such, the Ti isotope composition of the Solomon Island suite is likely the product of partial melting of a depleted mantle source that was refertilised by a sediment melt, which carried a heavier Ti isotope signature due to the presence of rutile in the subducted metasediment.

4.4.3 Fluids and residual mineral phases – rutile, Sunda arc samples

Kurzweil *et al.*, (2019) determine W isotope compositions on sediments in proximity to the Sunda arc, which due to their heavy W isotope composition cannot account for the light W isotope composition in Sunda arc samples. The contribution of the subducted sediments to the W budget in Sunda arc magmas is too small to influence their stable W isotope composition. Following Kurzweil *et al.*, (2019), and in order to verify whether these sediments influence the Ti isotope composition of Sunda arc samples, sediments from the Sunda arc region were analysed for their $\delta^{49}\text{Ti}$, which vary between +0.2 and +0.6 ‰. As stated above, Ti is generally compatible in the metasediment during partial melting (Hermann and Rubatto, 2009). The TiO_2 content in the analysed Sunda arc samples and sediments is in the same range (1 ± 0.5 wt.%). In the absence of a Ti-bearing oxide, Ti isotopes are not known to be fractionated by silicate minerals (Johnson *et al.*, 2019; Wang *et al.*, 2019). The involvement of a hydrous sediment melt in the petrogenesis of Sunda arc samples should result in a higher $\delta^{49}\text{Ti}$ in the Sunda sample suite, which is not observed. Furthermore, if the $\delta^{49}\text{Ti}$ of Sunda arc samples are indeed related

to a hydrous sediment melt, then a covariation between $\delta^{49}\text{Ti}$ and for instance their Th content, would be expected (Figure 4-4 b). During partial melting of hydrous sediments (and in the absence of monazite), Th is highly incompatible (Skora and Blundy, 2010), and as such, even small amounts of hydrous sediment-derived melt mixed in with Sunda parental magma would overwhelm the Th budget of the magma. This may explain the high Th contents and higher $\delta^{49}\text{Ti}$ of two of the samples (I2Kr2, Krakatau with a $\delta^{49}\text{Ti}$ and a Th concentration of $+0.105 \pm 0.022$ ‰ and $3.1 \mu\text{g/g}$ and I29Ag2 Agung with a $\delta^{49}\text{Ti}$ 0.125 ± 0.013 ‰ and $3.3 \mu\text{g/g}$, respectively). However, mass balance calculations further show that, either the modelled Th concentration in the melt mixture would be too low (due to higher degrees of partial melting required to fit the mixture to the observed $\delta^{49}\text{Ti}$ and TiO_2 content of around 0.10 ‰ and $1 \text{ wt.}\%$ TiO_2), or the Ti isotope composition would be too light (due to less than 10 % of partial melting degree and thus little contribution from sediment derived Ti into the melt mixture, Figure 4-4 b). Consequently, unlike the UPL and Solomon Islands sample suites, sediment recycling can be excluded as a potential cause for the range of $\delta^{49}\text{Ti}$ displayed by samples from the Sunda suite.

Even though, sediment melts can be excluded to have influenced the Ti isotope composition of the Sunda suite, there is evidence for the involvement of residual phases, like rutile, which are known to control Ti isotope fractionation. König *et al.*, (2010) have concluded, based on HFSE systematics, that there may be residual rutile present in the mantle source of Sunda arc basalts. This view is reinforced by the observation that samples from the Sunda suite display lower $\delta^{186}\text{W}$ and lower Zr/Hf ratios when compared to MORB, which is best explained by the presence of residual rutile in their mantle sources (Kurzweil *et al.*, 2019). While the W isotope compositions of Sunda samples can be explained by partial melting of the Sunda mantle wedge, due to its overprint by a W-rich and isotopically light fluid introduced W (Kurzweil *et al.*, 2019), such a process would not result in Ti isotope fractionation. It is far more likely that the range seen in the $\delta^{49}\text{Ti}$ of the Sunda sample suite is related to the involvement of rutile. For example, the sample with the highest $\delta^{49}\text{Ti}$ (I16Mu6; from the volcano of Muria, the furthest away from the Sunda arc trench), is also the melt that originated at greater depth (Kurzweil *et al.*, 2019), depths at which rutile is stable (pressures $> 1.5 \text{ GPa}$ and temperatures $< 1150 \text{ }^\circ\text{C}$; Green and Pearson, 1986). However, the reported heterogeneity in the subducted material and the depth of origin of Sunda parental magmas may obscure this trend (Kurzweil *et al.*, 2019). Nevertheless, the positive correlations between Nb/Ta (Figure 4-4 d) and Zr/Hf with $\delta^{49}\text{Ti}$ are

best explained by the presence of rutile in Sunda sources, and illustrates the importance of residual phases on the Ti isotope composition in subduction zone samples.

4.4.4 Residual phases – amphibole, Papua New Guinea

Low Nb/La and variations Zr/Sm in tholeiitic basalts from Cape Vogel and New Britain suggest the involvement of fluids or melts that were produced in the presence of amphibole in the sources of these basalts (Foley *et al.*, 2002; Ionov and Hofmann, 1995). Samples from New Britain (inner caldera) show negative Nb/Ta anomalies but not in Zr/Hf, and generally show very little variation in PRIMA-normalised trace element compositions, with the exception of one single sample, Sample SHR5 (inner caldera), which shows significant enrichment in incompatible trace elements (see Figure 4-5). New Britain Lavas further show positive trace element co-variations in Ti/Sc and Cr/Sc with SiO₂, which can be explained by fractional crystallisation of magnetite.

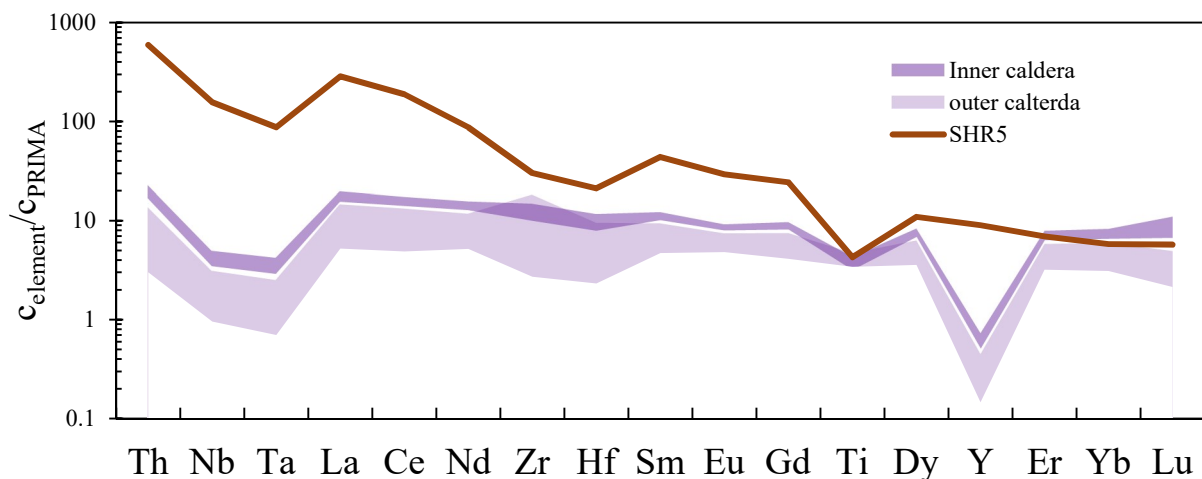


Figure 4-5: PRIMA-normalised trace element pattern for the New Britain sample suite.

The onset of either magnetite or amphibole fractional crystallisation during differentiation should be identifiable in the relationship between Ti/Sc and SiO₂, as Ti is more compatible in magnetite than Sc (Nielsen, 1992), whereas in amphibole the opposite is true (Tiepolo *et al.*, 2007). As a result, fractional crystallisation of magnetite would result in lower Ti/Sc whereas amphibole crystallisation will increase Ti/Sc in silicate melt. Considering the fact that Ti is also

compatible in magnetite, the elevated $\delta^{49}\text{Ti}$ in the Cape Vogel samples (between +0.1 and +0.4 ‰) may also result from magnetite crystallisation (Toplis and Corgne, 2002). New Britain inner caldera samples show two distinct groups in Ti/Sc vs. SiO_2 space: 1) in samples with SiO_2 between 50 wt.% and 60 wt.% show a slightly negative co-variation with Ti/Sc, which reaches a minimum value of 190 (from 230 at 50 wt.% SiO_2); 2) samples with SiO_2 contents exceeding 60 wt.%, Ti/Sc steadily increases until it reaches a maximum value of 500. This means that for New Britain samples with SiO_2 contents higher than 60 wt.%, the bulk mineral-melt partition coefficient for Sc is larger than for Ti during crystallization, as the Ti/Sc of the melt increases. This is somewhat unexpected, as Ti is more compatible in magnetite than Sc (Nielsen, 1992). Fractional crystallisation of magnetite would result in a decrease in the Ti/Sc of the silicate melt as it differentiated (*i.e.*, with increasing SiO_2 content), but the opposite appears to be true (Figure 4-6 a). Given the evidence for limited fractional crystallisation of magnetite in the New Britain suite, and since Ti can also be compatible in amphibole, it may as well be possible that the Ti isotope composition of these samples is instead related to amphibole crystallization, which merits further examination.

In order to constrain the effect of fractional crystallisation of amphibole on the trace element inventory of a given sample set, ratios between mid- and heavy rare earth elements (and incompatible elements) are often used as an indicator. For example, ratios like Zr/Sm and Nb/La ratios decrease in the melt as a result of amphibole crystallization (Foley *et al.*, 2002; Ionov and Hofmann, 1995). Indeed, the samples show a negative covariation between Zr/Sm and Nb/La, which in turn both show a negative Zr/Sm and a positive Nb/La covariation with Ti/Sc. The positive correlation of Ti/Sc and Nb/La is most likely due to simultaneous crystallisation of clinopyroxene and amphibole (Kurzweil *et al.*, 2019). When the three ratios are considered together, it is strongly suggestive of amphibole control on the Ti budget of the co-existing silicate melt rather than magnetite crystallization (Figure 4-6 b). Titanium in the silicate melt has an average V-fold spatial coordination (*e.g.*, Leitzke *et al.* 2018; Mysen and Richet, 2019 and references therein), whereas it sits in the VI-fold (octahedral) coordinated Y-site of amphibole (Tiepolo *et al.*, 2007 and references therein) as well as the VI-fold coordinated B-site of the $\text{ülvospinel-magnetite}$ solid solution (Okube *et al.*, 2018). However, the notion that amphiboles, as silicate minerals, may fractionate Ti isotopes stands in stark contrast with predictions from previous studies (Johnson *et al.*, 2019; Millet *et al.*, 2016; Wang *et al.*, 2019), which focussed more on silicates like olivine, ortho- and clinopyroxene and pyrope garnet, and concluded that silicate crystallization does not lead to resolvable Ti isotope fractionation.

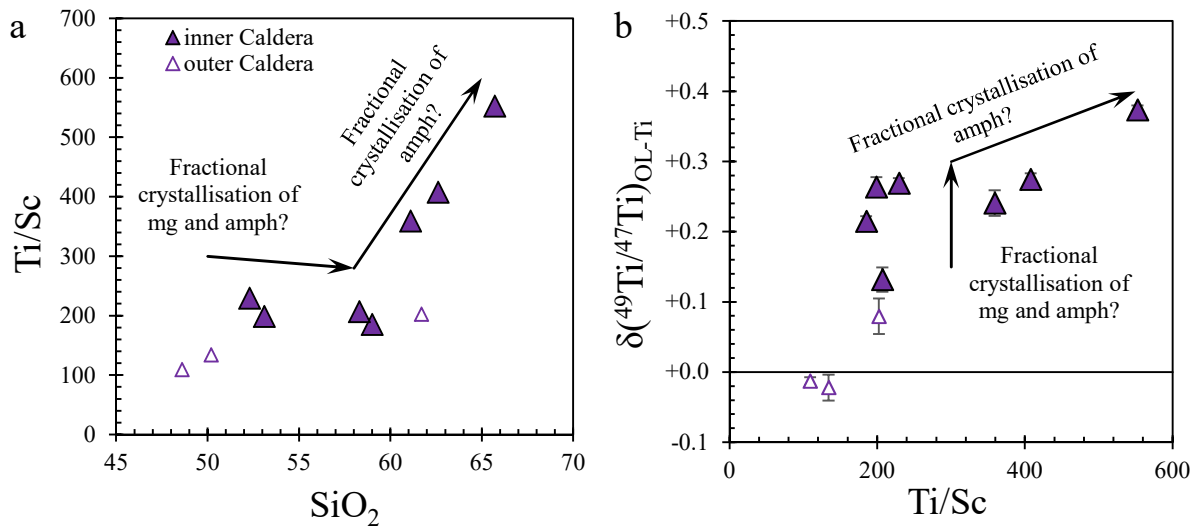


Figure 4-6 a and b: Main, trace element and Ti isotope data for New Britain samples. a) Ti/Sc vs. SiO₂, b) $\delta^{49}\text{Ti}$ vs. Ti/Sc showing how the first vertical array turns into a positive covariation with increasing $\delta^{49}\text{Ti}$ and Ti/Sc. Mg and amph abbreviate magnetite and amphibole, respectively.

High precision HFSE data for these samples (Kurzweil *et al.*, 2019) can be used to further constrain what phases take part in fractionating Ti isotopes. The HFSE show variable partitioning behaviour during fractional crystallization of magnetite and amphibole. For example, magnetite/melt partition coefficients for Nb and Ta (~ 0.04) are substantially lower than those for Hf and Zr (~ 1 – Nielsen, 1992); whereas all HFSE show broadly similar amphibole/melt partition coefficients (0.39, 0.51, 0.37 and 0.67, for Nb, Ta, Hf and Zr, respectively - Tiepolo *et al.*, 2007 and references therein). As such, fractional crystallisation of magnetite, which should result in higher $\delta^{49}\text{Ti}$ in the melt, is expected to lead to a negative covariation between $\delta^{49}\text{Ti}$ and Hf/Nb or Zr/Nb. This covariation is not observed in these samples. There is no covariation in $\delta^{49}\text{Ti}$ vs. Hf/Nb ($\sim 51 \pm 3$) and Zr/Nb ($\sim 1.2 \pm 0.2$), suggesting that the HFSE were not significantly fractionated from each other. This suggests the fractional crystallisation of a phase with a narrow range in HFSE mineral/melt partition coefficients, such as amphibole. With magnetite ruled out, results imply that the involvement of residual amphibole during petrogenesis of the New Britain suite may result in Ti isotope fractionation, which merits further study.

4.4.5 Basalts and their boninitic siblings

Boninites are thought to reflect partial melts from a shallow, depleted mantle region (harzburgitic peridotite), as in the mantle wedge overlying a subducting slab (Crawford *et al.*, 1989; König *et al.*, 2008; Münker, 1998). Boninites are classified into high-Ca (UPL) and low-Ca (Cape Vogel) boninites, with the latter always associated with Cr-spinel (Crawford *et al.*, 1989). Millet *et al.*, (2016) analysed ultramafic mantle samples (Alpine serpentinites) and found no resolvable variation in their $\delta^{49}\text{Ti}$ (weighted mean $\delta^{49}\text{Ti}_{\text{mantle}}$ of $+0.013 \pm 0.023$ ‰). Due to the fact that boninites originate from highly depleted mantle sources, and results from large degrees of partial melting, no significant Ti isotope fractionation is expected, and their isotope composition should reflect that of their mantle source (similar to $\delta^{49}\text{Ti}_{\text{mantle}}$). A comparison between the boninite and tholeiite suites from Troodos (UPL) and Cape Vogel, however, result in an interesting observation. Boninites from both suites have an average $\delta^{49}\text{Ti}$ of $+0.14 \pm 0.04$ ‰, and show a systematically higher $\delta^{49}\text{Ti}$ (by about $+0.1$ ‰) than their tholeiitic counterparts (average $\delta^{49}\text{Ti}$ of $+0.07 \pm 0.05$ ‰) at similar SiO_2 contents, even when they overlap in SiO_2 contents as is the case for the UPL samples (Figure 4-7).

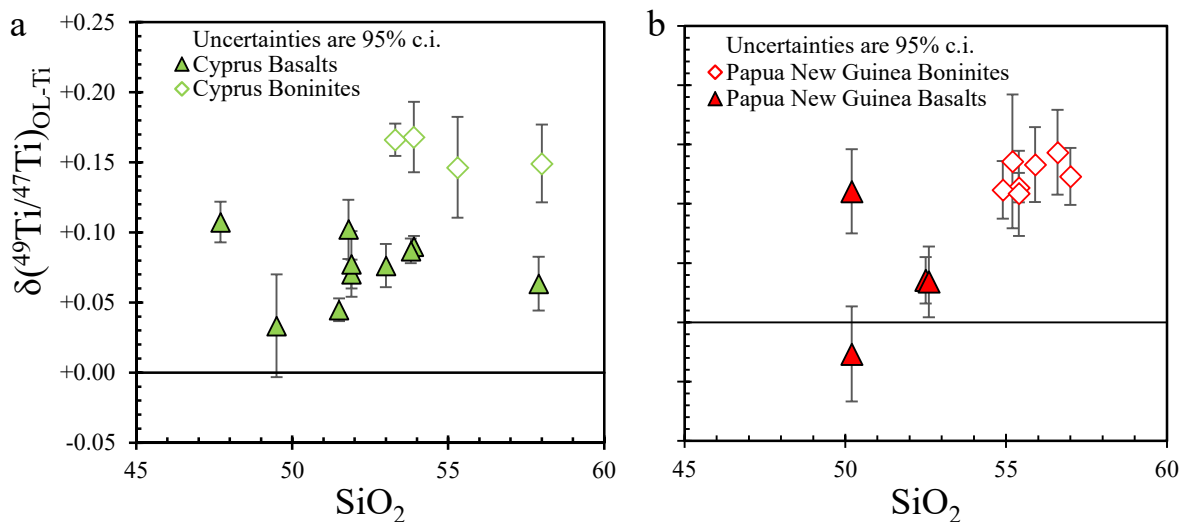


Figure 4-7 a and b: $\delta^{49}\text{Ti}$ vs. SiO_2 for a) Cyprus UPL basalts and boninites and b) Cape Vogel basalts and boninites.

Boninites are thought to result from partial melting of a more depleted mantle source compared to their petrogenetically linked tholeiites (Münker, 1998), which may be related to the

difference in their $\delta^{49}\text{Ti}$. Tholeiite petrogenesis is thought to be dominated by melting of clino- and orthopyroxene in spinel peridotite, and the Ti budget during tholeiite petrogenesis is dominated by these phases (McDonough *et al.*, 1992). As stated earlier, pyroxenes are not known to promote Ti isotope fractionation, so the $\delta^{49}\text{Ti}$ of tholeiitic melts is not expected to differ from their mantle sources, which is the case for MORB for example (Deng *et al.*, 2019; Millet *et al.*, 2016). However, in highly depleted (harzburgitic), mantle sources, the remaining Ti budget is thought to be dominated by residual Cr-spinel, which is usually associated with (low-Ca) boninites (Crawford *et al.*, 1989; McDonough *et al.*, 1992). Chromium-spinel, in similar fashion to the magnetite-ülvospinel solid solution and other Ti-bearing oxides, is expected to favour light Ti isotopes. As such, melting of a spinel-bearing ultra-depleted mantle source (as for boninites) should result in melts with low TiO_2 contents and higher $\delta^{49}\text{Ti}$ when compared to tholeiites, which is the case for boninites meeting expectation. However, even though the higher $\delta^{49}\text{Ti}$ of boninites is related to oxide/melt equilibria during partial melting, it primarily consists of a source signature rather than being the result of fractional crystallization of Fe-Ti oxides from an evolving silicate melt.

4.5 Conclusions

The lack of correlation between known fluid proxies and $\delta^{49}\text{Ti}$ show that during dehydration of slab components, the resulting fluids and fluid-rock interactions do not lead to resolvable Ti isotope fractionation. Whereas recycling of partial melts from subducted sediments is evident in the UPL and Solomon Island suites, in the case of the former this appears to have no impact on its Ti isotope composition. In the latter case, however, the presence of rutile in subducted sediments associated with mantle sources in the Solomon arc, likely contributed to measureable Ti isotope fractionation in basalts from this locality. Involvement of a phase like rutile also appears to affect the Ti isotope composition of samples from the Sunda arc, which can be easily accounted for as being the result of partial melting of a mantle source hosting residual Ti-bearing oxide, or potentially fractional crystallisation of the same phase. Interestingly, amphibole crystallization appears to affect the Ti isotope composition of arc samples from New Britain. The potential effect of fractional crystallisation of amphiboles on the Ti isotope composition of magmas demands further investigation. This is especially important as in previous studies (Johnson *et al.*, 2019; Wang *et al.*, 2019) no evidence was seen for Ti isotope

fractionation involving equilibrium between silicates (*e.g.*, ortho- and clino-pyroxenes, olivine and pyrope) and silicate melt. However, given that no study has thus far examined whether amphibole-melt equilibria can fractionate Ti isotopes, this remains an open question. The offset in $\delta^{49}\text{Ti}$ at similar SiO_2 in boninitic samples from a location (PNG, Cyprus) and tholeiitic samples from the same localities, can be explained by the partial melting of the mantle wedge in the presence of residual, and isotopically lighter, Cr-spinel (McDonough *et al.*, 1992).

Our results further confirm the conclusions of previous studies, namely that the main control on the Ti isotope composition of magmatic samples is the fractional crystallization of Fe-Ti oxides (Deng *et al.*, 2019; Johnson *et al.*, 2019; Millet *et al.*, 2016; Wang *et al.*, 2019). However, this study also shows that other factors (recycling of slab components like sediments) and phases (amphibole) may lead to silicate melts experiencing Ti isotope fractionation that goes beyond the singular effect of oxide crystallization during magmatic differentiation.

CHAPTER 5

CONCLUDING REMARKS

Previous studies showed that Ti isotope fractionation is a result of Fe-Ti oxide involvement during fractional crystallisation and partial melting, expressed by the covariation of $\delta^{49}\text{Ti}$ and SiO_2 (Deng *et al.*, 2018a, 2019; Greber *et al.*, 2017a; Johnson *et al.*, 2019; Millet *et al.*, 2016). The notion that Ti isotopes are exclusively fractionated by processes involving Fe-Ti oxides is supported by mineral separates from natural basaltic melts (Johnson *et al.*, 2019), as well as from ab-initio modelling (Wang *et al.*, 2019). Specifically, silicates like olivine, ortho- and clinopyroxene and pyrope garnet do not fractionate Ti as long as Ti is predominantly tetravalent (Wang *et al.*, 2019). This notion however no longer holds true at lower $f\text{O}_2$ when significant portions of Ti are trivalent, at which point pyroxene group minerals appear to show resolved Ti isotope variations (Wang *et al.*, 2019). Since Ti^{3+} is compatible in clinopyroxene (Mallmann and O'Neill, 2009) and its occurrence is more likely in samples from the Moon, this requires the determination of a Ti^{3+} isotope fractionation factor (Simon *et al.*, 2014; Simon and Sutton, 2017). This tentatively indicates that other phases, apart from Ti oxides, can also fractionate Ti isotopes.

The Ti isotope composition of urKREEP was previously constrained by the Ti isotope composition on a single lunar meteorite ($+0.330 \pm 0.034 \text{ ‰}$, SaU 169; Greber *et al.*, 2017b). Data for KREEP-rich lunar samples from this monograph allow a more robust determination of the Ti isotope compositions of the last residues during LMO solidification. Two of the four analysed KREEP-rich samples overlap with the $\delta^{49}\text{Ti}$ value proposed by Greber *et al.* (2017b) and constrain the Ti isotope composition of urKREEP now with one lunar meteorite and two samples from a sample return mission. Coupled HFSE and Ti isotope modelling provides a second approach to determine the $\delta^{49}\text{Ti}$ of the urKREEP component. Modelled melt HFSE concentrations and Ti isotope compositions in the last stages of LMO solidification are consistent with $\delta^{49}\text{Ti}$ and HFSE contents in KREEP-rich samples analysed in this monograph. More so, this study was able to differentiate between the petrogenetic processes of partial melting of an ilmenite-bearing cumulate (high-Ti mare basalt source region) and fractional crystallisation of ilmenite in a low-Ti magma (low-Ti). As a matter of fact, using modelled IBC during the last stages of various LMO solidification models as petrogenetic source, this monograph shows that the high-Ti mare basalts can best be explained by partial melting of an IBC component. Furthermore, petrogenesis by assimilation of an IBC component into a low-Ti magma can be excluded. Samples that are reported to have formed with no ilmenite at the liquidus, *i.e.*, which show no evidence for fractional crystallisation of ilmenite, are consistently less fractionated than low- and high-Ti ilmenite-bearing basalts. Most of the ilmenite-free

samples are within uncertainty of the Bulk Silicate Earth (Millet *et al.*, 2016) and the chondritic value proposed by Greber *et al.*, (2017b) with a $\delta^{49}\text{Ti} \sim +0.004 \pm 0.010$ ‰. Furthermore, these processes are modelled using recent partitioning data and LMO solidification models (Charlier *et al.*, 2018; Leitzke *et al.*, 2016; Lin *et al.*, 2017; Rapp and Draper, 2018; Snyder *et al.*, 1992; van Westrenen *et al.*, 2000). Modelled evolution trends for $\delta^{49}\text{Ti}_{\text{melt}}$ vs. $\text{Ta}/\text{Hf}_{\text{melt}}$ for fractional crystallisation of ilmenite and partial melting in the presence of ilmenite are consistent with the obtained results for the lunar samples from this study. Since this allowed for a more in-depth investigation of lunar mantle source processes and LMO solidification, it shows the potential of coupled $\delta^{49}\text{Ti}$ - HFSE studies in lunar samples.

Cyprus UPL tholeiites show only little Ti isotope variations. Mass balance calculations reveal that hydrous sediment melts mixing with the mantle melts cannot be the source of Ti isotope fractionation, because the proportion needed to produce the observed Ti contents and $\delta^{49}\text{Ti}$ values would require unrealistically large amounts of sediment. The alternative, that the “undiluted” sediment is much more positive, would result in very high $\delta^{49}\text{Ti}$ values and is as unrealistic as the previous notion. As a matter of fact, the $\delta^{49}\text{Ti}$ variations in Cyprus UPLs are consistent with the inferred depleted mantle wedge source (Fonseca *et al.*, 2017). Trace element variations coupled with $\delta^{49}\text{Ti}$ in samples from the Sunda arc and the Solomon Islands are consistent with residual rutile at the source. This suggests that Ti isotope fractionation in these samples is a result of partial melting in the presence of rutile, possibly (in the case of the Solomon Islands suite) related to overprint of the mantle wedge partial melts from rutile-bearing metasediments. New Britain samples show trace element variation coupled with $\delta^{49}\text{Ti}$ values that tentatively suggest the involvement of amphibole, which is in stark contrast to previous studies stating that fractional crystallisation of olivine, ortho- and clinopyroxene and pyrope garnet do not fractionate Ti isotopes (Johnson *et al.*, 2019; Wang *et al.*, 2019). The notion that fractional crystallisation of (Ca-rich) amphibole leads to Ti isotope fractionation remains to be tested. Lastly, Cape Vogel and Cyprus UPL tholeiites and boninites show a consistent offset in $\delta^{49}\text{Ti}$ vs. SiO_2 from each other, even if they still overlap in SiO_2 content, as is the case for the UPL samples. This offset towards higher $\delta^{49}\text{Ti}$ at comparable SiO_2 contents is consistent with the model for boninite petrogenesis (Crawford *et al.*, 1989). As the mantle wedge is partially molten, pyroxenes and olivine start to melt first and form the tholeiitic magmas (Münker, 1998). The Ti budget in the remaining harzburgitic mantle wedge is then controlled by residual Cr-spinel (McDonough *et al.*, 1992), partial melting in the presence of this oxide phase leads to the observed higher degrees of Ti isotope fractionation.

High precision HFSE data coupled with high precision Ti isotope composition measurements can prove a powerful tool to differentiate the petrogenetic process. Coupled with the SiO₂ trend for differentiation, this allows insights beyond fractional crystallisation of ilmenite. This monograph demonstrates how coupled $\delta^{49}\text{Ti}$ vs. HFSE ratios can differentiate between partial melting of an ilmenite bearing cumulate and fractional crystallisation of ilmenite in lunar basalts as well as partial melting in the presence of amphibole and rutile at the source of subduction zone rocks. Trace element variations coupled with $\delta^{49}\text{Ti}$ tentatively suggest Ti isotope fractionation by fractional crystallisation of amphibole. The results of this study reinforce the requirements for future studies, that will need to focus also on the amphibole group minerals and on the clinopyroxene group and determine fractionation factors for Ti⁴⁺ in Ca-rich amphiboles and Ti³⁺ in clinopyroxene (at lower fO_2). The former is known to have an effect on Ti isotopes (Wang *et al.*, 2019) and given the lower fO_2 on the Moon may be especially relevant for the understanding of Ti isotope fractionation behaviour on the Moon, whereas the latter up until now is only suspected of fractionating Ti isotopes.

– THE END –

ACKNOWLEDGEMENTS

It is time. Time to print, time to hand in. I do not know, where the time went. It still feels like yesterday, when I first set foot into the Poppelsdorfer Schloss. Into the University of Cologne. Suddenly, four years have passed. Where to start?

With the third try, I realize how hard this is. My time here – especially the last year – was among the best of my life, in spite of the experienced hardships. I want to thank my PhD siblings, Ninja Braukmüller, Christian Marien, Maxwell Thiemens for a time full of work and fun. I want to thank Peter Sprung for giving me the position and the freedom it entailed. While we could have done so much more and so much better, I am grateful for the opportunity. I want to thank my supervisors Peter Sprung, Carsten Münker and – even if it wasn't really his job, Raúl Fonseca. While my progress especially in the end was slow, I feel like I have learned a lot, to the betterment of the scientific me. Also a large “thank you” goes to Florian Kurzweil, for additional scientific support.

I also want to thank my Coffee-junkie-friends, Christina Obert, Carina Gerritzen, Laura Müller, Jens Barosch and Ina Martinet. And the rest of the Black Box Cosmochemistry group, past and present, you guys rock! Every. Single. One. Of. You.

All in all, thank you, my friends and family, for working with and being with me, especially in the hard times, in which I never felt alone.

All good things must come to an end, and with ctrl+P, so will this thesis.

Live long, and prosper!

REFERENCES

- Albarède, F., Beard, B. (2004) Analytical Methods for Non-Traditional Isotopes. *Reviews in Mineralogy and Geochemistry* 40.
- Alderman, O.L.G., Skinner, L.B., Benmore, C.J., Tamalonis, A., Weber, J.K.R. (2014) Structure of molten titanium dioxide. *Physical Review B* 90, 094204.
- Allègre, C. (2008) *Isotope Geology*. Cambridge University Press.
- Armytage, R.M.G., Georg, R.B., Williams, H.M., Halliday, A.N. (2012) Silicon isotopes in lunar rocks: Implications for the Moon's formation and the early history of the Earth. *Geochimica et Cosmochimica Acta* 77, 504–514.
- Asphaug, E. (2014) Impact Origin of the Moon? *Annual Review of Earth and Planetary Sciences* 42, 551–578.
- Aston, F.W. (1919) LXXIV. *A positive ray spectrograph*. *The London, Edinburgh, and Dublin Philosophical Magazine and Journal of Science* 38, 707–714.
- Bast, R., Scherer, E.E., Sprung, P., Fischer-Gödde, M., Stracke, A., Mezger, K. (2015) A rapid and efficient ion-exchange chromatography for Lu–Hf, Sm–Nd, and Rb–Sr geochronology and the routine isotope analysis of sub-ng amounts of Hf by MC-ICP-MS. *Journal of Analytical Atomic Spectrometry* 30, 2323–2333.
- Beard, B.L., Johnson, C.M. (2004) Fe Isotope Variations in the Modern and Ancient Earth and Other Planetary Bodies. *Reviews in Mineralogy and Geochemistry* 55, 319–357.
- Beard, B.L., Taylor, L.A., Scherer, E.E., Johnson, C.M., Snyder, G.A. (1998) The Source Region and Melting Mineralogy of High-Titanium and Low-Titanium Lunar Basalts Deduced from Lu-Hf Isotope Data. *Geochimica et Cosmochimica Acta* 62, 525–544.
- Bebout, G.E. (2014) Chemical and Isotopic Cycling in Subduction Zones. *Treatise on Geochemistry*. Elsevier, 703–747.
- Berglund, M., Wieser, M.E. (2011) Isotopic compositions of the elements 2009 (IUPAC Technical Report). *Pure and Applied Chemistry* 83.
- Bigeleisen, J. (1965) Isotope chemistry has opened new areas of chemical physics, geochemistry, and molecular biology. *Science* 147, 10.
- Binder, A.B. (1985) The depths of the Mare basalt source region. *Journal of Geophysical Research* 90, C396.
- Bonnand, P., Parkinson, I.J., Anand, M. (2016) Mass dependent fractionation of stable chromium isotopes in mare basalts: Implications for the formation and the differentiation of the Moon. *Geochimica et Cosmochimica Acta* 175, 208–221.

-
- Canup, R.M. (2014) Lunar-forming impacts: processes and alternatives. *Philosophical Transactions of the Royal Society A: Mathematical, Physical and Engineering Sciences* 372, 20130175.
- Charlier, B., Grove, T.L., Namur, O., Holtz, F. (2018) Crystallization of the lunar magma ocean and the primordial mantle-crust differentiation of the Moon. *Geochimica et Cosmochimica Acta* 234, 50–69.
- Clayton, D. (2003) *Handbook of Isotopes in the Cosmos - Hydrogen to Gallium*. Cambridge University Press.
- Clayton, R.N., Grossman, L., Mayeda, T.K. (1973) A Component of Primitive Nuclear Composition in Carbonaceous Meteorites. *Science* 182, 485–488.
- Coath, C.D., Elliott, T., Hin, R.C. (2017) Double-spike inversion for three-isotope systems. *Chemical Geology* 451, 78–89.
- Codillo, E.A., Le Roux, V., Marschall, H.R. (2018) Arc-like magmas generated by mélange-peridotite interaction in the mantle wedge. *Nature Communications* 9, 2864.
- Compston, W., Oversby, V.M. (1969) Lead isotopic analysis using a double spike. *Journal of Geophysical Research* 74, 4338–4348.
- Craig, H. (1961) Isotopic Variations in Meteoric Waters. *Science* 133, 1702.
- Crawford, A.J., Falloon, T., Green, D. (1989) Classification, Petrogenesis and Tectonic Setting of Boninites. *Boninites and Related Rocks* 1–49.
- Creech, J.B., Paul, B. (2015) IsoSpike: Improved Double-Spike Inversion Software. *Geostandards and Geoanalytical Research* 39, 7–15.
- Cruz-Uribe, A.M., Marschall, H.R., Gaetani, G.A., Le Roux, V. (2018) Generation of alkaline magmas in subduction zones by partial melting of mélange diapirs—An experimental study. *Geology* 46, 343–346.
- Dauphas, N., John, S.G., Rouxel, O. (2017) Iron Isotope Systematics. *Reviews in Mineralogy and Geochemistry* 82, 415–510.
- Dauphas, N., Schauble, E.A. (2016) Mass Fractionation Laws, Mass-Independent Effects, and Isotopic Anomalies. *Annual Review of Earth and Planetary Sciences* 44, 709–783.
- Delano, J.W., Lindsley, D.H. (1982) Chromium, Nickel, and Titanium Abundances in 74275 Olivines: More Evidence for a High-Pressure Origin of High-Titanium Mare Basalts. Thirteenth Lunar and Planetary Science Conference 1982. Lunar and Planetary Institute, Houston, Abstract #1083.
- Demtröder, W. (2010) *Experimentalphysik 4*. Springer Berlin Heidelberg, Berlin, Heidelberg.
- Deng, Z., Chaussidon, M., Savage, P., Robert, F., Pik, R., Moynier, F. (2019) Titanium isotopes as a tracer for the plume or island arc affinity of felsic rocks. *Proceedings of the National Academy of Sciences* 201809164.

- Deng, Z., Moynier, F., Sossi, P.A., Chaussidon, M. (2018a) Bridging the depleted MORB mantle and the continental crust using titanium isotopes. *Geochemical Perspectives Letters* 11–15.
- Deng, Z., Moynier, F., van Zuilen, K., Sossi, P.A., Pringle, E.A., Chaussidon, M. (2018b) Lack of resolvable titanium stable isotopic variations in bulk chondrites. *Geochimica et Cosmochimica Acta* 239, 409–419.
- DePaolo, D.J. (1981) Trace element and isotopic effects of combined wallrock assimilation and fractional crystallization. *Earth and Planetary Science Letters* 53, 189–202.
- Elkins Tanton, L.T., Van Orman, J.A., Hager, B.H., Grove, T.L. (2002) Re-examination of the lunar magma ocean cumulate overturn hypothesis: melting or mixing is required. *Earth and Planetary Science Letters* 196, 239–249.
- Elkins-Tanton, L.T., Burgess, S., Yin, Q.-Z. (2011) The lunar magma ocean: Reconciling the solidification process with lunar petrology and geochronology. *Earth and Planetary Science Letters* 304, 326–336.
- Foley, S., Tiepolo, M., Vannucci, R. (2002) Growth of early continental crust controlled by melting of amphibolite in subduction zones. *Nature* 417, 837–840.
- Fonseca, R.O.C., Kirchenbaur, M., Ballhaus, C., Münker, C., Zirner, A., Gerdes, A., Heuser, A., Botcharnikov, R., Lenting, C. (2017) Fingerprinting fluid sources in Troodos ophiolite complex orbicular glasses using high spatial resolution isotope and trace element geochemistry. *Geochimica et Cosmochimica Acta* 200, 145–166.
- Gerber, S., Burkhardt, C., Budde, G., Metzler, K., Kleine, T. (2017) Mixing and Transport of Dust in the Early Solar Nebula as Inferred from Titanium Isotope Variations among Chondrules. *The Astrophysical Journal* 841, L17.
- Gnos, E. (2004) Pinpointing the Source of a Lunar Meteorite: Implications for the Evolution of the Moon. *Science* 305, 657–659.
- Greber, N.D., Dauphas, N., Bekker, A., Ptáček, M.P., Bindeman, I.N., Hofmann, A. (2017a) Titanium isotopic evidence for felsic crust and plate tectonics 3.5 billion years ago. *Science* 357, 1271–1274.
- Greber, N.D., Dauphas, N., Puchtel, I.S., Hofmann, B.A., Arndt, N.T. (2017b) Titanium stable isotopic variations in chondrites, achondrites and lunar rocks. *Geochimica et Cosmochimica Acta* 213, 534–552.
- Green, D.H., Ringwood, A.E., Hibberson, W.O., Ware, N.G. (1975) Experimental petrology of Apollo 17 mare basalts. *Lunar and Planetary Science Conference Proceedings* 1, 871–893.
- Green, D.H., Ringwood, A.E., Ware, N.G., Hibberson, W.O., Major, A., Kiss, E. (1971) Experimental petrology and petrogenesis of Apollo 12 basalts. *Lunar and Planetary Science Conference Proceedings* 2, 601.

- Green, T.H., Pearson, N.J. (1986) Ti-rich accessory phase saturation in hydrous mafic-felsic compositions at high P,T. *Chemical Geology* 54, 185–201.
- Gross, J., Joy, K.H. (2016) Evolution, Lunar: From Magma Ocean to Crust Formation. In: Cudnik, B. (ed.) *Encyclopedia of Lunar Science*. Springer International Publishing, Cham, 1–20.
- Handley, H.K., Blichert-Toft, J., Gertisser, R., Macpherson, C.G., Turner, S.P., Zaennudin, A., Abdurrachman, M. (2014) Insights from Pb and O isotopes into along-arc variations in subduction inputs and crustal assimilation for volcanic rocks in Java, Sunda arc, Indonesia. *Geochimica et Cosmochimica Acta* 139, 205–226.
- Handley, H.K., Macpherson, C.G., Davidson, J.P., Berlo, K., Lowry, D. (2007) Constraining Fluid and Sediment Contributions to Subduction-Related Magmatism in Indonesia: Ijen Volcanic Complex. *Journal of Petrology* 48, 1155–1183.
- Handley, H.K., Turner, S., Macpherson, C.G., Gertisser, R., Davidson, J.P. (2011) Hf–Nd isotope and trace element constraints on subduction inputs at island arcs: Limitations of Hf anomalies as sediment input indicators. *Earth and Planetary Science Letters* 304, 212–223.
- Hermann, J., Rubatto, D. (2009) Accessory phase control on the trace element signature of sediment melts in subduction zones. *Chemical Geology* 265, 512–526.
- Herwartz, D., Pack, A., Friedrichs, B., Bischoff, A. (2014) Identification of the giant impactor Theia in lunar rocks. *Science* 344, 1146–1150.
- Heuser, A., Eisenhauer, A., Gussone, N., Bock, B., Hansen, B.T., Nögler, Th.F. (2002) Measurement of calcium isotopes ($\delta^{44}\text{Ca}$) using a multicollector TIMS technique. *International Journal of Mass Spectrometry* 220, 385–397.
- Hiesinger, H. (2006) New Views of Lunar Geoscience: An Introduction and Overview. *Reviews in Mineralogy and Geochemistry* 60, 1–81.
- Hoefs, J. (2009) *Stable isotope geochemistry*. Springer, Berlin.
- Hopkins, S.S., Prytulak, J., Barling, J., Russell, S.S., Coles, B.J., Halliday, A.N. (2019) The vanadium isotopic composition of lunar basalts. *Earth and Planetary Science Letters* 511, 12–24.
- Ionov, D.A., Hofmann, A.W. (1995) Nb–Ta-rich mantle amphiboles and micas: Implications for subduction-related metasomatic trace element fractionations. *Earth and Planetary Science Letters* 131, 341–356.
- Jochum, K.P., Enzweiler, J. (2014) Reference Materials in Geochemical and Environmental Research. *Treatise on Geochemistry*. Elsevier, 43–70.
- Johnson, A.C., Aarons, S.M., Dauphas, N., Nie, N.X., Zeng, H., Helz, R.T., Romaniello, S.J., Anbar, A.D. (2019) Titanium isotopic fractionation in Kilauea Iki lava lake driven by oxide crystallization. *Geochimica et Cosmochimica Acta* 264, 180–190.

- Johnson, C.M., Beard, B.L., Albarede, F. (2004) Overview and General Concepts. *Reviews in Mineralogy and Geochemistry* 55, 1–24.
- Joshima, M., Okuda, Y., Murakami, F., Kishimoto, K., Honza, E. (1986) Age of the Solomon Sea Basin from magnetic lineations. *Geo-Marine Letters* 6, 229–234.
- Kessel, R., Schmidt, M.W., Ulmer, P., Pettke, T. (2005) Trace element signature of subduction-zone fluids, melts and supercritical liquids at 120–180 km depth. *Nature* 437, 724–727.
- Kesson, S.E. (1975) Melting Experiments on Synthetic Mare Basalts and Their Petrogenetic Implications. Sixth Lunar Science Conference 1975. Lunar and Planetary Institute, Houston, Abstract #1168.
- Kesson, S.E., Ringwood, A.E. (1976) Mare basalt petrogenesis in a dynamic moon. *Earth and Planetary Science Letters* 30, 155–163.
- Kirchenbaur, M., Münker, C. (2015) The behaviour of the extended HFSE group (Nb, Ta, Zr, Hf, W, Mo) during the petrogenesis of mafic K-rich lavas: The Eastern Mediterranean case. *Geochimica et Cosmochimica Acta* 165, 178–199.
- Kirchenbaur, M., Munker, C., Schuth, S., Garbe-Schonberg, D., Marchev, P. (2012) Tectonomagmatic Constraints on the Sources of Eastern Mediterranean K-rich Lavas. *Journal of Petrology* 53, 27–65.
- Klaver, M., Djuly, T., de Graaf, S., Sakes, A., Wijbrans, J., Davies, G., Vroon, P. (2015) Temporal and spatial variations in provenance of Eastern Mediterranean Sea sediments: Implications for Aegean and Aeolian arc volcanism. *Geochimica et Cosmochimica Acta* 153, 149–168.
- Klemme, S., Günther, D., Hametner, K., Prowatke, S., Zack, T. (2006a) The partitioning of trace elements between ilmenite, ulvospinel, armalcolite and silicate melts with implications for the early differentiation of the moon. *Chemical Geology* 234, 251–263.
- Klemme, S., Günther, D., Hametner, K., Prowatke, S., Zack, T. (2006b) The partitioning of trace elements between ilmenite, ulvospinel, armalcolite and silicate melts with implications for the early differentiation of the moon. *Chemical Geology* 234, 251–263.
- Klemme, S., Prowatke, S., Hametner, K., Günther, D. (2005) Partitioning of trace elements between rutile and silicate melts: Implications for subduction zones. *Geochimica et Cosmochimica Acta* 69, 2361–2371.
- König, S., Münker, C., Hohl, S., Paulick, H., Barth, A.R., Lagos, M., Pfänder, J., Büchl, A. (2011) The Earth's tungsten budget during mantle melting and crust formation. *Geochimica et Cosmochimica Acta* 75, 2119–2136.
- König, S., Münker, C., Schuth, S., Garbe-Schönberg, D. (2008) Mobility of tungsten in subduction zones. *Earth and Planetary Science Letters* 274, 82–92.

-
- König, S., Münker, C., Schuth, S., Luguët, A., Hoffmann, J.E., Kuduon, J. (2010) Boninites as windows into trace element mobility in subduction zones. *Geochimica et Cosmochimica Acta* 74, 684–704.
- Kopecky, J., Sublet, J.-Ch., Simpson, J.A., Forrest, R.A., Nierop, D. (2001) *Atlas of Neutron Capture Cross Sections. Nuclear Data Section - International Atomic Energy Agency. Database.* .
- Kurzweil, F., Münker, C., Grupp, M., Braukmüller, N., Fechtner, L., Christian, M., Hohl, S.V., Schoenberg, R. (2019) The stable tungsten isotope composition of modern igneous reservoirs. *Geochimica et Cosmochimica Acta* 251, 176–191.
- Kurzweil, F., Münker, C., Tusch, J., Schoenberg, R. (2018) Accurate stable tungsten isotope measurements of natural samples using a 180 W- 183 W double-spike. *Chemical Geology* 476, 407–417.
- Leitzke, F.P., Fonseca, R.O.C., Göttlicher, J., Steininger, R., Jahn, S., Prescher, C., Lagos, M. (2018) Ti K-edge XANES study on the coordination number and oxidation state of Titanium in pyroxene, olivine, armalcolite, ilmenite, and silicate glass during mare basalt petrogenesis. *Contributions to Mineralogy and Petrology* 173, 103.
- Leitzke, F.P., Fonseca, R.O.C., Michely, L.T., Sprung, P., Münker, C., Heuser, A., Blanchard, H. (2016) The effect of titanium on the partitioning behavior of high-field strength elements between silicates, oxides and lunar basaltic melts with applications to the origin of mare basalts. *Chemical Geology* 440, 219–238.
- Leya, I., Schönbacher, M., Wiechert, U., Krähenbühl, U., Halliday, A.N. (2008) Titanium isotopes and the radial heterogeneity of the solar system. *Earth and Planetary Science Letters* 266, 233–244.
- Li, H., Zhang, N., Liang, Y., Wu, B., Dygert, N.J., Huang, J., Parmentier, E.M. (2019) Lunar Cumulate Mantle Overturn: A Model Constrained by Ilmenite Rheology. *Journal of Geophysical Research: Planets* 2018JE005905.
- Lin, Y., Tronche, E.J., Steenstra, E.S., van Westrenen, W. (2017) Experimental constraints on the solidification of a nominally dry lunar magma ocean. *Earth and Planetary Science Letters* 471, 104–116.
- Longhi, J. (1992) Experimental petrology and petrogenesis of mare volcanics. *Geochimica et Cosmochimica Acta* 56, 2235–2251.
- Mallmann, G., O'Neill, H.St.C. (2009) The Crystal/Melt Partitioning of V during Mantle Melting as a Function of Oxygen Fugacity Compared with some other Elements (Al, P, Ca, Sc, Ti, Cr, Fe, Ga, Y, Zr and Nb). *Journal of Petrology* 50, 1765–1794.
- Mandl, M.B., Fehr, M.A., Schönbacher, M. (2018) Titanium stable isotope fractionation on the Moon: Evidence for inter- mineral isotopic fractionation. *Goldschmidt 2018* 2018, 1.
-

- Marien, C.S., Hoffmann, J.E., Garbe-Schönberg, C.-D., Münker, C. (2019) Petrogenesis of plagiogranites from the Troodos Ophiolite Complex, Cyprus. *Contributions to Mineralogy and Petrology* 174, 35.
- Marschall, H.R., Schumacher, J.C. (2012) Arc magmas sourced from mélange diapirs in subduction zones. *Nature Geoscience* 5, 862–867.
- Mattauch, J., Herzog, R. (1934) Über einen neuen Massenspektrographen. *Zeitschrift für Physik* 89, 786–795.
- May, T.W., Wiedmeyer, R.H. (2008) A Table of Polyatomic interferences in ICP MS.pdf. *Atomic Spectroscopy* 18, 150–159.
- McCulloch, M.T., Gamble, J.A. (1991) Geochemical and geodynamical constraints on subduction zone magmatism. *Earth and Planetary Science Letters* 102, 358–374.
- McDonough, W.F., Stosch, H.-G., Ware, N.G. (1992) Distribution of titanium and the rare earth elements between peridotitic minerals. *Contributions to Mineralogy and Petrology* 110, 321–328.
- Meyer, C. (2012) Lunar Sample Compendium. 10.
- Millet, M.-A., Dauphas, N. (2014) Ultra-precise titanium stable isotope measurements by double-spike high resolution MC-ICP-MS. *Journal of Analytical Atomic Spectrometry* 29, 1444.
- Millet, M.-A., Dauphas, N., Greber, N.D., Burton, K.W., Dale, C.W., Debret, B., Macpherson, C.G., Nowell, G.M., Williams, H.M. (2016) Titanium stable isotope investigation of magmatic processes on the Earth and Moon. *Earth and Planetary Science Letters* 449, 197–205.
- Münker, C. (1998) Nb/Ta fractionation in a Cambrian arc/back arc system, New Zealand: source constraints and application of refined ICPMS techniques. *Chemical Geology* 144, 23–45.
- Münker, C. (2010) A high field strength element perspective on early lunar differentiation. *Geochimica et Cosmochimica Acta* 74, 7340–7361.
- Münker, C., Weyer, S., Scherer, E., Mezger, K. (2001) Separation of high field strength elements (Nb, Ta, Zr, Hf) and Lu from rock samples for MC-ICPMS measurements: SEPARATION OF HIGH FIELD STRENGTH ELEMENTS. *Geochemistry, Geophysics, Geosystems* 2, n/a-n/a.
- Mysen, B., Richet, P. (2019) Titanium-Bearing Systems. *Silicate Glasses and Melts*. Elsevier, 431–466.
- Nielsen, R.L. (1992) BIGD.FOR: A FORTRAN program to calculate trace-element partition coefficients for natural mafic and intermediate composition magmas. *Computers & Geosciences* 18, 773–788.

-
- Nielsen, S.G., Marschall, H.R. (2017) Geochemical evidence for mélange melting in global arcs. *Science Advances* 3, e1602402.
- Nielsen, S.G., Prytulak, J., Halliday, A.N. (2011) Determination of Precise and Accurate $^{51}\text{V}/^{50}\text{V}$ Isotope Ratios by MC-ICP-MS, Part 1: Chemical Separation of Vanadium and Mass Spectrometric Protocols. *Geostandards and Geoanalytical Research* 35, 293–306.
- Nier, A.O. (1940) A Mass Spectrometer for Routine Isotope Abundance Measurements. *Review of Scientific Instruments* 11, 212–216.
- Okube, M., Oshiumi, T., Nagase, T., Miyawaki, R., Yoshiasa, A., Sasaki, S., Sugiyama, K. (2018) Site occupancy of Fe^{2+} , Fe^{3+} and Ti^{4+} in titanomagnetite determined by valence-difference contrast in synchrotron X-ray resonant scattering. *Journal of Synchrotron Radiation* 25, 1694–1702.
- Olesik, J.W., Jiao, S. (2017) Matrix effects using an ICP-MS with a single positive ion lens and grounded stop: analyte mass dependent? *Journal of Analytical Atomic Spectrometry* 32, 951–966.
- Pahlevan, K., Stevenson, D.J. (2007) Equilibration in the aftermath of the lunar-forming giant impact. *Earth and Planetary Science Letters* 262, 438–449.
- Pearce, J.A., Peate, D.W. (1995) Tectonic Implications of the Composition of Volcanic ARC Magmas. *Annual Review of Earth and Planetary Sciences* 23, 251–285.
- Peate, D.W., Pearce, J.A., Hawkesworth, C.J., Colley, H., Edwards, C.M.H., Hirose, K. (1997) Geochemical Variations in Vanuatu Arc Lavas: the Role of Subducted Material and a Variable Mantle Wedge Composition. 38, 28.
- Plank, T. (2014) The Chemical Composition of Subducting Sediments. *Treatise on Geochemistry*. Elsevier, 607–629.
- Poitrasson, F., Halliday, A.N., Lee, D.-C., Levasseur, S., Teutsch, N. (2004) Iron isotope differences between Earth, Moon, Mars and Vesta as possible records of contrasted accretion mechanisms. *Earth and Planetary Science Letters* 223, 253–266.
- Poitrasson, F., Zambardi, T., Magna, T., Neal, C.R. (2019) A reassessment of the iron isotope composition of the Moon and its implications for the accretion and differentiation of terrestrial planets. *Geochimica et Cosmochimica Acta* 267, 257–274.
- Prytulak, J. *et al.* (2013) The stable vanadium isotope composition of the mantle and mafic lavas. *Earth and Planetary Science Letters* 365, 177–189.
- Prytulak, J., Nielsen, S.G., Halliday, A.N. (2011) Determination of Precise and Accurate $^{51}\text{V}/^{50}\text{V}$ Isotope Ratios by Multi-Collector ICP-MS, Part 2: Isotopic Composition of Six Reference Materials plus the Allende Chondrite and Verification Tests. *Geostandards and Geoanalytical Research* 35, 307–318.
- Rapp, J.F., Draper, D.S. (2018) Fractional crystallization of the lunar magma ocean: Updating the dominant paradigm. *Meteoritics & Planetary Science* 53, 1432–1455.
-

- Regelous, M., Haase, K.M., Freund, S., Keith, M., Weinzierl, C.G., Beier, C., Brandl, P.A., Endres, T., Schmidt, H. (2014) Formation of the Troodos Ophiolite at a triple junction: Evidence from trace elements in volcanic glass. *Chemical Geology* 386, 66–79.
- Render, J., Ebert, S., Burkhardt, C., Kleine, T., Brennecka, G.A. (2019) Titanium isotopic evidence for a shared genetic heritage of refractory inclusions from different carbonaceous chondrites. *Geochimica et Cosmochimica Acta* 254, 40–53.
- Reufer, A., Meier, M.M.M., Benz, W., Wieler, R. (2012) A hit-and-run giant impact scenario. *Icarus* 221, 296–299.
- Ringwood, A.E. (1970) Special Papers-Apollo 11 Symposium: Petrogenesis of Apollo 11 Basalts and Implications for Lunar Origin. *Journal of Geophysical Research* 75, 6453–6479.
- Rudge, J.F., Reynolds, B.C., Bourdon, B. (2009) The double spike toolbox. *Chemical Geology* 265, 420–431.
- Rufu, R., Aharonson, O., Perets, H.B. (2017) A multiple-impact origin for the Moon. *Nature Geoscience* 10, 89–94.
- Schauble, E.A. (2004) Applying Stable Isotope Fractionation Theory to New Systems. *Reviews in Mineralogy and Geochemistry* 55, 65–111.
- Schmidt, M.W., Poli, S. (1998) Experimentally based water budgets for dehydrating slabs and consequences for arc magma generation. *Earth and Planetary Science Letters* 163, 361–379.
- Schoenberg, R., Zink, S., Staubwasser, M., von Blanckenburg, F. (2008) The stable Cr isotope inventory of solid Earth reservoirs determined by double spike MC-ICP-MS. *Chemical Geology* 249, 294–306.
- Schuth, S., Münker, C., König, S., Qopoto, C., Basi, S., Garbe-Schönberg, D., Ballhaus, C. (2009) Petrogenesis of Lavas along the Solomon Island Arc, SW Pacific: Coupling of Compositional Variations and Subduction Zone Geometry. *Journal of Petrology* 50, 781–811.
- Sharp, Z.D. (2007) *Principles of stable Isotope Geochemistry*. Pearson.
- Shaw, D.M. (1970) Trace element fractionation during anatexis. *Geochimica et Cosmochimica Acta* 34, 237–243.
- Shearer, C.K. (2006) Thermal and Magmatic Evolution of the Moon. *Reviews in Mineralogy and Geochemistry* 60, 365–518.
- Shih, C.-Y., Wiesmann, H.W., Haskin, L.A. (1975) On the Origin of High-Ti Mare Basalts. Sixth Lunar Science Conference 1975. Lunar and Planetary Institute, Houston, Abstract #1245.

-
- Siebert, C., Nägler, T.F., Kramers, J.D. (2001) Determination of molybdenum isotope fractionation by double-spike multicollector inductively coupled plasma mass spectrometry. *Geochemistry, Geophysics, Geosystems* 2.
- Simon, S.B., Sutton, S.R. (2017) Valence of Ti, V, and Cr in Apollo 14 aluminous basalts 14053 and 14072. *Meteoritics & Planetary Science* 52, 2051–2066.
- Simon, S.B., Sutton, S.R., Grossman, L. (2007) Valence of titanium and vanadium in pyroxene in refractory inclusion interiors and rims. *Geochimica et Cosmochimica Acta* 71, 3098–3118.
- Simon, S.B., Sutton, S.R., Grossman, L. (2014) Valence of Ti in lunar rocks: The first direct measurements. *45th Lunar and Planetary Science Conference*. LPSC 2014. Houston.
- Skora, S., Blundy, J. (2010) High-pressure Hydrous Phase Relations of Radiolarian Clay and Implications for the Involvement of Subducted Sediment in Arc Magmatism. *Journal of Petrology* 51, 2211–2243.
- Snyder, G.A., Taylor, L.A., Neal, C.R. (1992) A chemical model for generating the sources of mare basalts: Combined equilibrium and fractional crystallization of the lunar magmasphere. *Geochimica et Cosmochimica Acta* 56, 3809–3823.
- Sossi, P.A., Moynier, F. (2017) Chemical and isotopic kinship of iron in the Earth and Moon deduced from the lunar Mg-Suite. *Earth and Planetary Science Letters* 471, 125–135.
- Sossi, P.A., Moynier, F., van Zuilen, K. (2018) Volatile loss following cooling and accretion of the Moon revealed by chromium isotopes. *Proceedings of the National Academy of Sciences* 115, 10920–10925.
- Sossi, P.A., Nebel, O., Foden, J. (2016) Iron isotope systematics in planetary reservoirs. *Earth and Planetary Science Letters* 452, 295–308.
- Sossi, P.A., O'Neill, H.St.C. (2017) The effect of bonding environment on iron isotope fractionation between minerals at high temperature. *Geochimica et Cosmochimica Acta* 196, 121–143.
- Sprung, P., Kleine, T., Scherer, E.E. (2013) Isotopic evidence for chondritic Lu/Hf and Sm/Nd of the Moon. *Earth and Planetary Science Letters* 380, 77–87.
- Sprung, P., Scherer, E.E., Upadhyay, D., Leya, I., Mezger, K. (2010) Non-nucleosynthetic heterogeneity in non-radiogenic stable Hf isotopes: Implications for early solar system chronology. *Earth and Planetary Science Letters* 295, 1–11.
- Stern, R.J. (2002) Subduction zones. *Reviews of Geophysics* 40, 1012.
- Taylor, H.P. (1974) The Application of Oxygen and Hydrogen Isotope Studies to Problems of Hydrothermal Alteration and Ore Deposition. *Economic Geology* 69, 843–883.
- Tejada, M.L.G., Mahoney, J.J., Castillo, P.R., Ingle, S.P., Sheth, H.C., Weis, D. (2004) Pin-pricking the elephant: evidence on the origin of the Ontong Java Plateau from Pb-Sr
-

- Hf-Nd isotopic characteristics of ODP Leg 192 basalts. *Geological Society, London, Special Publications* 229, 133.
- Teng, F.-Z., Dauphas, N., Watkins, J.M. (2017) Non-Traditional Stable Isotopes: Retrospective and Prospective. *Reviews in Mineralogy and Geochemistry* 82, 1–26.
- Thiemens, M.H. (2006) HISTORY AND APPLICATIONS OF MASS-INDEPENDENT ISOTOPE EFFECTS. *Annual Review of Earth and Planetary Sciences* 34, 217–262.
- Thiemens, M.H., Heidenreich, J.E. (1983) The Mass-Independent Fractionation of Oxygen: A Novel Isotope Effect and Its Possible Cosmochemical Implications. *Science* 219, 1073.
- Thiemens, M.M., Sprung, P., Fonseca, R.O.C., Leitzke, F.P., Münker, C. (2019) Early Moon formation inferred from hafnium–tungsten systematics. *Nature Geoscience*.
- Thomson, R., W. (1914) Rays of Positive Electricity and their Application to Chemical Analysis. *Nature* 92, 549–550.
- Tiepolo, M., Oberti, R., Zanetti, A., Vannucci, R., Foley, S.F. (2007) Trace-Element Partitioning Between Amphibole and Silicate Melt. *Reviews in Mineralogy and Geochemistry* 67, 417–452.
- Toplis, M.J., Carroll, M.R. (1995) An Experimental Study of the Influence of Oxygen Fugacity on Fe-Ti Oxide Stability, Phase Relations, and Mineral–Melt Equilibria in Ferro-Basaltic Systems. *Journal of Petrology* 36, 1137–1170.
- Toplis, M.J., Corgne, A. (2002) An experimental study of element partitioning between magnetite, clinopyroxene and iron-bearing silicate liquids with particular emphasis on vanadium. *Contributions to Mineralogy and Petrology* 144, 22–37.
- Trinquier, A., Elliott, T., Ulfbeck, D., Coath, C., Krot, A.N., Bizzarro, M. (2009) Origin of nucleosynthetic isotope heterogeneity in the solar protoplanetary disk. *Science* 324, 374–376.
- Tusch, J., Sprung, P., van de Löcht, J., Hoffmann, J.E., Boyd, A.J., Rosing, M.T., Münker, C. (2019) Uniform ^{182}W isotope compositions in Eoarchean rocks from the Isua region, SW Greenland: The role of early silicate differentiation and missing late veneer. *Geochimica et Cosmochimica Acta* 257, 284–310.
- van Kan Parker, M., Mason, P.R.D., van Westrenen, W. (2011) Trace element partitioning between ilmenite, armalcolite and anhydrous silicate melt: Implications for the formation of lunar high-Ti mare basalts. *Geochimica et Cosmochimica Acta* 75, 4179–4193.
- van Westrenen, W., Blundy, J.D., Wood, B.J. (2000) Effect of Fe_2O_3 on garnet–melt trace element partitioning: experiments in FCMAF and quantification of crystal-chemical controls in natural systems. 13.
- Wadhwa, M. (2008) Redox Conditions on Small Bodies, the Moon and Mars. *Reviews in Mineralogy and Geochemistry* 68, 493–510.

-
- Walker, D., Longhi, J., Lasaga, A.C., Stolper, E.M., Grove, T.L., Hays, J.F. (1977) Slowly cooled microgabbros 15555 and 15065. *Lunar and Planetary Science Conference Proceedings 2*, 1521–1547.
- Walker, D.A., McDougall, I. (1982) $^{40}\text{Ar}/^{39}\text{Ar}$ and K-Ar dating of altered glassy volcanic rocks: the Dabi Volcanics, Papua New Guinea. *Geochimica et Cosmochimica Acta* 46, 2181–2190.
- Wang, K., Jacobsen, S.B., Sedaghatpour, F., Chen, H., Korotev, R.L. (2015) The earliest Lunar Magma Ocean differentiation recorded in Fe isotopes. *Earth and Planetary Science Letters* 430, 202–208.
- Wang, M., Audi, G., Kondev, F.G., Huang, W.J., Naimi, S., Xu, X. (2017) The AME2016 atomic mass evaluation (II). Tables, graphs and references. *Chinese Physics C* 41, 030003.
- Wang, W., Huang, S., Huang, F., Zhao, X., Wu, Z. (2019) Equilibrium inter-mineral titanium isotope fractionation: Implication for high-temperature titanium isotope geochemistry. *Geochimica et Cosmochimica Acta* S0016703719307069.
- Warren, P.H., Taylor, G.J. (2014) The Moon. *Treatise on Geochemistry*. Elsevier, 213–250.
- Warren, P.H., Wasson, J.T. (1979) The origin of KREEP. *Reviews of Geophysics* 17, 73.
- Wasserburg, G.J., Papanastassiou, D.A., Nienow, E.V., Bauman, C.A. (1969) A Programmable Magnetic Field Mass Spectrometer with On-Line Data Processing. *Review of Scientific Instruments* 40, 288–295.
- Watkins, J.M., DePaolo, D.J., Watson, E.B. (2017) Kinetic Fractionation of Non-Traditional Stable Isotopes by Diffusion and Crystal Growth Reactions. *Reviews in Mineralogy and Geochemistry* 82, 85–125.
- Weyer, S., Anbar, A., Brey, G., Munker, C., Mezger, K., Woodland, A. (2005) Iron isotope fractionation during planetary differentiation. *Earth and Planetary Science Letters* 240, 251–264.
- White, W.M., Klein, E.M. (2014) Composition of the Oceanic Crust. *Treatise on Geochemistry*. Elsevier, 457–496.
- Wiechert, U. (2001) Oxygen Isotopes and the Moon-Forming Giant Impact. *Science* 294, 345–348.
- Woelki, D., Regelous, M., Haase, K.M., Romer, R.H.W., Beier, C. (2018) Petrogenesis of boninitic lavas from the Troodos Ophiolite, and comparison with Izu–Bonin–Mariana fore-arc crust. *Earth and Planetary Science Letters* 498, 203–214.
- Woodhead, J.D., Eggins, S.M., Johnson, R.W. (1998) Magma Genesis in the New Britain Island Arc: Further Insights into Melting and Mass Transfer Processes. 39, 28.
-

- Yu, S., Tosi, N., Schwinger, S., Maurice, M., Breuer, D., Xiao, L. (2019) Overturn of Ilmenite-Bearing Cumulates in a Rheologically Weak Lunar Mantle. *Journal of Geophysical Research: Planets* 124, 418–436.
- Zhang, J., Dauphas, N., Davis, A.M., Leya, I., Fedkin, A. (2012) The proto-Earth as a significant source of lunar material. *Nature Geoscience* 5, 251–255.
- Zhao, Y., de Vries, J., van den Berg, A.P., Jacobs, M.H.G., van Westrenen, W. (2019) The participation of ilmenite-bearing cumulates in lunar mantle overturn. *Earth and Planetary Science Letters* 511, 1–11.

APPENDIX A

Table 7-1: Appendix, used trace elements (lunar samples). Trace element and Ti isotope data used in this study. Main elements data is compiled using the lunar sample compendium and the references therein (Meyer 2012); HFSE data by Thiemens *et al.*, (2019)

Data - This study			Ti isotope data				Main elements - Meyer (2012) wt%				HFSE - Thiemens <i>et al.</i> , (2019) µg/g						
NASA ID	Mission	Rock type	$\delta^{49}\text{Ti}$	2 s	n	95% c.i.	SiO ₂	TiO ₂	FeO	MgO	W	Th	U	Hf	Zr	Nb	Ta
10017	Apollo 11	High-Ti ilm basalt	0.009	0.024	6	0.012	41.3	11.9	19.6	7.76	0.382	3.40	0.858	16.3	491	30.4	1.82
10020		High-Ti ilm basalt	0.011	0.022	6	0.011	40.7	10.6	18.5	8.06	0.331	0.667	0.180	7.31	201	17.5	1.10
10057		High-Ti ilm basalt	0.009	0.024	6	0.012	41.6	11.4	19.1	7.02	0.386	3.56	0.856	16.2	490	30.7	1.81
74255	Apollo 17	High-Ti ilm basalt	0.043	0.010	6	0.005	38.4	12.2	18.0	10.7	0.064	0.450	0.132	8.21	221	25.9	1.43
74275		High-Ti ilm basalt	0.045	0.010	6	0.005	38.7	12.7	18.0	10.2	0.059	0.466	0.138	8.67	233	28.6	1.50
75035		High-Ti ilm basalt	0.115	0.025	6	0.013	42.6	10.1	18.8	6.25	0.091	0.546	0.163	11.6	322	32.9	1.93
79135	Apollo 17	High-Ti Bce	0.019	0.017	6	0.009	42.3	5.15	14.8	10.4	0.189	1.34	0.368	5.88	190	15.0	0.901
79035		High-Ti Bce	0.047	0.018	6	0.010	41.7	6.58	15.6	9.91	0.165	1.16	0.315	5.88	182	15.8	0.961
14305	Apollo 14	KREEP-rich Bce	0.296	0.030	6	0.016	48.4	1.71	10.6	10.3	1.28	16.4	4.33	28.3	1163	73.6	3.26
68115	Apollo 16	KREEP-rich Bce	0.117	0.027	6	0.014	44.8	0.34	4.00	5.79	0.549	4.45	1.17	8.92	360	23.8	0.974
72275	Apollo 17	KREEP-rich Bce	0.185	0.026	6	0.014	48.0	0.91	11.9	10.0	0.924	5.84	1.51	15.9	658	31.0	1.40
14310	Apollo 14	KREEP basalt	0.263	0.035	6	0.018	48.3	1.24	7.93	8.00	1.21	10.9	2.98	20.1	817	51.4	2.31
15058	Apollo 15	Low-Ti QNB	-0.010	0.034	6	0.018	47.8	1.77	20.0	9.01	0.059	0.576	0.150	2.76	98	6.62	0.366
15065		Low-Ti QNB	-0.030	0.014	6	0.007	47.2	1.33	19.2	10.7	0.090	0.863	0.216	3.96	139	9.96	0.522
15495		Low-Ti QNB	0.011	0.017	6	0.009	48.0	1.52	20.7	10.4	0.069	0.670	0.169	3.07	110	6.80	0.380
15545		Low-Ti ONB	0.011	0.032	6	0.017	45.0	2.33	22.2	10.5	0.081	0.491	0.132	2.53	85	6.15	0.374
15556		Low-Ti ONB	0.007	0.030	6	0.016	45.7	2.76	21.9	8.67	0.088	0.512	0.154	2.67	89	6.38	0.392
15555		Low-Ti ONB	-0.008	0.026	6	0.014	44.2	2.10	22.4	11.2	0.063	0.432	0.112	2.09	70	5.01	0.304
12022	Apollo 12	Low-Ti ilm basalt	0.029	0.022	6	0.011	43.2	5.10	22.0	10.4	0.088	0.677	0.182	4.29	121	6.68	0.359
12051		Low-Ti ilm basalt	0.030	0.022	8	0.009	45.1	4.62	20.2	7.21	0.127	0.804	0.208	4.04	121	7.67	0.427
12063		Low-Ti ilm basalt	0.055	0.022	6	0.012	43.5	5.00	21.3	9.56	0.085	0.661	0.172	4.10	115	6.62	0.376
12054		Low-Ti ilm basalt	0.028	0.026	6	0.014	43.3	4.63	19.6	9.22	0.123	0.977	0.255	5.31	153	8.91	0.499
12004	Apollo 12	Low-Ti olv basalt	0.006	0.010	6	0.005	45.2	2.88	21.5	12.5	0.115	0.959	0.260	3.45	114	7.78	0.406
12053	Apollo 12	Low-Ti pgt basalt	-0.013	0.026	6	0.014	47.3	3.32	19.8	8.06	0.122	1.04	0.272	3.77	122	8.50	0.446

Table 7-2: Appendix, used trace element data in the arc study. Data compiled from previous studies (Fonseca et al., 2017; Kirchenbaur and Münker, 2015; König et al., 2008, 2010; Kurzweil et al., 2019; Schuth et al., 2009)

		Main and trace element data													
						wt.-%		µg/g							
		$\delta(^{49}\text{Ti}/^{47}\text{Ti})^{\text{OL-Ti}}$	2 s	n	95% c.i.	SiO ₂	TiO ₂	MgO	Th	Zr	Hf	Nb	Ta	Sm	Sc
<i>Cyprus Basalts</i>															
CY-1	Basalt	0.090	0.010	4	0.008	53.9	0.390	7.40	0.132	15.5	0.511	0.940	0.053	0.747	35.1
CY-4b	Basalt	0.070	0.013	4	0.010	51.9	0.390	6.70	0.132	15.2	0.506	0.905	0.052	0.745	34.1
CY-A	Basalt	0.045	0.010	4	0.008	51.5	0.400	6.80	0.142	16.1	0.538	0.739	0.042	0.827	34.2
CY-D	Basalt	0.087	0.011	4	0.009	53.8	0.490	4.60	0.148	18.3	0.600	0.780	0.046	0.890	37.2
ZY-61	Basalt	0.076	0.019	4	0.015	53.0	0.440	5.90	0.144	20.8	0.714	1.10	0.068	1.02	34.2
CY 15	Basalt	0.063	0.024	4	0.019	57.9	0.538	6.18	0.169	28.7	0.967	0.674	0.051	1.58	41.2
CY 45	Basalt	0.102	0.027	4	0.021	51.8	0.620	5.68	0.164	27.8	0.952	0.713	0.045	1.30	38.3
CY 12	Basalt	0.107	0.018	4	0.014	47.7	0.450	5.79	0.124	23.3	0.827	0.550	0.049	1.04	37.3
CY 31	Basalt	0.033	0.046	4	0.037	58.0	0.270	9.44	0.141	7.48	0.336	1.86	0.169	1.30	38.8
CY 33	Basalt	0.149	0.035	4	0.028	53.9	0.290	8.49	0.145	10.7	0.428	0.935	0.069	0.475	36.4
CY 34	Boninite	0.168	0.032	4	0.025	49.5	0.590	8.47	0.097	25.6	0.900	0.899	0.055	0.530	36.7
CY 36	Boninite	0.146	0.045	4	0.036	55.3	0.310	6.81	0.206	9.04	0.363	1.98	0.152	0.451	42.9
CY 39	Boninite	0.166	0.014	4	0.011	53.3	0.340	7.66	0.210	8.21	0.338	1.83	0.144	0.420	46.1
CY-4b	Boninite	0.077	0.029	4	0.023	51.9	0.390	6.70	0.132	15.2	0.506	0.905	0.052	0.745	34.1
Cy1	Basalt	0.102	0.269	1	0.035	53.9	0.390	7.40	0.132	15.5	0.511	0.940	0.053	0.747	35.1
Cy4	Basalt	0.033	0.370	1	0.048	51.9	0.390	6.70	0.132	15.2	0.506	0.905	0.052	0.745	34.1
Cy61	Basalt	0.061	0.253	1	0.033	52.7	0.660	6.60	0.15	20.4	0.730	1.14	0.070	1.03	33.6
Cy62	Basalt	0.099	0.262	1	0.034	50.5	0.530	7.20	0.094	17.8	0.597	0.463	0.030	1.06	23.4
cy63c	Basalt	0.087	0.268	1	0.035	52.4	0.410	7.50	0.131	16.8	0.525	0.924	0.055	0.756	36.1
<i>Papua New Guinea - Cape Vogel</i>															
PNG 1	Boninite	0.114	0.016	4	0.012	55.4	0.302	14.2	0.734	46.2	1.14	1.97	0.17	0.922	34.4
PNG 8	Boninite	0.133	0.040	4	0.032	55.9	0.121	19.7	0.484	26.2	0.630	1.21	0.106	0.452	30
PNG 10	Boninite	0.143	0.045	4	0.036	56.6	0.141	17.9	0.566	30.4	0.730	1.33	0.123	0.529	31.5
PNG 12	Boninite	0.112	0.031	4	0.024	54.9	0.381	11.3	0.816	54.0	1.34	2.37	0.205	1.12	34.8
PNG 14	Boninite	0.136	0.071	4	0.056	55.2	0.140	22.6	0.384	17.2	0.420	0.816	0.065	0.441	26.5
PNG 25	Boninite	0.109	0.045	4	0.036	55.4	0.355	13.3	0.872	58.2	1.42	2.66	0.211	1.12	30.5

PNG 27	Boninite	0.123	0.030	4	0.024	57.0	0.151	16.2	0.602	33.3	0.799	1.46	0.134	0.58	32.6
PNG 62	Basalt	0.035	0.016	3	0.020	52.5	0.763	6.30	0.186	35.3	1.14	0.696	0.047	1.52	44.1
PNG54	Basalt	0.110	0.275	1	0.036	50.2	0.642	7.60	0.155	37.8	1.18	0.700	0.045	1.58	46.3
PNG59	Basalt	-0.027	0.310	1	0.040	50.2	0.709	8.10	0.108	29.6	0.934	0.534	0.036	1.27	48.8
PNG63	Basalt	0.034	0.231	1	0.030	52.6	0.752	5.70	0.157	28.3	0.814	0.921	0.047	1.59	41.9

Sunda Arc

I2Kr2	basalt. Andesit	0.105	0.028	4	0.022	54.7	1.10	4.05	3.08	113	3.22	3.11	0.193	5.13	26.8
I4Sm1	Basalt	0.045	0.017	4	0.013	50.4	1.40	6.11	5.69	109	3.13	6.65	0.465	4.65	34.5
I12Mu2	Absarokit	0.067	0.017	4	0.013	44.8	1.31	10.5	10.6	190	5.14	36.5	2.07	11.6	38.4
I29Ag2	basalt. Andesit	0.125	0.016	4	0.013	56.4	0.828	3.45	3.33	#NV	#NV	#NV	#NV	4.31	21.7
I32Ri3	Basalt	-0.008	0.010	4	0.008	49.6	1.05	4.57	1.78	53.9	1.76	2.57	0.162	3.54	24.4
I3 Ga1	Basalt	0.023	0.024	4	0.019	48.9	0.831	10.6	0.817	41.4	1.30	1.74	0.106	2.07	43.7
I 25Pe1	basalt. Andesit	0.082	0.025	4	0.020	44.8	0.810	15.1	14.0	124	3.14	31.5	1.35	8.84	34.4
I16Mu6	Absarokit	0.276	0.026	4	0.020	52.5	0.687	2.22	50.4	313	6.42	93.6	3.78	19.1	8.4

Solomon Islands

S 3	Basalt	0.036	0.060	5	0.037	46.7	0.660	11.04	0.183	17.7	0.585	0.214	0.014	1.39	54.9
S 18	Basalt	0.042	0.032	4	0.026	47.5	0.460	10.64	0.325	27.7	0.728	0.640	0.032	1.74	37.9
S E 15	Basalt	0.095	0.029	4	0.023	50.0	0.760	4.33	3.26	84.1	2.03	1.92	0.072	4.93	32.7
S 153 Mbo	Basalt	0.039	0.031	4	0.024	48.4	0.760	7.46	0.493	34.8	1.21	0.695	0.042	2.22	61.7
S 187 Van	Basalt	0.045	0.026	4	0.021	49.0	0.720	4.43	0.424	44.9	1.33	0.792	0.045	2.38	29.7
S 207 Tin	Basalt	0.051	0.036	4	0.028	49.2	1.35	4.52	0.488	78.1	2.01	2.37	0.129	3.27	28.8
S 217 SC	bas. Andesite	0.070	0.012	4	0.009	52.1	0.910	4.43	0.549	74.9	1.90	1.17	0.062	2.68	30.7
S 220 SC	bas. Andesite	0.034	0.031	4	0.024	51.8	1.12	3.60	1.27	88.1	2.40	2.19	0.119	3.80	33.9

New Britain

SHR5	trachytic andesite	0.275	0.014	5	0.009	62.6	0.904	1.93	1.67	132	3.04	2.69	0.162	5.07	13.3
SHR9	andesite	0.215	0.012	5	0.007	59.0	0.833	4.01	1.43	103	2.39	2.08	0.126	4.41	27
SHR13	trachytic andesite	0.241	0.029	5	0.018	61.1	0.904	2.30	1.55	126	2.88	2.46	0.154	4.83	15.1
SHR31	basaltic andesite	0.269	0.012	5	0.007	52.3	0.753	6.17	1.82	131	3.00	2.52	0.149	5.27	19.7
SHR32	dacite, trachytic andesite	0.373	0.010	5	0.006	65.7	0.803	1.24	1.92	151	3.48	2.94	0.181	5.23	8.72
SHR24	basaltic andesite	0.264	0.022	5	0.014	53.1	0.673	5.65	1.71	122	2.83	2.38	0.135	4.98	20.3
SHR26	andesite	0.132	0.028	5	0.017	58.3	0.883	2.91	1.16	186	2.86	1.86	0.108	4.06	25.6

SHR14	basalt	-0.013	0.007	4	0.005	48.6	0.720	5.23	0.255	28.0	0.700	0.570	0.030	2.05	39.6	
SHR16	basalt	-0.022	0.023	4	0.018	50.2	0.994	5.64	0.399	40.1	1.01	0.739	0.042	2.60	44.5	
SHR22	andesite	0.079	0.032	4	0.025	61.7	0.853	2.02	1.65	48.6	1.32	0.979	0.054	3.38	25.3	
<i>Sunda arc sediments</i>																
DSDP 27-261-2-2-11.92m	Mudstone	0.616	0.122	4	0.097	#NV	#NV	#NV	3.7	96.4	#NV	#NV	#NV	#NV	#NV	
DSDP 27-261-3-3-51.33m	Carbonate	0.227	0.021	4	0.017	#NV	#NV	#NV	1.14	54.9	#NV	#NV	#NV	#NV	#NV	
DSDP 27-261-5-1-162.48m	Mn-oxid-rich muds	0.610	0.007	4	0.006	#NV	#NV	#NV	4.54	117	#NV	#NV	#NV	#NV	#NV	
DSDP 27-261-6-1-177.41m	Mudstone	0.547	0.008	4	0.007	#NV	#NV	#NV	4.00	181	#NV	#NV	#NV	#NV	#NV	
DSDP 27-261-9-3-202.95m	Mudstone	0.246	0.067	4	0.054	#NV	#NV	#NV	1.66	137	#NV	#NV	#NV	#NV	#NV	
DSDP 27-261-22-2-344.31m	Sandstone	0.206	0.037	4	0.030	#NV	#NV	#NV	1.97	98.6	#NV	#NV	#NV	#NV	#NV	
DSDP 27-261-28-2-448.42m	Carbonate	0.475	0.029	4	0.023	#NV	#NV	#NV	1.81	53.1	#NV	#NV	#NV	#NV	#NV	
<i>Mediterranean sediments</i>																
DSDP-13-127-2-5-140/141cm	Graded sands; marl oozes	0.185	0.015	4	0.012	45.2	0.9	2.84	7.28	221	5.77	27.5	1.65	6.76	15.1	
DSDP-13-128-6-3-50/52cm	Graded silt/sand	0.193	0.013	4	0.011	46.9	0.91	3.2	7.30	114	3.09	12.6	0.784	7.20	14.3	
DSDP-13-127-18-1-100/102cm	Limestone	0.160	0.024	4	0.019	10.3	0.14	1.27	2.61	130	3.57	8.49	0.522	1.87	3.43	
ODP-160-970-A-9X-1-32/34cm	Clust-rich mud; debris flow	0.008	0.033	4	0.026	31.4	0.46	3.97	7.03	61.4	1.68	7.05	0.443	4.58	10.8	
ODP-160-970-A-16X-2-44/46cm	Clust-rich mud; debris flow	0.224	0.050	4	0.040	33.1	0.3	2.24	5.27	118	3.20	13.6	0.852	3.63	5.87	

Erklärung zum Eigenanteil an den Publikationen

Als Erstautor bin ich für den Inhalt der hier gelisteten Publikationen verantwortlich. Alle Daten, sofern nicht anderweitig gekennzeichnet, wurden von mir persönlich erhoben, ausgewertet und interpretiert.

Erklärung gemäß §4, Abs. 9 der Promotionsordnung der Mathematisch-Naturwissenschaftlichen Fakultät

Ich versichere, dass ich die von mir vorgelegte Dissertation selbständig angefertigt, die benutzten Quellen und Hilfsmittel vollständig angegeben und die Stellen der Arbeit – einschließlich Tabellen, Karten und Abbildungen –, die anderen Werken im Wortlaut oder dem Sinn nach entnommen sind, in jedem Einzelfall als Entlehnung kenntlich gemacht habe; dass diese Dissertation noch keiner anderen Fakultät oder Universität zur Prüfung vorgelegen hat; dass sie – abgesehen von unten angegebenen Teilpublikationen – noch nicht veröffentlicht worden ist, sowie, dass ich eine solche Veröffentlichung vor Abschluss des Promotionsverfahrens nicht vornehmen werde. Die Bestimmungen der Promotionsordnung sind mir bekannt. Die von mir vorgelegte Dissertation ist zu Beginn von Dr. Peter Sprung betreut worden .

Köln, 18.01.2020

Veröffentlichte Teilpublikationen:

Kommescher*, S.; Thiemens, M. M.; Münker, C.; Sprung, P; (2017) Revisiting the Ti isotope inventory of the Moon. *Goldschmidt 2017 Conference abstract*

Kommescher*, S; Fonseca, R. O. C; Kurzweil, F.; Müller L. J. A.; Münker, C.; Thiemens, M. M. T; Sprung, P; (2017) New insights into lunar basalt source from Ti isotope variations. *Goldschmidt 2019 Conference abstract*

Kommescher*, S; Fonseca, R. O. C; Kurzweil, F.; Thiemens, M. M. T; Münker, C.; Sprung, P; (accepted manuscript, final revisions) Unravelling lunar mantle processes through the Ti isotope composition of lunar basalts. *Geochemical Perspective Letters*

Kommescher*, S; Fonseca, R. O. C; Kurzweil, F.; Rzehak, L. J. A.; Münker, C.; Sprung, P; (in preparation) Titanium isotope variation in subduction zone rocks (preliminary title)

CURRICULUM VITAE

PERSÖNLICHE INFORMATIONEN

Name: Sebastian Kommescher, M.Sc.
Geburtstag: 20.02.1987
Geburtsort: Le Chesnay (F)
Staatsangehörigkeit: Deutsch

BILDUNG

Seit 2016 Promotion im Rahmen des UoC Advanced Post Doc Grant innerhalb der Exzellenz Initiative an Dr. Peter Sprung mit Titel: *“Titanium isotope constraints on silicate differentiation and nucleosynthetic heritage of Earth and Moon”*
Titel der Promotion: *„Mass-dependent Ti isotope variations in terrestrial and lunar basalts“*.
2013 - 2015 Master of Science: *“Rubidium / Strontium dating of Rubidium-poor terrestrial and extra-terrestrial samples”*; Betreuer: Prof. Dr Harry Becker, Prof. Dr. Timm John, Endnote: 1.5
2011 - 2015 MSc-Student: Geologische Wissenschaften, Freie Universität Berlin, Endnote: Sehr gut (1.5)
2011 Bachelor of Science: *“Rhenium / Osmium dating and highly siderophile element abundances in a mantle pyroxenite of the Lanzo peridotite massif”*; Betreuer: Prof. Dr Harry Becker, Dr. Konrad Hammerschmidt; Endnote: Gut (2.3)
2008 - 2011 BSc-Student: Geologische Wissenschaften, Freie Universität Berlin, Endnote (2.5)
2006 Abitur Hardtberg Gymnasium Bonn

BERUFLICHE QUALIFIKATION:

2019 Stipendiat der GSGS; Grant Nummer GSGS-2019X-07
2018 - 2019 Student Council Member der Graduate School of Geosciences
2014 Wissenschaftliche Hilfskraft: *Environmental Monitoring of Hexabromocyclodecane in Europe*; Betreuer: cand. Dr. Mathias Ricking
2014 Wissenschaftliche Hilfskraft: *“Early Archaean crust-formation processes constraints from the Ancient Gneiss Complex (Swaziland) and the Itsaq Gneiss Complex (West Greenland)”*; Project supervisor: Dr. Elis Hoffmann
2012 - 2014 Wissenschaftliche Hilfskraft: *“Highly siderophile element abundances in components of Chondrites”*; PhD Projekt, Yogita Kadlag
2010 - 2012 Studentische Hilfskraft: *“Highly siderophile element geochemistry of mantle pyroxenites”*; PhD Projekt, Timo Gawronski
2006 - 2007 Wehrdienst
